The Dissertation Committee for Victor Chijioke Duribe
certifies that this is the approved version of the following dissertation:

Capacitance Resistance Modeling for Improved Characterization in Waterflooding and Thermal Recovery Projects

Committee:

Thomas F. Edgar, Supervisor

Larry W. Lake, Co-Supervisor

Michael Baldea

Leon S. Lasdon

Isaac C. Sanchez

Capacitance Resistance Modeling for Improved Characterization in Waterflooding and Thermal Recovery Projects

by

Victor Chijioke Duribe, B.S.

DISSERTATION

Presented to the Faculty of the Graduate School of

The University of Texas at Austin

in Partial Fulfillment

of the Requirements

for the Degree of

DOCTOR OF PHILOSOPHY

THE UNIVERSITY OF TEXAS AT AUSTIN

December 2016

To my sister, *Nkechi*.

Acknowledgments

I would like to thank my advisors Drs. *Thomas Edgar* and *Larry Lake* for their guidance and mentorship throughout the course of my graduate studies. It has been a life changing opportunity to work with and learn from educators and researchers of their caliber. I am indebted to them for their significant investments of time and effort without which this dissertation would have been impossible. Many thanks also go to the other members of my doctoral committee, especially Dr. *Leon Lasdon*, whose inputs early on were critical in shaping the course of the research presented in this dissertation.

I am also grateful to the McKetta Department of Chemical Engineering, the Petroleum Engineering department, and the sponsors of the Center for Petroleum Assets Risk Management (CPARM) at the University of Texas at Austin for their financial support. I acknowledge *Kristine Poland* and *Heather Felauer* for providing the administrative support that allowed me to focus on research. Special mention is due *Kate Baird* and *Randy Rife* of the McKetta Department of Chemical Engineering. Their willingness to help in taking care of the administrative and IT issues (respectively) that arise ever so often is matched only by the quick and responsive manner with which they address these issues.

Many different software tools were used in this work. The STARS

thermal simulator was provided by Computer Modeling Group (CMG), GAMS software was provided by the provided by GAMS Development Corporation, and the MATLAB software was provided by MathWorks®. Their support is appreciated. I would also like to thank *Lionel Ribeiro* and *Jason Bryant* of Statoil ASA for their role in what was an amazing internship experience two summers ago.

It has been an absolute pleasure working with past and present members of the Lake and Edgar research groups. I am thankful for the opportunity to collaborate with the passionate, hardworking, and bright individuals that make up these groups. Special thanks go to Drs. *Jong Kim*, *Fei Cao*, and *Anh Nguyen*, whose works served as the immediate stepping stones from which my research took off. I am grateful to them for the discussions early on in my graduate studies that were instrumental towards developing my understanding of the capacitance resistance modeling method. I would also like to thank Dr. *Xu (Richard) Shu* of the Edgar group, collaboration with whom made the development of the denoising strategy presented in this dissertation possible.

Finally, I would like to express my gratitude to my friends and relatives, whose support and encouragement shone bright especially through dark and tortuous patches on my way towards this dissertation. Special thanks to *Yusra*, for her patience with me in those moments when the stress of constant research becomes borderline. My deepest gratitude goes to my mother, *Chinyere*; my sisters, *Chisom*, *Onyinyechi*, *Chidoziri*, and *Nkechinyere*; my nieces, *Ugonnaya*, *Chimdi*, and *Nwabunwanneya*; and my brothers-in-law, *Bill* and *Ugochukwu*.

This dissertation would be impossible but for their constant encouragement and unwavering support especially during these ten years that I have been abroad in pursuit of higher education. I remain ever grateful for their love and sacrifice, to which this dissertation is a tribute.

Capacitance Resistance Modeling for Improved Characterization in Waterflooding and Thermal Recovery Projects

Victor Chijioke Duribe, Ph.D.
The University of Texas at Austin, 2016

Supervisors: Thomas F. Edgar
Larry W. Lake

Rates are typically one of the most measured in an oil recovery project. The abundance of these types of data is explained partly by their relative ease of collection. Additionally, their collection and reporting is often required for logistical as well as financial purposes. Numerous researchers have shown the potency of using these data for characterization and management of oil reservoirs under primary or secondary recovery.

Reduced-order models typically use these measurements as input to characterize reservoirs. The capacitance resistance model (CRM) is one such reduced order modeling method. This model uses well rates (and bottomhole pressure data, if available) to characterize a reservoir in a cheap and fast way. In characterizing an oil reservoir, the CRM and its linear counterpart (the Integrated Capacitance Resistance Model or ICRM) use historical data available at the wells to infer connectivity and flow paths between these wells

through a set of model parameters. This use of readily available data, enabled by the speed of these models, creates a powerful tool that can be used as an alternative or as a complement to more expensive and time consuming traditional reservoir management tools.

The CRM was initially developed for secondary recovery (i.e., waterflooding) but has been shown to work very well for primary recovery and many enhanced oil recovery (EOR) processes. The increasing industry acceptance of this modeling method is because of the work researchers who have contributed in expanding the capabilities of this modeling approach. However, key questions such as the impact of noise of CRM and ICRM performance remain. Additionally, a rigorous way of designing injection rates (a key input into the CRM model) such that parameter estimation is optimal has not been addressed. Finally, ideas about the applicability of the CRM modeling method to thermal EOR processes has not been explored.

This research aims to address these questions. By addressing these questions, this work aims to contribute towards deepening current understanding of the CRM modeling method and to opening new avenues for its application and research.

Table of Contents

List of Tables

List of Figures

Chapter 1

Introduction and Research Objectives

1.1 Introduction

Depending on the particular nature of a discovery, a reservoir may undergo primary, secondary, and/or tertiary recovery. During primary recovery, oil is expelled from within the pores of an oil-bearing rock by the excess compressional energy contained in the reservoir. For reservoirs in which the reservoir/fluid flow properties are conducive for the natural outflow of oil (and other reservoir fluids), recovery typically starts with this technique. Artificial lift techniques such as gas lift or pumping may be initiated after economic limit is reached. As shown in Figure 1.1, primary recovery technique may yield from $12 - 15\%$ of original oil in place (OOIP) [34].

Secondary and/or tertiary recovery techniques are necessary when the natural energy of the reservoir is no longer sufficient to support economic production. In secondary recovery, water or other fluids naturally occurring within the reservoir is (re-)injected to increase reservoir pressure and thus produce another $15-20\%$ OOIP. Tertiary recovery is used when pressure support alone is not sufficient. Here, gases, heat agents, chemicals, or biosurfactants are introduced to improve fluid properties that may be limiting flow and improve

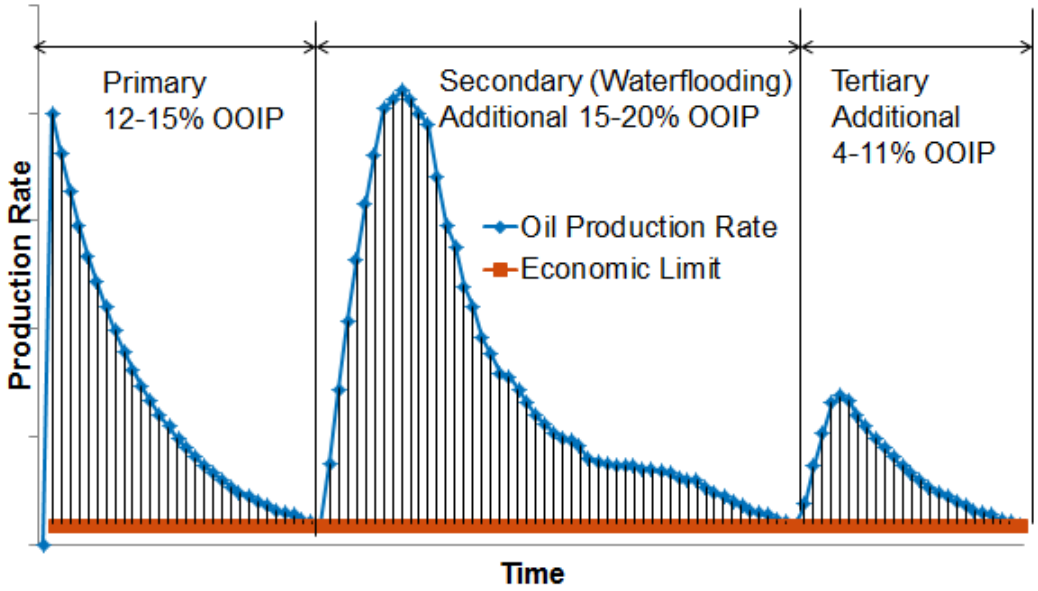

Figure 1.1: Typical recovery profile of a conventional oil recovery

production. Tertiary recovery yields $4 - 11\%$ OOIP [34].

For maximum and profitable exploitation of the resources trapped in a petroleum reservoir through these recovery mechanisms, proper characterization is necessary. This is so because strategic decisions, a water (or steam) injection scheme in a secondary (or thermal) recovery project for example, depend on how well the reservoir under exploitation is known. Consequently, the outcome of these important decisions, and more importantly, their financial ramifications, depends on how accurately the reservoir is characterized.

Reservoirs, however, are intrinsically complex systems. They generally have multiple inputs and outputs interacting in ways complicated by the heterogeneities existent in most reservoirs. Therefore, reservoir characterization

is a difficult task and accurate implementation of it can be time-consuming and financially intensive.

One approach to reservoir management is by numerical simulation. Simulations capture the behavior of oil reservoirs by solving first principle equations of fluid flow in porous media. In this way, Darcy's equation for fluid flow is coupled with principle(s) of conservation of mass and/or energy and solved for each grid block to yield accurate results. However, reservoir simulations are often time-consuming, have enormous data requirement and their results are prone to geological uncertainty [47],[30]. This makes their application for different possible scenarios very difficult.

An approach to complementing simulations as well as alleviating their disadvantages is via input-output reservoir models. Input-output reservoir models involves the merging of reservoir engineering principles with field measurements to provide a framework on which past reservoir behavior can be modeled and future production forecasted. Compared to detailed grid-by-grid numerical simulations, these models are simpler, less data intensive (and hence cheaper to build) and also quicker to implement.

These input-output models have found wide application in the oil industry. One reason for this is because of their simplicity and speed of implementation, which make realization of multiple runs and/or cases possible. This enables the study of different possible scenarios in order to increase characterization accuracy. Also, input-output models are more advantageous, compared to the reservoir simulation approach, in handling the complexities of large

and/or old fields with hundreds of wells and/or long histories [68].

Capacitance resistance models (CRMs), being of the input-output type, possess these desirable characteristics and thus its use for accurate characterization of reservoirs under primary and/or secondary recovery has been widespread over the past decade. However, important questions surrounding the influence of noise on these models, the nature of perturbations necessary for optimal model performance, as well as their use in non-isothermal recovery processes remain. This work focuses on addressing these questions.

1.2 Model Description

1.2.1 The Capacitance Resistance Model (CRM)

The CRM is a reduced order, input-output model that characterizes a reservoir using production and injection rate data (and also bottomhole pressure (BHP) data, if available) only. The CRM is so named due to the analogy of an oil reservoir undergoing waterflooding with a resistance-capacitance (RC) circuit. This analogy was first proposed and demonstrated by Bruce [8] in an experiment in which he combined RC units to physically simulate a reservoir. In this analogy, the production rate from a reservoir resulting from a step change in the injection rate is analogous to the voltage measurement of a capacitor in a parallel RC circuit where the battery potential is analogous to the injection signal [55].

This model is parametrized by a gain, which shows the quantity of the injectant supporting production at a given producer at steady state, and a time

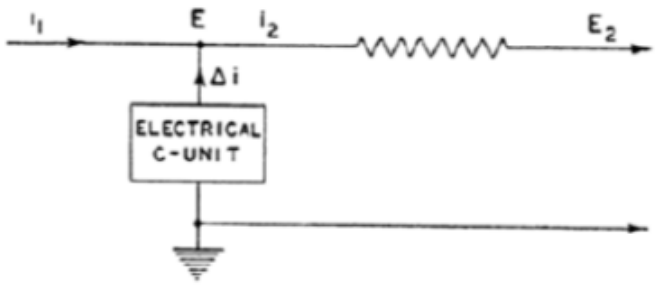

Figure 1.2: An electrical Resistance-Capacitance unit (from [9])

constant, which indicates the response time of a producer to a perturbation at a given injector. In characterizing a reservoir, the CRM uses historical data to determine the connectivity and flow path between well pairs.

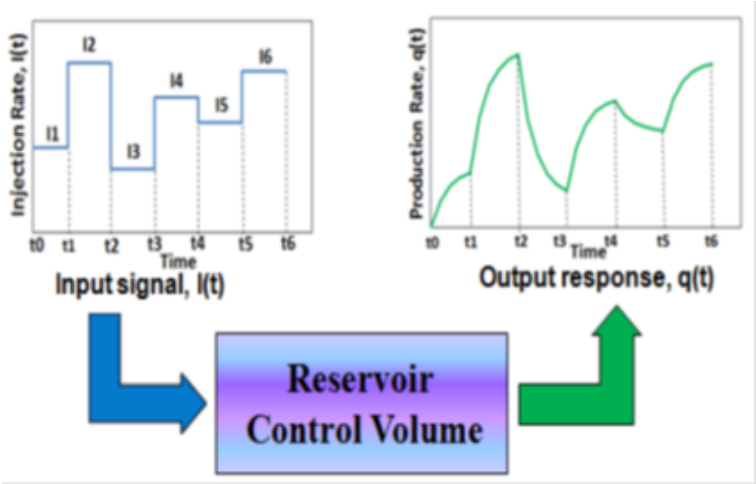

Figure 1.3: Schematic representation of production response caused by fluctuations in the injection rates for an arbitrary reservoir control volume ([30])

By solving the material balance based ordinary differential equation using the principle of superposition in time for three different control volumes, the CRM is present in the following model structure:

- **tank model CRM (CRMT)**, where the control volume is the entire reservoir undergoing waterflooding,
- **producer based CRM (CRMP)**, where the control volume is the drainage volume around a given producer,
- **injector-producer based CRM (CRMIP)**, where the control volume is the drainage area between a given injector-producer well pair.

Detailed derivation of these different variants of the model is presented in [55].

The producer based CRM in its differential form, first derived in [55], is shown in Equation 1.1.

$$V_P c_t \frac{d}{dt}\left[\frac{q_j(t)}{J_j(t)} + P_{wf}(t)\right] = \sum_{i=1}^{N_{inj}} f_{ij} I_i(t) - q_j(t) \tag{1.1}$$

where V_P is producer pore volume, c_t total compressibility, $q(t)$ production rate for producer j at time t, P_{wf} bottomhole pressure, f_{ij} interwell connectivity or gain, I_i injection rate for injector i, J_j producer productivity index, N_{inj} number of injector(s).

Sayarpour [55] solved this ODE using the principle of superposition in time to obtain an analytical form for the CRMP as shown in Equation 1.2.

$$q_j^k = q_j^{k-1} e^{-\Delta t/\tau_j} + \left(1 - e^{-\Delta t/\tau_j}\right) \sum_{i=1}^{N_{inj}} f_{ij} I_i(t) \tag{1.2}$$

where τ_j is producer j's time constant and Δt represents time step between discrete times k and $k+1$

The parameters i.e., the time constant and gains are estimated through a least square fitting procedure using the objective function in Equation 1.3 and under the constraints shown in Equations 1.4 and 1.5.

$$minimize \sum_{k=1}^{n_t} \sum_{j=1}^{n_P} \left(q_j^k - q_j^{k,obs}\right)^2 \tag{1.3}$$

$$subject\ to \sum_{j=1}^{n_P} f_{ij} \leq 1, \forall all\ injectors \tag{1.4}$$

$$f_{ij}, \tau_j > 0 \tag{1.5}$$

1.2.2 The Integrated Capacitance Resistance Model (ICRM)

The ICRM is presented as Equation 1.6 and is obtained by integrating the fundamental differential equation for the CRMP. This model fits historical cumulative production and injection data to obtain parameter estimates by minimizing, in a least square sense, an objective function that is shown in Equation 1.7 under the same constraints as the CRMP.

$$N_{p,j}^k = (q_j^0 - q_j^k)\tau_j + \sum_{i=1}^{N_{inj}} f_{ij} CWI_i^k \tag{1.6}$$

$$minimize \sum_{k=1}^{n_t} \sum_{j=1}^{n_P} \left(N_{P,j}^k - N_{P,j}^{k,obs}\right)^2 \tag{1.7}$$

where $N_{p,j}^k$ is cumulative production rate for producer j at time step k and CWI_i^k is cumulative injection at injector i till timestep k.

From Equations 1.4, 1.5, 1.6, and 1.7, it is seen that the ICRM is a linear model. Because of this linearity, the ICRM offers significant advantages relative to the CRMP. These advantages, relative to the CRMP, are summarized in the Table 1.1.

Model Feature	CRMP	ICRM
Regression method	Nonlinear multivariate	Linear multivariate
Linearity of model	Nonlinear	Linear
Linearity of constraints	Linear	Linear
Dependent variable	Total production rate	Cumulative total production rate,
Independent variables	Water injection rates, producer BHP	Cumulative water injection rates, producer BHP
Estimated parameters	Time constants (τ), gains (f_{ij}), productivity indices (J_j)	Time constants (τ), gains (f_{ij}), productivity indices (J_j)
Convex optimization	No	Yes
Analytical solution	Not possible	Possible with constraints relaxed
Uniqueness of solution	Not unique (possibly local minimum)	Unique (global minimum)
Direct estimation of confidence interval of estimated parameters	Difficult	Easy
Relative computation time	Slow	Fast

Table 1.1: Qualitative comparison between CRMP and ICRM (from [30])

1.3 Bootstrapping for Confidence Interval Estimation

For the CRM, determination of parameter confidence interval is important in order to validate history matching results. However, because the CRM is nonlinear, calculation of confidence interval for model parameters is difficult. Weber ([68]) demonstrated an approach for CRM parameter confi-

dence interval estimation which involved the relaxation of model constraints and a removal of time constant as model parameters. This technique allowed for the use of standard linear regression techniques to estimate the confidence intervals of the linearly occurring gains. Because the time constants were considered constants (and not model parameters), their confidence interval could not be estimated using this approach.

Kim ([30]) calculated gain confidence intervals for the same dataset using CRM and ICRM. A comparison of the results showed a significant difference in the confidence interval values obtained from the models. The ICRM yielded tighter confidence interval estimates relative to the CRM. This result demonstrated the superior validity of gains estimated via ICRM relative to those obtained using the CRM [30]. Part of the increased uncertainty in CRM gain estimates seems to emanate from the limiting requirement of removing time constants as model parameters, forcing the uncertainty in the time constants to be reflected through the gains. This misrepresentation of uncertainty necessitates the development of a robust and accurate mechanism for estimating the confidence intervals of CRM gains and time constants.

Bootstrapping is viable method for confidence interval estimation for nonlinear model parameters. The method was introduced by Efron ([19]) for use in estimation of confidence intervals when the application of standard method such as approximate large scale statistics is not possible. Bootstrapping is a computationally intensive method. It involves an extensive repetition of a given data analysis procedure on replicated datasets in order to obtain

sufficient sample size that allows for an estimation of a parameter's confidence interval. This resampling and replication method eliminates the need to impose restrictive constraints (or assumptions) on the distribution of the parameter estimates. Confidence interval estimation via bootstrapping continues to gain increased usage in diverse fields as computing power and availability has increased in recent times. The reader is referred to [21], [17], [26] and [12] for a detailed overview of the bootstrapping method and it different applications. An excellent introduction and overview for an engineer interested in the application of bootstrapping within the signal processing domain is presented [78].

1.4 Heavy Oil Overview

Viscous crude oils and natural bitumen are defined by their density and viscosity. Viscous crude oils are of two types: heavy oil, which according to the United States Geological Survey (USGS) may be defined as reservoir fluid possessing density below 22°API gravity and a viscosity less than 100 cP, and extra-heavy oil, which encompasses oils possessing densities below 10° and viscosities ranging between 100 – 10,000 cP. Natural bitumens generally have densities less than 5°API and viscosities well above 10,000 cP, typically rendering them immobile within a reservoir. This classification is tabulated in Table 1.2.

Because of their increased asphaltene content, heavy crudes and bitumen are denser and more viscous relative to conventional (light) oil [62]. Con-

Category	Characteristics
Heavy oil	10°API <Gravity <22°API
	10 <Viscosity <100 cP
Extra–Heavy oil	5°API <Gravity <10°API
	100 <Viscosity <10,000 cP
Oil Sands/Bitumen	Gravity <5°API
	Viscosity>10,000 cP

Table 1.2: Viscous oil categories and characteristics (from [42])

sequently, these petroleum resources have traditionally been regarded as less valuable. A major reason for this is the increased exploitation and transportation cost their unfavorable flow properties necessitate. Also, these petroleum resources typically have a higher metal content making their processing more expensive.

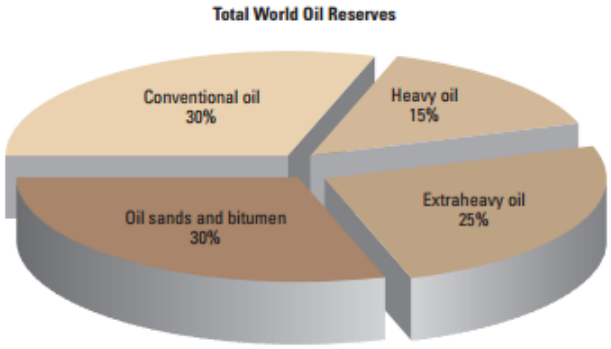

Figure 1.4: Relative distribution of total world oil reserves (from[4])

However, despite the recent downturn in global oil demand, heavy oil remains a viable energy resource around the world. As Figure 1.4, heavy oils and bitumen comprises of over 70% of the current total proven reserves, with

40% representing heavy/extra-heavy oils alone. These percentages translate to an estimated reserves of 3,396 billion barrels of heavy oils (concentrated predominantly in Venezuela in the Orinoco heavy-oil belt) [60] and even at 10% recovery factor, could mean additional decades of supply at current global consumption rates. Additionally, the prolonged, traditional focus on light oil exploitation and consumption, coupled with a deceleration in the discovery rate of new reserves, positions heavy oil as a viable energy resource for the future [42],[41]. Thus, improving heavy oil reservoir characterization time and accuracy, as a way of reducing their exploitation cost, is of significant importance.

1.5 Mathematical Modeling of Thermal Oil Recovery Processes

Thermal oil recovery can be defined as the recovery mechanism in which oil is produced from a reservoir by the supplemental addition of the necessary expulsive energy in the form of heat [24]. This recovery mechanism includes methods like steam assisted gravity drainage (SAGD), steamflooding, hot waterflooding, cyclic steam injection (steam soak or huff and puff) and in-situ combustion. Generally, recovery, via these methods, is facilitated by the in-situ reduction in oil viscosity due to the addition of heat. However, viscosity reduction (and thus oil recovery) may be enhanced in these methods due to other physical and chemical changes that become possible as heat energy is added [13],[18],[70],[36].

Reservoir characterization and management is essential during thermal recovery process in order to maintain profitable operations. This can be achieved, like in other recovery processes, using reservoir simulators that combine geological data and fluid properties with first principle equations to infer energy and fluid flow within the reservoir. Due to the enormous volume of input data required to initialize these simulators and the uncertainty associated with the geological data they require, simulations can be financially and computationally cost intensive.

Different analytical approaches to reservoir modeling have been developed and implemented to complement simulators and ameliorate their high computational intensity. Fundamentally, thermal processes are very complex and hence difficult to accurately model [2]. This is because the interfacial and hydrodynamic phenomena generally present in displacement processes are further complicated by viscous and chemical changes introduced due to reservoir heating [2]. Different modeling attempts are present in literature with varying scopes ranging from Gottfrieds work in modeling thermal recovery in general [24] to Spillette's model for hot waterflooding ([63]), Neuman's for steam drive ([46]), and Youngrens for in-situ combustion [71]. These models, however, rely on geological data in order to capture the complexities of thermal recovery processes. Also, the different assumptions necessary to derive tractable analytical models can lead to loss in generality, inflexibility and oftentimes, inaccurate results.

Reduced-order (input-output) models focus on the main phenomena

of fluid flow while neglecting extraneous processes to obtain descriptive characterization of a reservoir to significant accuracy. These models do not require geological data and thus are able to characterize reservoirs speedily and cheaply. While reduced-order models can be limited by the uncertainties in the production and BHP data that they require, their simplicity and speed make multiple runs that would improve accuracy possible. These favorable factors make reduced order models, such as those of the CRM family, attractive as complements or even replacements to numerical simulators in modeling thermal stimulation processes.

1.6 Research Objectives

The capacitance resistance models (CRMs) provide a reduced-order, input-output modeling approach that characterizes reservoirs using production/injection and BHP fluctuations. The models were primarily developed for waterflooding (secondary recovery) operations and has since been successfully applied to primary recovery and other enhanced oil recovery (EOR) processes. This research focused on improving CRM capabilities for characterization in waterflooded reservoirs as well as extending the CRM technology to thermal stimulation projects.

The four key objectives of this research are as follows:

- **Investigation of noise impact on CRM/ICRM performance:** Because of the data-centric nature of the CRM technology, the importance

of data cleanliness cannot be overemphasized. This research investigates the impact of noise on the performance of the CRM and its linear counterpart, ICRM. Knowledge of noise tolerance levels for both models would help guide appropriate model selection depending on the measured/perceived level of noise in available data.

- **Denoising of production data for CRM parameter estimation:** The need to denoise production data becomes is apparent particularly because of the pervasive noiseness of production data. In this work, noise removal strategies are implemented and analyzed. Comparative analysis of these denoising strategies, complemented with individual sensitivity analysis, will help demonstrate the preferential suitability of each strategy under different noise conditions. The results will provide useful additions to the engineer/practitioners toolkit for battling noise in data.

- **Design of injection rates for optimal parameter estimation:** Because the CRM is an input-output model, characterization with this technology is only as good as the data used. This research effort will focus on designing injection rate profiles, using design of experiments (DOE) concepts, to optimally perturb a reservoir in a way that yields the most accurate parameter estimates.

- **Extension of the CRM technology to thermal recovery projects:** The CRM is particularly attractive for characterization of thermal projects because of its relative speed, no reliance on geological data, and appli-

cability to reservoirs with significant number of wells. This dissertation will focus on developing a CRM variant applicable to thermal processes. Such a model will provide fast and easy alternatives or complements for modeling and managing reservoirs undergoing thermal stimulation.

1.7 Layout of the Dissertation

The remainder of this dissertation is presented as follows:

- **Chapter 2** presents a literature survey of thermal stimulation models, with particular focus on hot waterflood modeling. This intent is not to provide an exhaustive catalog of the developments in these two areas but to give the reader sufficient exposure to the pertinent works which this research will build upon.

- **Chapter 3** provides a detailed assessment of the impact of noise on CRM and ICRM parameter estimation. A comparison of both models provides basis for the development of noise removal strategies as well as for recommendation on model selection.

- **Chapter 4** presents research on denoising of production data using several noise removal strategies. These denoising techniques are compared and sensitivity analyses conducted for each.

- **Chapter 5** presents a method for the optimal design of injection rates. Formulation of the model and its validation using for a synthetic field is included in this chapter.

- In **Chapter 6**, thermal CRM variants for hot waterflooding are developed. An analytical treatment of hot waterflooding is first considered. Then derivation of the thermally coupled CRM (TCCRM) and the LC-CRM for hot waterflood modeling is presented. The chapter concluded with a presentation of model validation results.

- **Chapter 7** presents the conclusions, summarizes key technical contributions, and proposes recommendations for future research.

Chapter 2

Literature Review

2.1 Development of the CRM

Data on injection and production rates are usually abundant during a waterflooding project. The abundance of these types of data is explained partly by their relative ease of collection. Additionally, their collection and reporting is often required for logistical as well as financial purposes.

Numerous researchers have shown the potency of using these data for characterization and management of oil reservoirs under primary or secondary recovery. Albertoni and Lake [3] presented the seminal idea of using production and injection rates only to infer connectivity between wells. Their technique involved the use of multivariate linear regression (MVLR) to quantify interwell communication. A diffusivity filter was used to account for pressure dissipation and time lag between wells. Building upon Albertoni and Lake's work, Yousef [72] presented a capacitance resistance model (CRM) that quantified interwell communication without the use of diffusivity filters. The model was tested using synthetic data and validated, with good agreement, using field data. Sayarpour et al. [56] solved the CRM governing differential equations for different control volumes. Using the principle of superposition in time, semi-

analytical solutions were obtained and validated using simulated and field cases.

In recent years, improvements in the CRM method have positioned the model as a reservoir management tool capable of assisting in performing key tasks such as history matching of production data [57], forecasting of production rates [9], scheduling of injection rates [1], detection of injection leakage [45], estimation of fracture distribution [15], optimization of carbon sequestration [65]. Other improvements have also been achieved through the works of many researchers, some of which are reviewed by Cao in [9]. Table 2.1 summarizes the contributions of different researchers affiliated to the University of Texas at Austin towards the development of the CRM.

Author(s)	Year	Contribution(s)
Yousef A.A	2006	Developed the full CRM in which diffusivity filters were replaced by time constants. Formulated the model in discrete time to ease application to field data. Validated model using synthetic data to obtain results in good agreement with field properties.
Liang et al.	2007	Used CRM to allocate injection rates in a synthetic field with four producers and five injectors. Optimization procedure returned different injection patterns depending on oil and injected water prices used.
Sayarpour M.	2008	Solved the original CRM equation, using superposition in time techniques, for three control volumes to obtain the tank version (CRMT), the producer-based version (CRMP) and the producer-injector pair version (CRMIP). Applied actual field data using stepwise variation of injection rates (SVIR) and linear variation of injection rates (LVIR).

Table 2.1: Summary of CRM contributions at UT

Weber D.B	2009	Introduced a warm start fitting procedure to obtain feasible initial guesses. Introduced a two-stage fitting algorithm to maintain consistency of obtained parameters. Used CRM to optimize injection allocation for large scale waterflooding projects.
Kim J.	2011	Extended the family of Capacitance Resistance Models to include the Integrated Capacitance Resistance Model (ICRM) and the linearly transformed producer based CRM (ltCRMP). Attempted to establish the relationship between interwell connectivity and interwell distance between injector-producer pairs.
Cao F.	2011	Used CRM as a tool to detect and reconcile errors in production data. Data cleaning procedure involved calculating production rates, using the CRM, based on water injection rates applied to a field and subsequently adjusting the errant data points using the calculated rates.
Wang W.	2011	Incorporated geomechanical surface subsidence models with the CRM to predict surface subsidence from injection and production data in the Lost Hills oil fields. Showed that interwell connectivity can evolve temporally, especially in soft reservoir formations, caused by the rearrangement of rock grains that results from rock damage and compaction.
Nguyen A.P	2012	Demonstrated the application of the original CRM by applying to data from a west Texas field. Developed ICRM for primary recovery scenario. Extended the applicability of the CRM method to simultaneous water alternating gas (SWAG) injection projects.
Laochamroonvorapongse R.	2013	Combined analytical tools (RPI- and WOR-plots) with CRM to improve inference of heterogeneity in oil reservoirs. Developed a CRM variant able to improve history matching by taking into account the interaction between producers that result from operational conditions and constraints.

Table 2.1 continued: Summary of CRM contributions at UT

Cao F.	2014	Developed a CRM variant that is applicable to immature waterfloods. This CRM variant, called the Coupled CRM, involved the introduction of a variable time constant, the value of which is update at each time step using results of the saturation equation. Two coupling mechanisms of the saturation and pressure equations were demonstrated.

Table 2.1 continued: Summary of CRM contributions at UT

Despite its success in modeling waterflooding and other oil recovery techniques, CRM has been limited to isothermal processes. Thus, this effort, to our knowledge, is the first to attempt an extension of the CRM to non-isothermal stimulation processes. A thermal CRM provides engineers a powerful tool for quick and accurate history matching of past production data, as well as forecasting and optimization of future production.

2.2 Review of Hot Waterflood Models

For a reservoir containing heavy oil to be produced profitably, it is often necessary to thermally stimulate it. This essentially means injecting heat into the reservoir to heat up the resident oil and improve its flow properties. Heat is introduced into the reservoir through a fluid (typically hot water or steam), by in-situ combustion of oil within the reservoir, or through electrical (resistive) heating.

Hot waterflooding remains a feasible and economically viable way of introducing heat into the reservoir. In fact, from an operational standpoint, hot waterflooding is the most attractive thermal stimulation technique for viscous oils [25]. The simplicity of the process, inexpensiveness of the necessary equipment for generating and handling of hot water, as well as its close similarity to the well-understood cold waterflooding has all contributed in permeating the use of hot water as a flooding agent for viscous oils has persisted.

While the use of hot water for oil recovery is believed to has started in the 1930s [53], the analytical model of this process flourished mainly in the 1950s and beyond. Table 2.2 summarizes the early contributions for thermal recovery modeling in general and hot waterflooding in particular.

Author(s)	Year	Contribution(s)
Lauwerier H.A	1955	First introduced a mathematical model that allowed for the calculation of the temperature profile in a linear, one-dimensional, homogeneous reservoir under hot waterflooding. Model was developed under simplifying assumptions of constant injection rate and temperature, absence of lateral conductive heat transfer, infinite vertical thermal conductivity, and instantaneous establishment of thermal equilibrium between rock and fluids. Heat loss to adjacent strata was not considered.
van Heiningen J; Schwartz N	1955	Used Lauweriers (1955) temperature model to examine the influence of reservoir heating on production characteristics (mainly oil viscosity). Demonstrated a practical application of the temperature model by using it to calculate the increase in recovery factor caused by hot fluid injection in a hot waterflooding project.

Table 2.2: Summary of early hot waterflood modeling contributions

Pratts M.	1959	Proposed a model for calculating the heat efficiency for any thermal recovery process. Assumed, as in Lauwerier (1955), constant thickness of the flooded layer and infinite vertical conductivity but relaxed all other assumptions. Concluded that cold water injection following a hot fluid drive will result in beneficial heat redistribution and may thus improve oil production.
Marx W. J; Langenheim R. H	1959	Introduced a generalized method for analyzing thermal recovery in an idealized radial reservoir with conductive heat loss. Their method calculates thermal invasion rates, cumulative area heated, and theoretical economic limits for hot fluid injection. Presents a table useful for quick and easy estimation of the error function argument occurring in the calculations.
Spillette A. G	1965	Presented a detailed review of the analytical solutions of hot fluid injection problem. Included significant contributions from notable Soviet researchers Rubinshtein L.I, Avdonin N.A, and Malofeev G.E, access to whose works were not generally available beyond the Soviet scientific community. Spillettes review detailed the efforts of these and other researchers to remove the restrictive but simplifying assumptions of infinite vertical thermal conductivity within the reservoir and zero horizontal thermal conductivity made by Lauwerier (1955) in developing his model.
Gottfried B.S	1965	Developed a generalized mathematical model for describing all principal phenomena (i.e., hydrodynamic, temperature, and chemical) possible in the thermal stimulation of linear reservoirs. Model incorporated convective heat loss without addressing conductive heat loss in the adjacent strata. Validated model by comparing to laboratory experiments of a forward in-situ combustion project.

Table 2.2 continued: Summary of early hot waterflood modeling contributions

Thomas G.W	1967	Introduced three approximations for the analytical calculation of the temperature distribution during hot fluid injection. Presented a means of tracking heat propagation in a heated reservoir by introducing an equation for constructing isotherms and for calculating the heated volume. Demonstrated the applicability of the approximate methods using example problems.

Table 2.2 continued: Summary of early hot waterflood modeling contributions

Lauwerier ([35]) first introduced and solved an energy balance model that assumed incompressible flow in a one-dimensional reservoir with no heat loss and constant injection temperature. Spillette ([64]) used this model to calculate spatial and temporal temperature profiles for a 1D reservoir under hot waterflooding. He also presented the latest (at the time) analytical methods for solving the energy balance equation and demonstrated their superior applicability, relative to Lauweriers analytical solution, which is limited by restrictive but simplifying assumptions of infinite vertical thermal conductivity and zero horizontal thermal conductivity.

Marx and Langenheim ([39]) proposed a mathematical model for the temperature dynamics in reservoir radial flow system. One major contribution was the provision of a table for quick and easy estimation of the error function argument that was necessary for the calculations. The model, which was

obtained by solving a heat balance using Laplace transforms, was tested on a steamflooding example that illustrated its use for forecasting oil production.

Because Marx-Langenheims approach was developed for a highly idealized reservoir, certain limiting assumptions made it applicable only to certain aspects of thermal stimulation. Gottfried ([24]) attempted to improve on that by introducing a more generalized thermal stimulation model. His approach incorporated the modeling of all principal phenomena present in a thermal recovery process. A trade-off to this generality, however, was a significant increase in computation time. Building mainly upon Lauweriers and Marx-Langenheims contributions, numerous improvements have been achieved in the analytical modeling of hot waterflooding. These contributions, as well a more detailed overview of the early history of hot waterflooding, are provided in [64], [22], and [53].

A more recent development in modeling hot waterflooding has been the thermal streamline method. This method was introduced by Pasarai and Arihara ([50]) to leverage the speed and accuracy of the original streamline method developed for waterflooding. In this method, the flow equations are solved first assuming incompressibility of rock and fluids to obtain the pressure required for defining the streamlines. Subsequently, the energy balance is solved along each streamline to obtain temperatures at each given pressure and saturation. This decoupling of the fluid flow and energy balance equations results in faster computational time. The model was validated for a one dimensional (1D) and two dimensional (2D) reservoirs, and improvements on

the model have been offered by many researchers.

The improvements over the years, both in terms of computing power and of thermal flooding modeling techniques, have yielded progressively faster models. However, most existing models today still require geological data. This continues to make characterization time consuming for the engineer, especially in situations where speed, not precision, is more important. The CRM, which is fast, cheap and does not need geological data, is therefore well suited to provide such needed characterization alternative.

Chapter 3

Assessment of the Impact of Noise on CRM/ICRM Performance

3.1 Introduction

The Capacitance Resistance Model (CRM) offers the promise of fast and cheap characterization of an oil reservoir. In characterizing an oil reservoir, this reduced-order model uses historical data available at the wells to infer connectivity and flow paths between these wells through a set of model parameters. The use of readily available data, enabled by the speed of the model, creates a powerful tool that can be used as an alternative or complement to the more expensive and typically time consuming traditional reservoir management tools.

However, the CRM is nonlinear in terms of the parameters, making parameter estimation using the model susceptible to suboptimal initialization issues, the possibility of getting stuck at local optima, and the likelihood of generating non-unique solutions when characterizing reservoirs with large numbers of wells [68]. Additionally, the constrained nature of this non-linear model makes it difficult to estimate parameter confidence intervals using standard descriptive statistical techniques.

To address these issues, Nguyen et al. [48] developed an integrated form of the CRM called the Integrated Capacitance Resistance Model (ICRM). The ICRM, being linear in terms of the parameters, ensures that a global optimum is achieved during the parameter estimation problem regardless of the initialization values of the parameter estimates used. The global nature of the optimum and the attendant uniqueness of the parameter estimates a from the convexity of the optimization problem as formulated using the ICRM. Also, calculating the confidence intervals using this model is straightforward since the simpler T-statistics can be used once the constraints are relaxed. This simpler formulation makes ICRM faster relative to the CRM.

In validating the ICRM, Kim et al. [29] presented a high-level, qualitative comparison of the CRM and ICRM. He also compared the results obtained when each of the models is applied to the same dataset and concluded that when clean, high fidelity data are used (as was the case for the numerically simulated datasets they used), good parameter estimates can be expected. However, the question of how noisy data affect estimation using these models, both individually and relative to each other, has largely been unanswered. This question is of immense importance because datasets from oil fields are usually corrupted by measurement noise arising from faulty and/or inappropriately calibrated measuring equipment. Additionally, rate allocation and other similar imprecise measurement practices make field data far from perfect.

This study investigates the impact of noise in production/injection data on parameter estimates obtained using CRM and ICRM. To this end, multiple

datasets with different levels of noise are fitted to each of the models, parameters estimates are obtained and compared to determine which of the two models produces more consistent, accurate results and under which conditions of data noisiness. We note here that previous researchers have recognized the issue of data corruption in field data and its impact on parameter estimation ([68], [10]). These researchers presented efforts to improve parameter estimation in the presence of corrupted data. Weber [68] introduced a two-stage fitting algorithm to improve the consistency of parameters when fitting CRM to field data. The first stage involved a preliminary data cleaning exercise aimed at increasing the quality of data to be fed into the second stage of the fitting algorithm. Cao [10] also used CRM as a tool to detect and reconcile errors in production data. However, both of these efforts at data cleaning were restricted to outlier identification and removal for the CRM alone. The issue of noise impact on any of the models was not addressed and this work intends to fill that gap.

This chapter is organized as follows: First, an overview of the methodology is presented to give the reader the necessary background information. Methods of expressing data quality, obtaining noisy data, and estimating confidence intervals for model parameters are each introduced and described. This is followed by a presentation and discussion of the results of the investigation. Finally, the chapter concludes with a brief summary of key findings.

3.2 Method

3.2.1 Signal-to-Noise Ratio: An Overview

In order to express quantitatively the influence of data quality on the performance of these models, a measure of the noise level present in the data set is necessary. Different techniques for expressing this measure exist in the literature. The common idea behind these techniques is that they compare a certain descriptive measure (such as the spread or the amplitude) of the signal to that of the noise to arrive at a value that indicates the level of noise in the data set.

This work uses the signal-to-noise ratio (SNR) as the quantitative index of data quality. By definition, this index is given by the ratio of the power of the desired signal in the dataset to that of the noise. The SNR comparatively measures the level of a desired signal in the data to the level of background noise accompanying it and ranges between 1 (for a dataset constituting entirely of noise) and infinity (for a dataset with no noise).

$$SNR = \frac{P_s}{P_n} \tag{3.1}$$

where P_s and P_n are the average power of signal and average power of noise, respectively.

The average power of a signal (noise or desired), *x(t)*, is calculated as follows:

$$P_s = \frac{1}{t - t_0} \cdot \int_{t_0}^{t} |x(t)|^2 dt \tag{3.2}$$

Equation 3.2 is only applicable for a continuous time signal, *x(t)*, where integration is possible. The discrete version, which is more fitting for this work since we deal with discrete signals, is as follows:

$$P_s = \frac{1}{k - k_0 + 1} \cdot \sum_{n=k_o}^{k} |x[n]|^2 \tag{3.3}$$

When the noise signal is assumed to be zero-mean, white, and Gaussian, the average power of such a noise sequence is given by the square of the standard deviation, σ^2. Because the additive noise applied to the original (uncorrupted) production signals in this work is generated under the above assumption, we calculate the standard deviation of the noise sequence required to achieve each pre-determined noise (SNR) level as the ratio of the power of the desired signal (given by Equation 3.3) and the SNR. This procedure was followed consistently throughout this work.

3.2.2 Production Data Simulation

To assess the performance of the ICRM and CRM relative to noise, production data to be fitted to the models is first simulated. This involved setting up a two producer, one injector reservoir system with predetermined gains (i.e., connectivities) and time constants. The injection signal was identical to that of Injector 1 in the Streak Case dataset used by Albertoni and

Lake [3] and by Kim [30].

Using this injection data and the preset parameters, the production rates were calculated using the CRM and the ICRM (recursively via Equations 3.4 and 3.5). This constituted the base case.

$$q_j(k) = \frac{1}{(\tau_j + \Delta t)} \cdot \left[\sum_{i=1}^{N_{inj}} f_{ij} CWI_i^k + \tau_j q_o - N_{pj}^{k-1} \right] \tag{3.4}$$

$$N_{Pj}^k = N_{Pj}^{k-1} + q_j^k \cdot \Delta t \tag{3.5}$$

Subsequently, zero-mean, Gaussian, white noise was added to the production rate data and the noise variance gradually increased to yield signals with SNRs spanning five orders of magnitude – from 100000 to 10. Figure 3.1 shows the production rate profiles of both producers before and after noise addition for SNR = 10. Analogous plots for SNRs 100000, 10000, 1000, and 100 are included in Appendix A.

3.2.3 CRM Confidence Interval Estimation

Each of these noisy datasets was fitted with both CRM and ICRM to obtain a new set of parameter estimates and the associated 95% confidence interval for each of the estimates. For the linear ICRM, confidence interval was estimated using standard t-statistical technique. Due to the nonlinear nature of the CRM, the confidence interval for its parameters cannot be estimated using this method. Thus, too obtain these confidence interval estimates, a boot-

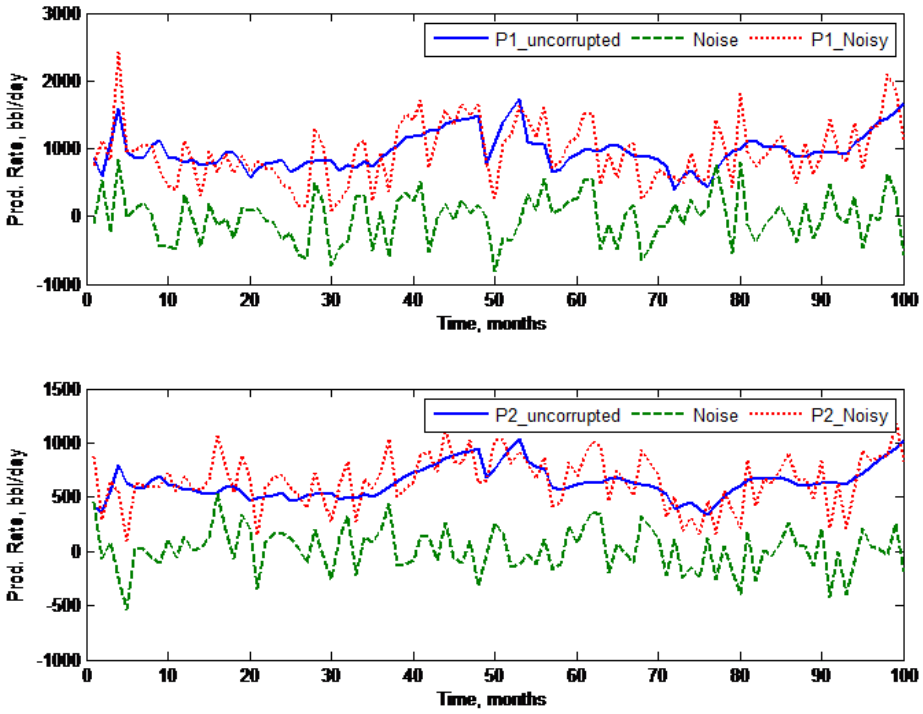

Figure 3.1: Production rate profiles of both producers before and after noise addition for SNR = 10

strapping algorithm introduced by Efron and Tibshirani [20], implemented in MATLAB, was used. In this algorithm, random noise datasets were generated and simultaneously re-sampled 1000 times. These re-sampled datasets were used to generate new production rate values which were then fitted to the CRM model to obtain new parameter sets. For each given parameter, the 2.5^{th} and 97.5^{th} percentile values of these 1000 sets of parameters form the lower and upper confidence limits, respectively. The number of optimal resampling was taken to be 1000 since that number of resampling was required to stabilize the SNR at each noise level (see Figure 3.2).

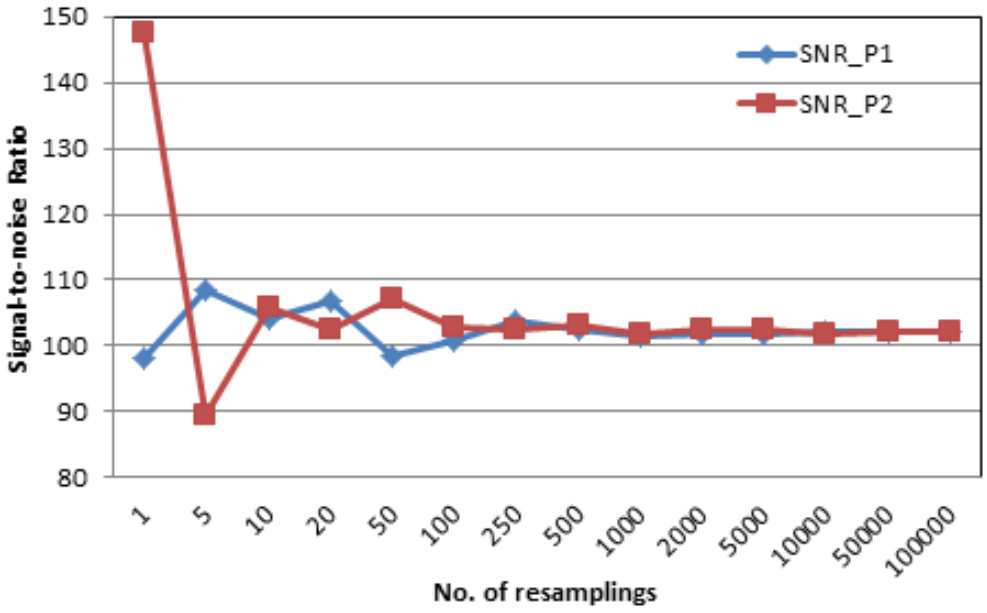

Figure 3.2: Signal SNR as a function of number of resamples for target SNR = 100

For the linear ICRM, the constraints were relaxed and the confidence limits were calculated via usual t-statistics. The 95% confidence interval is calculated as:

$$t_{0.95}(\nu = N - m) \cdot Sy_{/x} \cdot \sqrt{C_{ii}^{-1}} \tag{3.6}$$

where $t_0.95(n)$ is the Student's t-distribution at 95% confidence level; Sy/x is the standard error, C^{-1} is the inverse of covariance matrix. This calculation is presented in more detail in [30].

Note that noise was added only to the production/injection rates after simulation. Hence, simulation or forward propagation was implemented once (for the base case scenario only) because simulated cases are not noisy and thus have SNR values approaching infinity. Altering the SNR of a dataset cannot be achieved by adding noise to the injection data and re-simulating since in such a situation, the intended noise component becomes part of the desired signal.

3.3 Results and Analysis

3.3.1 Effects of noise in the production data only

As mentioned in the preceding section, noise was added to the production rates only after simulation. That is, the injection rate dataset applied to the models was not corrupted and was identical to that used in generating the base case. This approach, from our point of view, closely corresponds to

a scenario in the field where noise and uncertainty are introduced during the measurement of production rates. The introduction of noise during the measurement process may be a result of faulty or improperly calibrated equipment causing production observations to be systematically corrupted. In addition, measurement practices in which the production rate for a producer at each time step is allocated rather that measured directly can give rise to data that is imprecise and noisy.

Noise signals with different standard deviation values were added to production rate signals simulated using the CRM and ICRM, to yield noisy signals with SNR levels ranging from 10 to 100000. Each of these corrupted CRM- and ICRM-generated production rate signals was fitted to the CRM and ICRM respectively obtain model parameters (i.e., gains and time constants) as well as their 95% confidence intervals. Uncorrupted injection rate signal was used for each fitting. The parameter estimates and their 95% confidence intervals are presented as a bar chart in Figure 3.3 to aid visualization.

The plots show the influence of noise on parameter estimation using CRM and ICRM on two levels. First, we observe that the parameter estimates show a deviation from Base Case values with increasing severity as noise level increase. This tendency is more apparent when SNR levels are below 1000. Second, the width of the confidence intervals generally increases with increase in the level of noise in the production data. This observation is intuitive as more noise in the data should lead to increased uncertainty which the width of the confidence interval is a measure of.

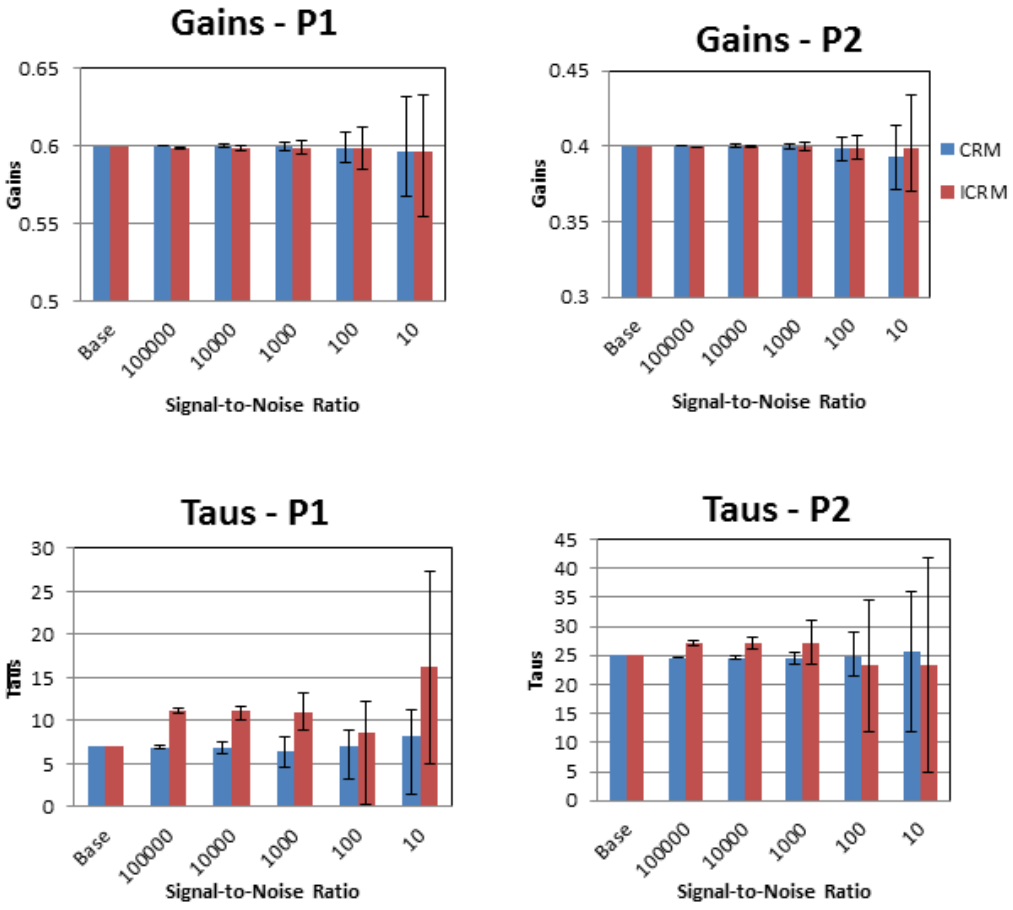

Figure 3.3: Parameters estimated for different noise levels in production data

Because the influence of noise for SNR levels above 1000 is minimal, both models consistently produced estimates that were close to base case values and confidence intervals that were fairly tight. The consistency in the parameter estimates indicates that both models respond with similar sensitivity to noise for SNR levels above three orders of magnitude. For datasets with SNRs below two orders of magnitude, the results indicate that the ICRM shows a greater sensitivity to noise relative to the CRM, as the width of the confidence interval for the ICRM is seen to increase at a faster rate.

The results indicate a threshold of the level of noise above and below which the models show different sensitivities to noise. Since the data used for both models were essentially the same, it seems that the difference in the sensitivities of the models arises mainly from differences in model structure. Because ICRM is structured to use cumulative data, prior integration of production/injection rate data is necessary. Integrating past rates (to yield the current cumulatives) encourages noise accumulation over time and hence error tracking as history matching progresses. This accumulation of noise does not seem to cause a significant deviation of the model estimates from base case values at low noise levels (i.e., high SNR values) but starts to introduce deviations in estimates and a widening of their confidence intervals when noise is sufficiently present. The CRM fitting, on the other hand, is affected only by the noise present at each time step. Consequently, noise is not accumulated during the history matching process, enabling the model to perform better relative to the ICRM, even when the level of noise in the data is significant.

To demonstrate this effect of noise, we compute the power spectrum via fast Fourier Ttansform (FFT) decomposition of noisy production signals calculated using both models. Results of the FFT decomposition is shown for SNR = 10 in Figure 3.4. Analogous plots for SNRs 10000–100 are included in Appendix A. Signal power at zero frequency is omitted in these plots since the added noise being of zero mean does not cause deviation in the signal average. Signal power at frequency 0.0329 (1/day), corresponding to frequency of monthly perturbation, is plotted for all SNRs in Figure 3.5.

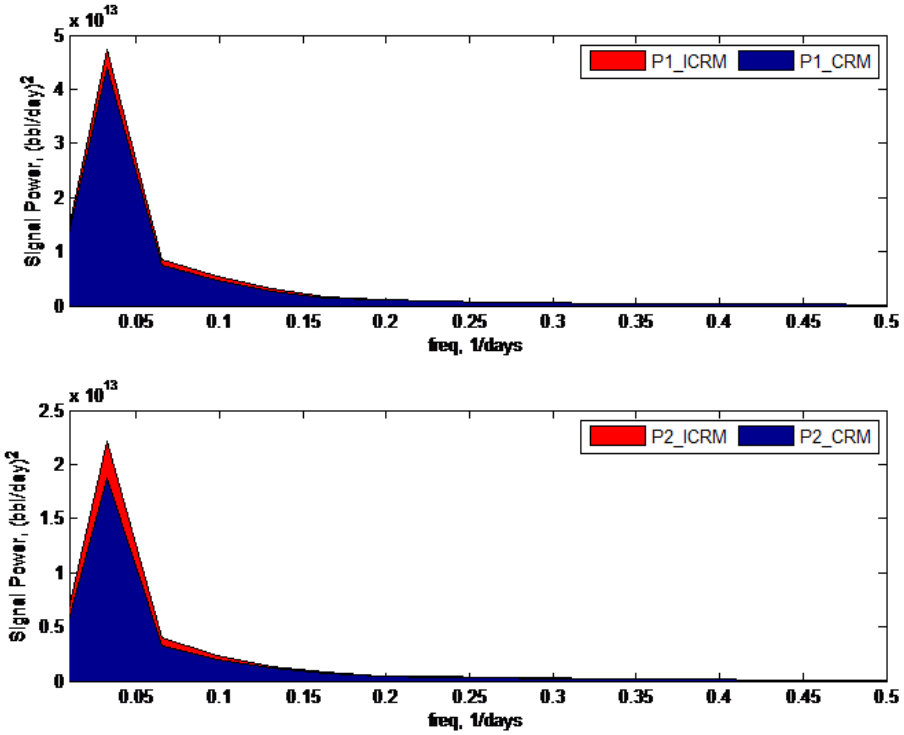

Figure 3.4: Power spectrum for production signals at SNR = 10

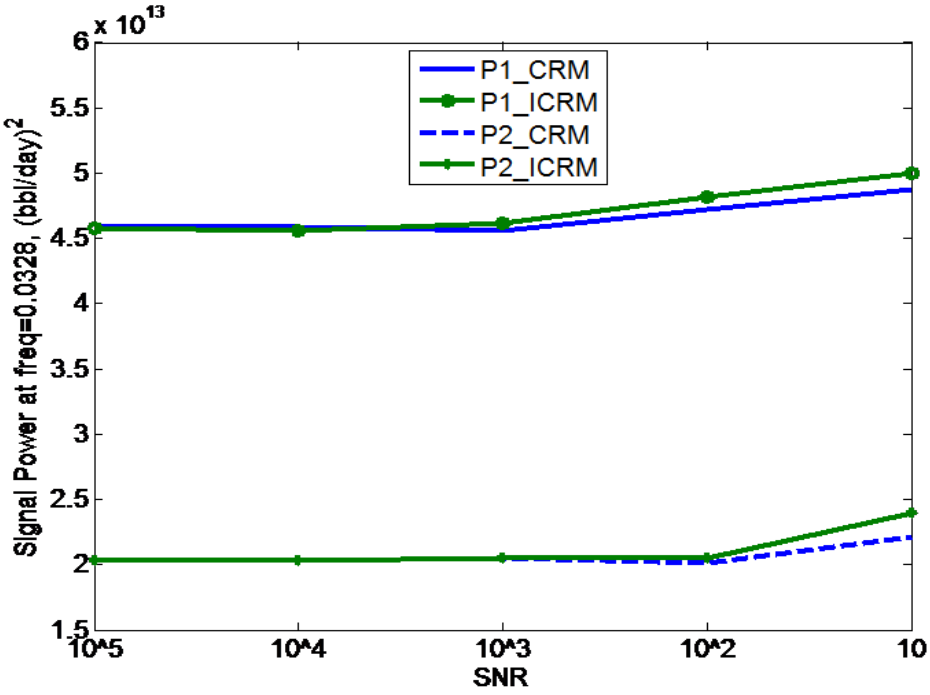

Figure 3.5: Influence of noise on signal power at dominant frequency

Figure 3.5shows that at high noise levels, signal power for the ICRM-generated signal is higher relative to that of CRM-generated signal at lower frequencies. This observation is less apparent as SNR increases, almost disappearing when SNR is above 1000. Because the ICRM is also a low pass filter (like the CRM), this introduction of power into the lower frequency interval causes increased deviation in parameter estimates as well as the confidence intervals. This is exhibited as increased model sensitivity to noise at sufficiently low SNR levels since the increased power at low frequencies originates via additive noise.

3.3.2 Effects of noise in the injection data only

To evaluate the impact of noise in the injection data on parameter estimation, noise signals with different standard deviation values were generated and added to the injection rate signal to yield noisy injection signals with SNR levels ranging from 10 to 100000. Each of these corrupted injection signals was fitted to uncorrupted production rate data to obtain model parameters (i.e., gains and time constants) as well as their 95% confidence intervals.

The parameter estimates obtained for the different SNR values are presented in Figure 3.6. The charts show that the estimates for the gains and time constants do not vary significantly even as SNR decreases. It can also be seen that the confidence interval for each parameter does not increase greatly except for SNR levels approaching 10.

These results indicate that noise in the injection data generally does not

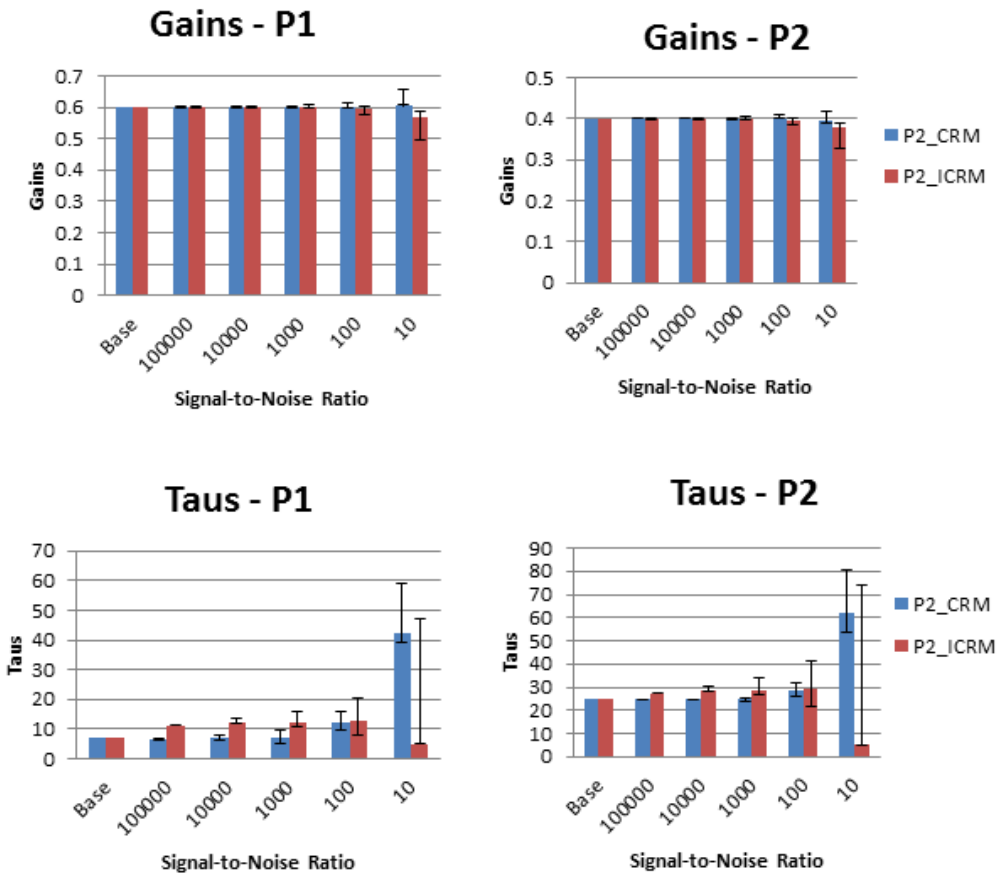

Figure 3.6: Parameters obtained for different noise levels in injection data

impact the value of and uncertainty in parameter estimates. This insensitivity of CRM and ICRM to noise in injection data appears to be a consequence of the first order nature of the models, which becomes obvious when the models are written in a transfer function notation in the Laplacian domain. The first order nature of these models enables them to act as low-pass filters, in which noise (essentially high frequency fluctuations) is dampened out or attenuated, such that the noisy part of the data does not affect parameter estimation.

3.4 Conclusions

In this work, an assessment of the impact of noisy data on parameter estimation using CRM and ICRM was presented. The focus was on investigating the deviation of parameter estimates from the true (i.e., base case) values as well as the change in uncertainty of parameter estimates in two scenarios: first, when noise is present in the production data only, and second, when noise is present in the injection data only. Our results show that production noise present to a level where SNR is below three orders of magnitude leads to significantly inaccurate parameter estimates, more so for the ICRM than the CRM. Additionally, we found that injection noise has little influence on the accuracy of parameter estimates for both models because of their nature as low pass filters.

The insights on the impact of noise in production data on parameter estimation lead to a conclusion that the ICRM would be more advantageous relative to the CRM for datasets with SNR levels above 1000. Given that

the ICRM is linear, it requires significantly less computational effort and time to achieve results of better or comparable quality. Hence, for datasets with the appropriate level of cleanliness, ICRM may provide the cheaper and faster means to characterize a reservoir. Alternatively, in cases where the SNR is below three orders of magnitude, prior data cleaning would be necessary to achieve fast and accurate estimation with ICRM.

For higher estimation accuracy in cases where SNR is below 100 and data cleaning tools are not readily available, the CRM would be the better option. The model is less sensitive to noise relative to ICRM below this threshold and hence produces more accurate estimates, even when there is a significant amount of noise in the dataset.

Chapter 4

Denoising of Data for Parameter Estimation Applied to Petroleum Production

4.1 Introduction

Big Data continues to find application in diverse scientific disciplines. For example, modern drilling facilities are massively instrumented with sensors gathering abundant process data that carry on-time process information. However, one factor that continues to stymie its adoption within the oil and gas space is the adverse impact of noise in data. Because of mechanical and/or human errors, field data may contain between 2–20% noise ([16],[7]). Reservoir characterization using data-driven reduced order (RO) models, a viable area for Big Data application, typically produces estimates that are influenced by the quality of the input data. Thus, for dynamic, data-driven transfer function models like those of the Capacitance Resistance Model (CRM) family [29],[47] significant levels of noise may lead to inaccurate parameter estimates, resulting in mischaracterization of the oil reservoir system. This adverse impact of noise on parameter estimation using CRM has been demonstrated in the chapter 3.

Denoising, which can be defined as the removal of the noisy component of a raw signal while preserving the important non-noisy component,

is therefore often necessary when characterizing reservoirs using CRM. This chapter presents simple, yet effective denoising strategies that may be applied to preprocess oil field data before CRM application. This study indicates that appropriate denoising results in significant improvements in data quality, which in turn facilitates accurate parameter estimation.

The rest of this chapter is organized as follows: Section 4.2 presents the approach pursued in this work. The three denoising strategies demonstrated in this chapter are presented and discussed in Section 4.3. In Section 4.4, the results are presented, accompanied with analysis of the findings. Section 4.5 concludes the chapter with a summary of key findings.

4.2 Approach

The preceding chapter has demonstrated the adverse influence of noise, particularly at SNR levels below 100, on parameter estimation using the CRM. In this work therefore, different denoising techniques are applied to production data with SNR levels ranging from 10 to 100 to increase parameter estimation accuracy post-denoising. In addition, the performance of the different denoising strategies are compared to understand which are more suitable for CRM application and what conditions are most effective.

This work considers a small reservoir system composed of one injector (I1) and two producers (P1 and P2). Such a system essentially represents a single input, two output transfer function model more familiar within signal processing and control. The CRM, which represents a first order transfer func-

tion model, captures the interaction between input i and output j through two types of model parameters, the gain, f_{ij} and the time constant, τ_j. The CRM equation is shown in Equation 4.1. While the gains occur linearly, the model is nonlinear in terms of parameters because of the exponentially occurring time constant.

$$q_j^k = q_j^{k-1} e^{-\Delta t/\tau_j} + \left(1 - e^{-\Delta t/\tau_j}\right) \sum_{i=1}^{N_{inj}} f_{ij} I_i(t) \tag{4.1}$$

where τ_j is producer j's time constant and Δt represents time step between discrete times k and $k+1$

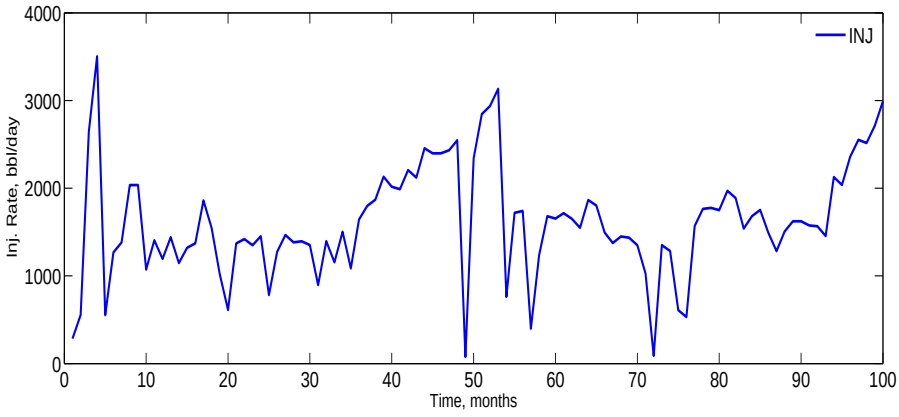

Figure 4.1: Injection rate data for production rate simulation

To obtain noisy data, the injection rate data shown in Figure 4.1 is applied to the CRM and a set of predetermined parameter to obtain the original (uncorrupted) production data for each of producer. This uncorrupted production rate, which forms the Base Case, is subsequently corrupted with

additive zero mean, white noise noise of increasing variance. The variance of the noise signal is scaled relative to the power of the production rate signal to yield noisy signals with SNRs ranging from 10 to 100. The injection signal in all cases remained uncorrupted. Figure 4.2 show the production rate profiles of both producers before and after noise addition for SNR = 10. Analogous plots for SNR levels 100, 75, 50, and 20 are included in Appendix B

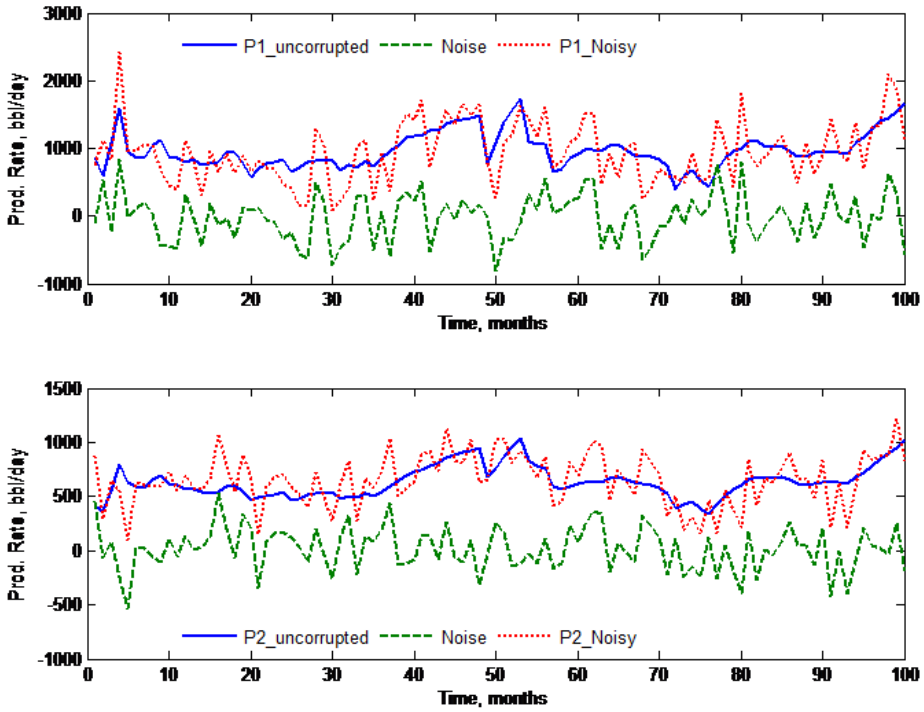

Figure 4.2: Production rate profiles of both producers before and after noise addition for SNR = 10

Each of the noisy datasets is fitted with the CRM (before and after

denoising) to obtain a corresponding set of parameter estimates and the associated 95% confidence interval for each estimate. To obtain these confidence interval estimates, a MATLAB-based bootstrapping algorithm is used. Details about bootstrapping and its application for CRM confidence interval estimation can be found in chapter 1 as well as in [20].

4.3 Digital Data-Driven Denoising Strategies

Digital data-driven denoising strategies, unlike the model-based ones, are useful when a priori knowledge of the process model is unknown. In such cases, denoising is done to reach a preset or desired level by approximating the filtered value of the current datapoint using previous measurements. Data-driven denoising strategies are suitable for preprocessing of well production rate data before CRM/ICRM application given the difficulty in integrating a full-order reservoir model into a model-based denoising strategy.

In this work, denoising of production data is demonstrated via three commonly used noise filtering strategies. The following subsections detail the basics of the filtering algorithms used.

4.3.1 Exponential Filter

The exponential low-pass filter is a simple and effective method used for damping out high-frequency noise, and its digital form can be described by Equation 4.2.

$$\hat{y}(k) = \theta y(k) + (1-\theta)\,\hat{y}(k-1) \tag{4.2}$$

where $\hat{y}(k)$ and $y(k)$ stand for filtered measurement and (raw) data respectively at discrete time step k, and $\theta(0 < \theta \leq 1)$ is a tuning parameter that weighs the current and previous filtered samples.

The operation described in Equation 4.2 is also called the exponentially weighted moving average (EWMA) filter. While $\theta = 1$ corresponds to no filtering, a decreasing value of θ weakens the influence of process measurements [59].

4.3.2 Savitsky-Golay (SG) Filter

The Savitsky-Golay (SG) finite impulse response (FIR) low-pass filter [54], also known as polynomial least-square smoothing filter, has been widely used to increase the signal-to-noise ratio without significantly distorting the signal. The general idea of the SG filter is to use polynomials fitted by local adjacent data points for smoothing purposes [49].

Considering a data sequence , at a certain moment in time, we can obtain $2N+1$ samples centered at t=0, which can be used to fit the following k^{th} order polynomial with a minimized residual:

$$Q_t = \sum_{i=0}^{k} a_k x^k; -N \leq x \leq N \tag{4.3}$$

where the coefficients a_k are obtained through minimizing the following approximation error:

$$E_m = \sum_{t=-N}^{N} (Q_t - y_t)^2 = \sum_{t=-N}^{N} \big(\sum_{i=0}^{k} a_k x^k - y_t \big)^2 \tag{4.4}$$

4.3.3 Wavelet-based Filter

The Fourier transform has been widely used in signal processing to perform frequency analysis, as defined in the following equation:

$$F(f) = \int_{-\infty}^{\infty} f(t)\, e^{-2\pi i f t} dt \tag{4.5}$$

The term $e^{-2\pi i f t}$ carries frequency information through parameter that can be used to design digital filters, such as low-pass and band-pass filters [49]. However, in the above equation, the time information represented by t is lost after integration, and we can no longer observe the change of frequencies with time. To overcome such a problem, wavelet transform can be used, and the mother wavelet function is used to replace $e^{-2\pi i f t}$, as shown in Equation 4.6:

$$\psi_{a,b}(t) = \frac{1}{\sqrt{a}} \psi\big(\frac{t-b}{a}\big) \tag{4.6}$$

where a is the scale parameter containing frequency information and b is the shift parameter preserving the time domain information. The simplest mother wavelet function is the Haar wavelet defined in Equation 4.7:

$$\psi_{a,b}(t) = \begin{cases} 1, & 0 \leq t < \frac{1}{2} \\ -1, & \frac{1}{2} \leq t < 1 \\ 0, & \text{otherwise} \end{cases} \tag{4.7}$$

The wavelet transformation [37] can be used in filtering noise: the signal is first decomposed into coefficients at different scales which can be considered as a variety of frequency bands. Decomposition can be of one or multiple levels depending on the nature of noise present in the data and the desired level of denoising targeted. Second, the wavelet thresholding is performed on the coefficients to keep the desirable information. In the last step the processed signal is then transformed back into the time domain to obtain a clean signal.

4.4 Results and Analysis

4.4.1 Comparison between SG, Exponential, and Wavelet Filters

Here the effectiveness of the filters used in this work to denoise production data is compared. History-matching of production data before and after denoising is performed to observe the level of fit each of the filters is able to achieve. Furthermore, to quantify performance, we calculate the coefficient of fit (R^2) between the denoised (at each SNR level) and uncorrupted signals and compare with that of the noisy signal. A general improvement in the R^2 value after denoising is expected because removal of noise, while preserving the useful component of the signal, should align the denoised signal closer to the uncorrupted signal.

For the SG filter, a cubic polynomial was used. At each time step, a

frame size of seven data points was used to fit the filter polynomial for producer P1. For P2, the frame size used was 11. For the exponential filter, the tuning parameter, θ, was set at 0.72 and 0.55 for P1 and P2 respectively. Different frame size and θ values were used to accommodate the different power of the noise signals present in the different producers. The frame size and θ values used in this case were determined via a crude optimization exercise in which these filter parameters were varied to maximize filter performance. A detailed sensitivity analysis of the impact of these filter parameters is presented in subsection 4.4.2.

The coefficient of fit, calculated via Equation 4.8, is used to compare production signals before and/or after denoising, to the original (uncorrupted) production data. This coefficient, ranging from 0 to 1 quantifies the deviation of the denoised signal from the original. A coefficient of fit value of 0 signifies complete loss of the original signal, while a value of 1 indicates complete removal of noise without distortion of the original signal. The relative expansion/contraction of confidence intervals for CRM parameters resulting from denoised quantifies change in uncertainty due to denoising.

$$R^2 = 1 - \frac{SS_{res}}{SS_{tot}} \tag{4.8}$$

where SS_{res} is the residual sum of square errors between the denoised and original signals, while SS_{tot} is the total sum of squared errors.

Figure 4.3 compares production rates for P1 and P2 before and after

denoising to the uncorrupted production sequence at SNR = 10. Analogous plots for SNRs between 20 and 100 are presented in the Appendix B

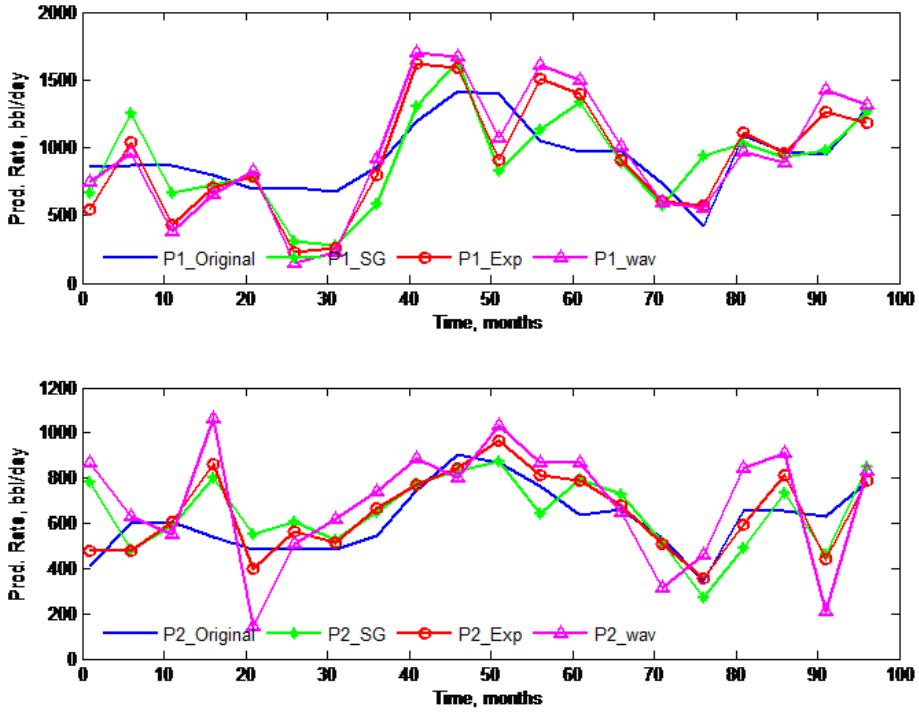

Figure 4.3: Production rate profiles of both producers before and after denoising for SNR = 10

In Figure 4.3, we see that noise filtering generally introduces smoothening of the production data by minimizing spikes. This observation is intuitive - because the filters are low pass filters, removal of noise, i.e., the high frequency component of the data, is accompanied by the removal of a portion of the signal's high frequency content. Thus, for segments in the data where changes

are gradual, close tracking of the original production signal was observed as opposed to segments with significant spikes, in which there is more mismatch. This mismatch is observed for all SNR levels and increases in severity as noise level increases.

Additionally, while all the filters perform similarly at relatively higher SNR levels, we observe better performance for the SG filter particularly at lower SNR levels. The signal denoised using the SG filter is seen, at each noise level, to have comparatively lower spikes. The SG filtered signal tracks better with the uncorrupted production signal. This observation is further demonstrated by a comparison of the R^2 values obtained after denoising by the different filters as shown in Figure 4.4. From the plots, we see that denoising improves the fit between the corrupted and uncorrupted signals, particularly with increasing noise content. We also observe slightly higher R^2 values for the SG filter, confirming the better performance and thus higher effectiveness of this filter at higher noise levels.

The SG filter performs better because of its ability to filter out noise while preserving the high frequency component of the signal that is useful. The superior effectiveness of SG filters among standard low pass filters like those of the moving average type is well established in the literature ([58], [61]) and is the provenance of the better match and higher R^2 values obtained when using SG filters. Thus, the results suggest the SG filter to be chosen over exponential and wavelet filters for production data denoising when possible. However, because SG filters are also known to be less effective in rejecting noise

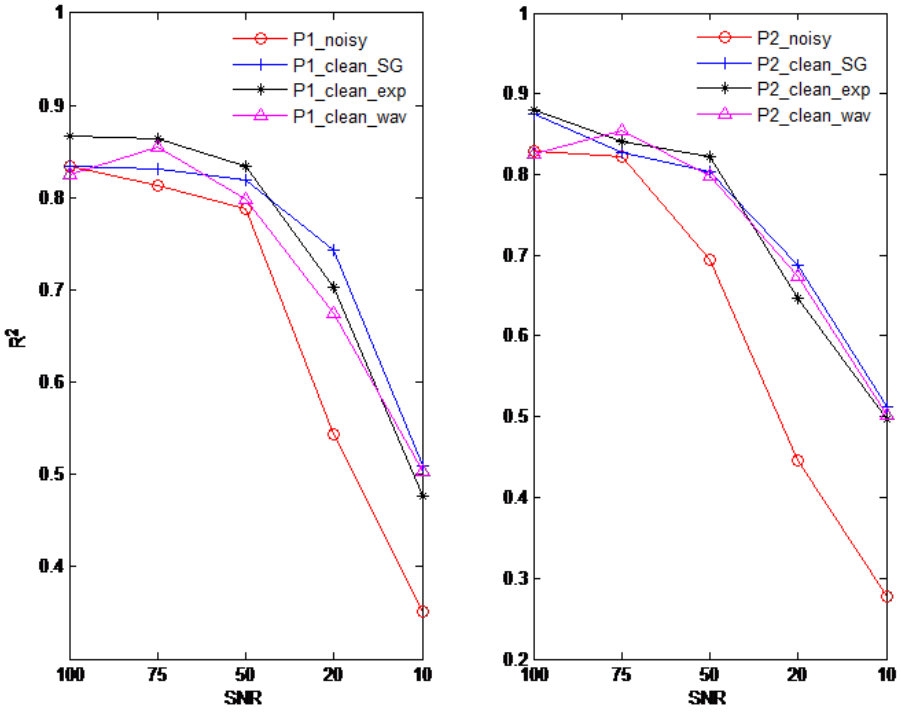

Figure 4.4: Filter performance as a function of noise level

in situations where the noise content is large [61], exponential filters, being simpler and a more effective moving average filter, may be more generally applicable in such scenarios.

4.4.2 Influence of filter structure

To understand the impact of filter structure on performance, we vary the value of the parameters that determine filter structure. For the two parameter SG filter, we implement denoising for four scenarios in which the filter polynomial was quadratic, cubic, quartic, and quantic respectively in each scenario. This was to observe the influence of the order of the filter polynomial on the R^2 value. Second, we implemented denoising for three scenarios using frame size of the 5, 7, and 9 datapoints respectively, with subsequent comparison of the resulting R^2 values. For the exponential filter, we varied the tuning parameter, θ, to demonstrate its influence on filter performance, as measured through the R^2 value. For brevity, the results and analyses are presented for producer P1 only but the insights generated are applicable to producer P2 as well.

For the wavelet filter, a Haar wavelet function, implemented in MATLAB®, was used and the decomposition level applied to the initial noisy production data was varied. Results presented for one, two, and three levels of decomposition demonstrate the influence of this parameter on denoising using wavelet filters. This work does not consider the influence of the choice of the mother wavelet function used because of the large number of options available for this

parameter. Therefore, an assessment of a finite set of this parameter may not generate results sufficient to develop a general understanding of its impact.

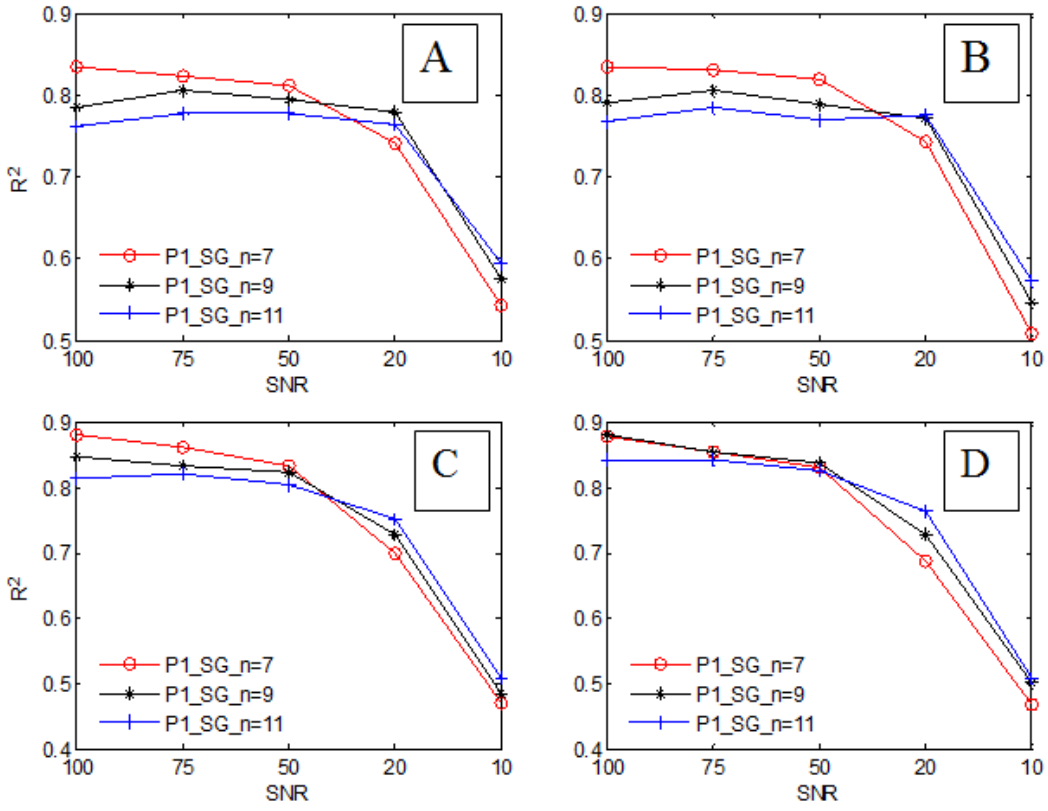

Figure 4.5: Impact of frame size on SG filter performance A) at filter polynomial order, k=2; B) at k=3; C) at k=4; D) at k=5;

Figure 4.5 shows the influence of the order of the filter polynomial, as well as that of the filter frame sizes for the SG filter. The plot shows that first, irrespective of the polynomial order, smaller frame sizes are more effective at relatively higher SNR level, and vice versa. This observation supports a choice of larger frame sizes in situations where noise content may be significant. Sec-

ond, we observe from the plot that performance for scenarios with polynomial orders, k and $k+1$, where k is even, is the same. Figure 4.6 better illustrates this observation, which is well supported in the literature [58]. The equivalent performance for filters with polynomial order k and $k+1$ suggests that where possible, lower order (and thus simpler) filters may be used to achieve results on par with slightly higher order ones. However, in general, a higher order filter performs better relative to a low order one at high SNR values

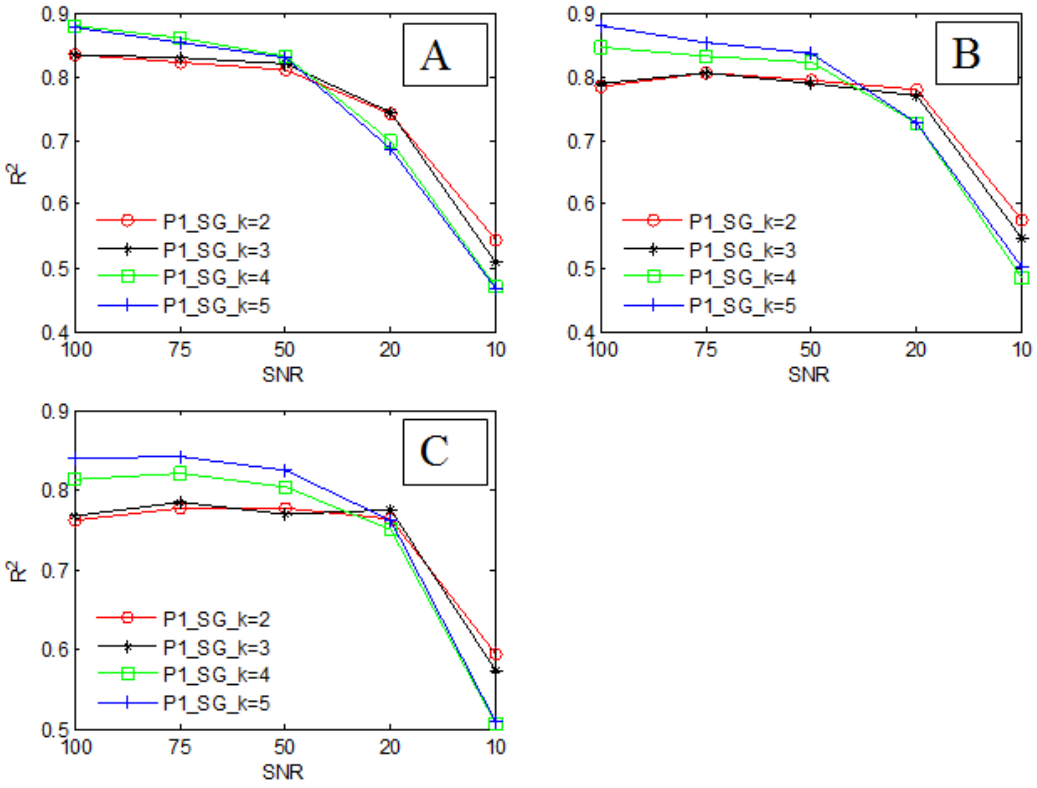

Figure 4.6: Impact of filter polynomial order on SG filter performance A) at frame size, $N = 7$; B) at $N = 9$; C) at $N = 11$

For the exponential filter, we considered three scenarios with values of 0.55, 0.75, and 0.95 respectively to demonstrate the influence of this tuning parameter on the R2 value. Results are presented in Figure 4.7.

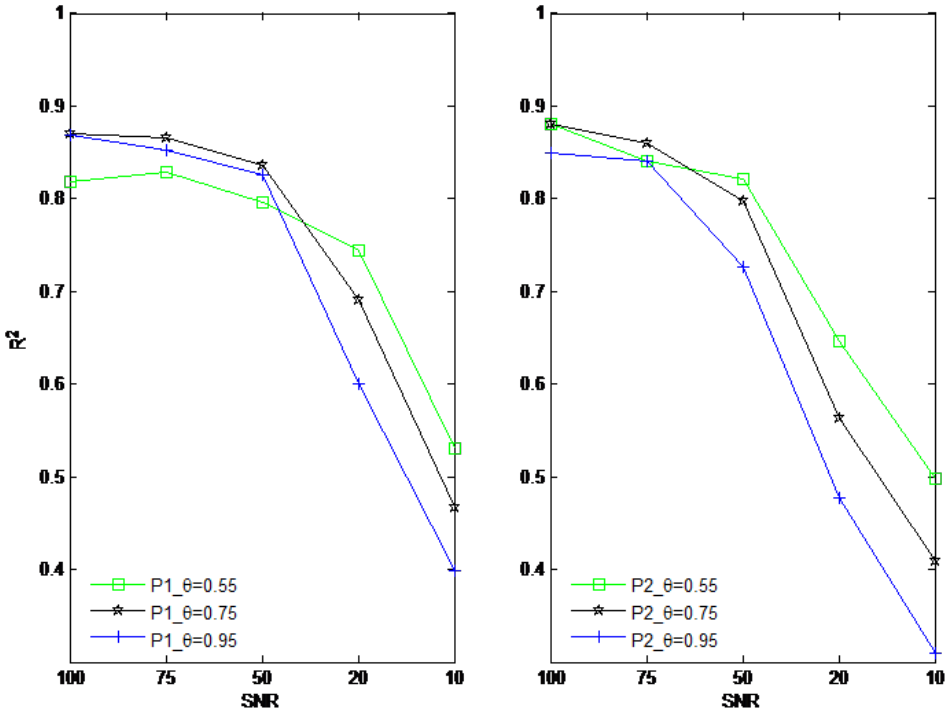

Figure 4.7: Influence of tuning parameter θ on exponential filter performance

Figure 4.7 shows R^2 value as a function SNR for the three above mentioned scenarios. The results show that the lower the value, the better the filter performance at lower SNR levels. This is primarily because filters with lower θ value are more aggressive in their removal of noise. This characteristic puts such filters at a slight disadvantage at high SNR levels when the noise

component in the data is small but makes them relatively more effective when the signal is significantly noisy (i.e., at high SNR levels). Because the impact of the tuning parameter is significant, careful selection or optimization of this parameter based on the noise content in the signal to be denoised is crucial.

For the wavelet filter, we considered three scenarios with decomposition levels of 1, 3, and 5 respectively to demonstrate the influence of this parameter on the R^2 value. Results are presented in Figure 4.8.

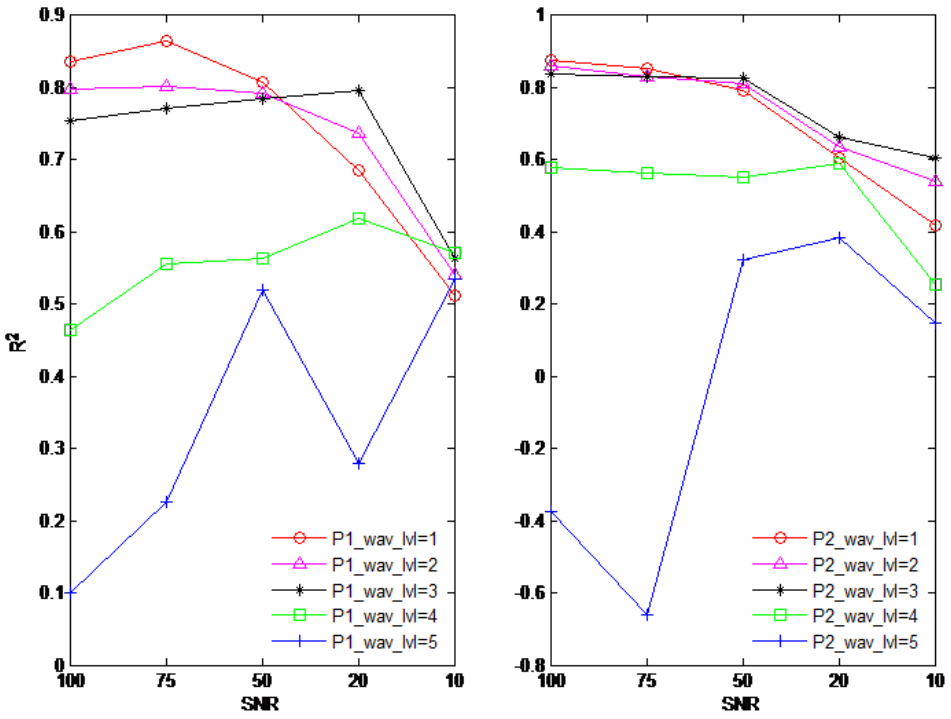

Figure 4.8: Influence of signal decomposition level for the wavelet filter

From Figure 4.8, two observations are apparent. First, for the signal

used in this study decompositions from levels 4 upwards yielded markedly poor results. This observation is pronounced at higher SNRs and reduces drastically at relatively lower SNR. Because denoising using the wavelet transform constitutes a thresholding of high frequency (detail) coefficients, multilevel decomposition with the attendant thresholding at each level increases the aggressiveness of noise removal. This results in a smoother denoised signal, devoid of the relics of the original signal and thus lowers R^2 values. This observation underscores the need for a careful determination of the decomposition level to avoid the over-smoothing of noisy signal during denoising.

Second, Figure 4.8 shows that for decomposition levels below 3, less decomposition is more appropriate at higher noise levels and vice versa. This finding is intuitive. When a significant amount of noise is present in the signal, higher decomposition levels only produces more opportunity for increased noise extraction. The opposite is the case for situations where little noise is present in the signal. In the extreme case of level 5 decomposition, denoising begins to encroach into the removal of valuable frequency attributes of the actual signal, which is the cause of the negative R^2 value. Consequently, basing the choice of decomposition level on *a priori* determined noise level in data or sequentially optimizing the decomposition value to yield the best fit are prudent approaches for effective denoising using wavelet filters.

4.4.3 Influence of Denoising on CRM Parameter Estimates

4.4.3.1 Influence on gains

Figure 4.9 shows the influence of denoising on gain estimates for producer P1. An analogous plot for producer P2 is included in Appendix B.

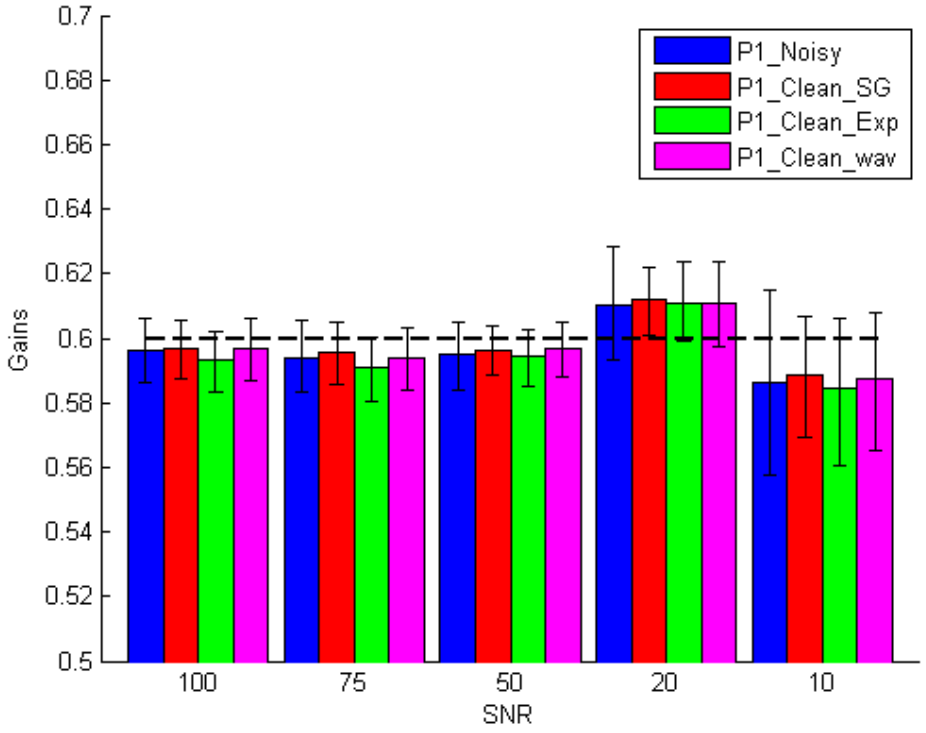

Figure 4.9: CRM gain estimates before and after denoising for different SNR values

From the bar graph, we see that denoising makes negligible on the value of gain estimates. This observation is consistent for both the SG, exponential, and wavelet filters irrespective of noise level. However, from close observation,

we see that denoising results in a tightening of the confidence interval estimates as noise level increases and especially for the SG filter. The relatively better performance stems primarily from the polynomial fitting process inherent to the SG filter, in which the slopes of the filter polynomial are made to match that of the signal at each time step [58]. Additionally, this process, which does not introduce a phase shift (unlike the exponential filter), results is a better preservation of the salient signal features, a higher R^2 value, and consequently, more certainty in gain estimates.

4.4.3.2 Influence on time constants

Figure 4.10 shows the influence of denoising on time constant estimates for producer P1. An analogous plot for producer P2 is included in Appendix B.

From Figure 4.10, we see that unlike the negligible influence of denoising on gains, the estimation of time constants is substantially sensitive to denoising. This observation is consistent with our previous studies that show a disproportionate influence of noise in a dataset on time constant estimation over gains. Because the time constants occur exponentially in the CRM (see Eq. 4.1 in Section 4.2), as opposed to the linearly occurring gains, these two parameter types show different sensitivities to noise, and consequently to denoising. Thus, the different denoising strategies that we have demonstrated show different levels of effectiveness in terms of time constant estimation.

While the denoising strategies led to tighter confidence interval, we ob-

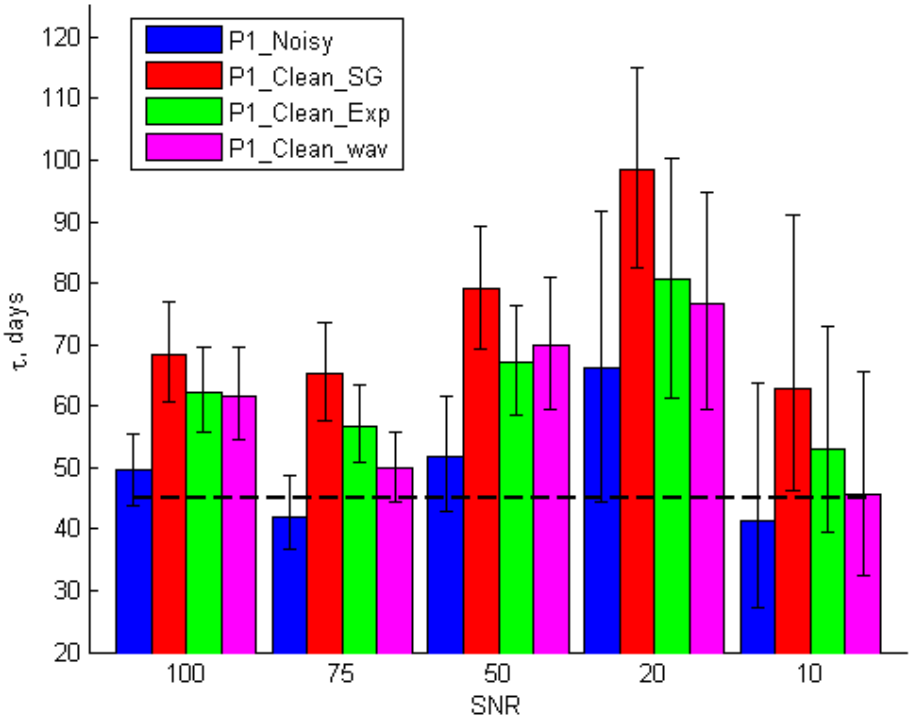

Figure 4.10: CRM τ estimates before and after denoising for different SNR values

serve that denoising is generally accompanied by significant drift of τ estimates from the original value. This observation suggests that the high frequency component of production signal is more influential in the estimation of time constants, which then explains a worsening of performance as this component of the data is removed alongside noise during denoising. This drift of τ estimates seems to reduce dramatically at very high noise levels, because the over representation of noise in the corrupted signal ensures that the majority of what is removed is noise.

Figure 4.10 also shows that denoising using the SG filter introduces the most deviation in τ from original values, but the tightest confidence interval estimate, relative to the wavelet and exponential filters. A consideration of the frequency domain characteristics of the filters offers an explanation. While the SG filter is attractive because of its extremely flat passband, this filter, unlike the exponential filter, only features a modest attenuation in the stopband [58]. Thus, even though some of the high frequency component of the original signal is being removed during denoising, the noise itself is not entirely removed, leading to the slight amplification of the noise effect on τ estimation. While this deviation is a trade-off worth considering when denoising production data for CRM application, we note that denoising may still be beneficial even when the deviation in τ estimates is significant because CRM history-matching has been shown to be less sensitive to τ values.

4.5 Conclusions

In this chapter, the use of simple digital filters to clean production data before CRM application was demonstrated. The performance of the three filters used was compared to understand the impact of key filter parameters on filter performance and on CRM parameter estimation accuracy. The findings lead to the following conclusions:

- Denoising of production data improves data quality because it leads to smoother data that better matches the original signal. This is demonstrated by the increase in R^2 values after denoising.

- The SG filter may be preferential over EWMA and wavelet filters for production data denoising, particularly when noise content is low. When the opposite is the case, EWMA filters, being simpler and a more effective moving average filter, may be a better choice.

- For the SG filter, a choice of larger frame sizes in situations where noise content may be significant seems to be more effective. Contrastingly, higher order filters were observed to perform better at higher SNR levels, making a case for an optimal selection of filter order and frame size during SG filter design.

- For the EWMA filter, the tuning parameter θ is influential. Our findings indicate that at high noise levels, filters with smaller θ values are more effective than those with high values. The relatively higher aggressive

nature of the EWMA filter at lower θ values makes them better suited for significantly noisy datasets. However, this ability could easily turn into a disadvantage when noise levels are low.

- For the wavelet filter, we observed that the decomposition level is a significant parameter that must be chosen carefully to avoid over-smoothing. Particularly when SNR levels are high, low decomposition of a noisy signal is more prudent as multilevel decomposition accompanied with thresholding of high frequency decomposition coefficients may lead to excessive filtering and encroachment into the signal's frequency intervals that are actually relevant.

- While denoising improves the certainty in the CRM parameter estimates (as demonstrated by a tightening of the confidence interval), it may also lead to a deviation of time constant estimates from the true values. This is a potentially adverse consequence that the practitioner should consider while designing or using digital filters for production data preprocessing. However, this deviation may overall be a minor disadvantage since CRM fittings are known to be less sensitive to τ values.

Chapter 5

Design of Optimal Injection Signals for CRM Parameter Estimation

5.1 Introduction

For proper implementation of either the CRM or the ICRM, the data to be fitted is required to be sufficiently rich [27]. This raises two important questions. First, what is an appropriate measure of data richness? That is, how can the richness of a dataset be quantified such that data for/from different systems can be easily compared? Secondly, by which method can a dataset that is sufficiently rich be constructed? Questions like these are relevant when it is necessary to determine the optimal amount of external excitation required to construct informative data [43].

In general, the quantification of the information content (or informativeness) of a signal is done via a concept termed degree of richness. According to Mišković et al. [43], a signal is said to be sufficiently rich of degree n if it possesses a spectral density that is nonzero in at least n distinct frequency points within the bounds of $\big(-\pi,\, \pi\big]$. On the basis of this definition, it can be said that a signal is only as rich as the number of distinct frequency components in it's power/amplitude spectrum. Therefore, decomposition of any

optimized signal to observe the number of frequency components present in it is an important step towards validating the effectiveness of any input design methodology.

The problem of input design has been of much interest for the past four decades. The high level of interest is explained by the necessity of exciting physical systems with the appropriate input signal, which is fundamental for the optimal identification of these systems [40]. The vast majority of literature on this problem has approached it from a DOE standpoint, a topic upon which much work has been presented particularly within statistics and engineering literature [40]. This work will follow suit and will also approach the optimal input design problem using experimental design techniques.

The rest of the chapter is organized as follows: Section 5.2 introduces the methodology for this work. Section 5.3 presents three validation cases for the input design method developed here. Section 5.4 concludes the chapter with a brief summary of key findings.

5.2 Method

While scientific literature abounds with sufficient conditions for the design of input signal of optimal richness [43], inputs for reservoir systems have received little attention. One reason for this deficiency have been the relative paucity of mathematical, first principle reservoir models that requires the perturbation of the reservoir system (and the information contained therein) for its identification. Additionally, data-driven models like the CRM are devel-

oped and typically used in the industry to optimize production for profit and not for the information content.

An attempt to design injection rates with the goal of maximizing their information content was made by Moreno and Lake [44]. In this work, a time domain approach was adopted. According to the authors, this choice was made to facilitate the incorporation of input constraints. Also, the optimal injection strategy was found to be a bang-bang injection scheme when the injection rates took on upper and lower bound. In a case were the total injection rate was constrained, an injection rate sequence having a piecewise constant profile was determined to be optimal. An E-optimality criterion, in which the largest eigenvalue of the Fisher information matrix (FIM) is maximized, was used. In conclusion, two examples, one for each type of constraint, were presented.

This work adopts a time domain approach. While it is true that optimization in the frequency domain provides a cheaper route, in terms of computational effort, the inflexibility of frequency domain design to inputs beyond sinusoids is a major drawback that makes frequency domain approach impractical for our system. Additionally, it is well known that injection rates in oil fields are bounded by physical and operational constraints. Thus, to be of practical significance, any input design must be capable of taking into account the necessary constraints. Because an appropriate method for constraining rates in a frequency domain framework remains unclear, the time domain approach, in which straightforward incorporation of constraints has been demonstrated in several publications, will be used.

The P-optimal criterion, in which the principal components of the covariance matrix are minimized, is used in this work. This optimality criterion was introduced by Zhang and Edgar [75] in their 2008 publication, where they used it to design inputs and sampling time for differential and algebraic systems. The P-optimal design method has been shown to being a more general case of other frequently used design criteria such as SV-optimal, D-optimal, and E-optimal criteria. Thus, this method essentially combines the advantages of the above mentioned design methods. Additionally, the prior use of principal component analysis (PCA) to decompose the information matrix enables it to handle, unlike other design criteria, situations where the condition number is relatively large. Thus, the P-optimality criterion is well suited for this work where the information matrix is often ill-conditioned.

Further, it is well known that a useful component of input design and optimization in discrete signals is the determination of optimal sampling rate. According to Zarrop et al. [74], the maximum return from an experiment (in this case an input design) cannot be achieved unless a joint optimization of both the frequency spectrum as well as the sampling rate of the input is implemented. Zhang and Edgar [75] have shown that the coupled design of both input and sampling rate is readily performed using the P-optimal design criterion. Thus, the P-optimality criterion, which easily lends itself to sampling rate optimization seems an appropriate choice for injection rate design. This work however focuses only on injection design through frequency spectrum optimization as the impact of sampling rate on CRM parameter estimation

has been considered in previous research [68].

To execute the P-optimal design of injection rates, the design matrix, which is formed to reflect the input signal for each injector over the fitting period, is constructed and initialized. Using the design matrix, the sensitivity matrix, J, is then calculated. This sensitivity matrix indicates the influence of a unit change in parameter value on the model performance and is calculated through Equation 5.1

$$J(k) = \frac{dq_t(k)}{d\theta} \tag{5.1}$$

where $q_t(k)$ is the total production rate at timestep k, and θ is a matrix (or vector for a one-producer system) of model parameters.

The information matrix is calculated as a product of the transpose of the sensitivity matrix and the sensitivity matrix itself. This resultant matrix, also called the Fisher Information Matrix (FIM), is calculated via Equation 5.2.

$$M = J^T \times J \tag{5.2}$$

Using the singular value decomposition (SVD) technique, the FIM is decomposed into eigenvector and eigenvalue matrices. The diagonal elements of the eigenvalue matrix represent the principal components (PCs) of the FIM, typically arranged from highest to lowest. Zhang and Edgar [75] demonstrated the equivalence of SVD and PCA for real and symmetric matrices such as the FIM. The eigenvalue matrix is then inverted to yield the prediction error (or

parameter) covariance matrix, which represents the difference between model prediction and data.

An objective function, F, representing the total information content in the FIM, is calculated and maximized in a least square sense. This is equivalent to minimizing a certain scalar criterion of the covariance matrix such as the determinant or the largest eigenvalue, for example. These optimality criteria are discussed in [75].

The objective function used in this work corresponds to the P-optimality criterion and is shown in Equation 5.3. This objective function optimizes input for all model parameters. The P-optimal design method also permits a focused design for one or a select number of model parameters. In such a case, the objective function is formulated to include only the (s) retaining information about the parameters of interest. The objective function for this targeted optimization routine, say for s number of parameters, is presented in Equation 5.4.

$$F = min \prod_{i=1}^{m} \left(a_i \sum_{1}^{m} P_{ji}^2 \right) \tag{5.3}$$

where m is the number of optimal PCs to be used, a_i are the eigenvalues of the covariance matrix, and P_{ji} is the corresponding eigenvector matrix.

$$F = min \prod_{i=1}^{m} \left(a_i \sum_{1}^{s} P_{ji}^2 \right) \tag{5.4}$$

The P-optimal design method is summarized in Table 5.1.

Step	Description
1	Initialize model parameters and design matrix
2	Using initial model parameter values, calculate sensitivity matrix via Equation 5.1
3	Calculate the Fisher Information Matrix (FIM) via Equation 5.2
4	Decompose FIM to obtain eigenvector and eigenvalue matrices and invert to obtain the prediction error covariance matrix
5	Select model parameters to be designed for and the corresponding PCs, if necessary, and optimize objective function calculated via Equations 5.3 or 5.4 accordingly
6	Validate designed input via comparison with unoptimized and by frequency spectrum assessment

Table 5.1: P-Optimal Algorithm Description

5.3 Implementation of the P-optimal Design Method

The P-optimal design approach is demonstrated for 3 different cases:

- **Case 1**, only gains considered for a one producer system
- **Case 2**, gains and time constants considered for a one producer system
- **Case 3**, gains and time constants considered for a multiwell system

These cases are selected to demonstrate different aspects of the design approach. The first two cases demonstrates design for a one producer system, with the first case considering design for the gains only, and the second addressing a joint design for both gains and time constants. The third case illustrates joint gain/time constant design for a system with multiple injectors and producers.

5.3.1 Case 1: Only gains for a one producer system

In this case, design of injection rates was performed for a five-injector-one-producer system using the P-optimal criteria. The well layout is as shown in Fig. 5.1 The total design time was two years or 24 iteration time steps. The design variables were the injection rates for each of the five injectors at each time step i.e, 120 decision variables in total.

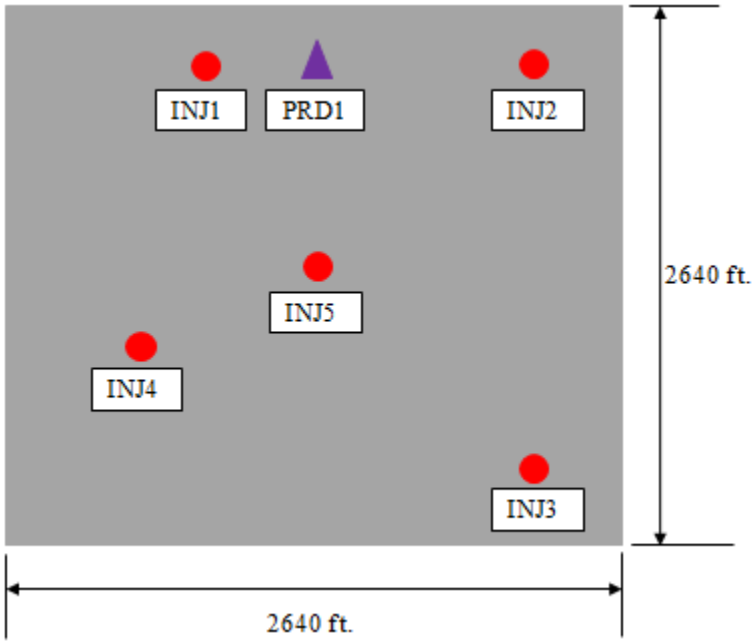

Figure 5.1: Well location map for Case 1

The injection rates were constrained between 250 STB/day and 2500 STB/day. This choice of upper and lower bounds, while arbitrary, was enforced to replicate the constraints on water injection in real fields. Since it is operationally undesirable to have large surges in the injection rates, an addi-

tional constraint was added to limit increases in injection rates to at most 500 STB/day. Input designs were done for the estimation of gains only.

Figure 5.2 shows the optimized injection rates. From the results, it is apparent that the optimal inputs are multi-level and not bang-bang. This profile stems from the necessity to excite different modes of the system while satisfying the different constraints imposed. The multi-level nature of the inputs agrees with the examples in [75] but differs significantly from that included in [44]. Apart from the difference in design criteria between this work and Moreno's, another main reason for the disparity is the penalty term present in Moreno et al.'s objective function which penalized switching and therefore encouraged a min-max injection profile.

According to Zarrop [73], the two conditions necessary for persistent excitation are non-singularity of the information matrix as well as the existence of at least int [p/2] (and not more than $\big(p\times(p+1))/2\big)+1$) lines in the signal's frequency spectrum (where p is number of parameter). To confirm the first requirement is satisfied for the designed input sequence, the condition number of the information matrix resulting from the optimized profile was compare with that of the initial. The results are presented in Table 5.2.

	Condition Number
Unoptimized	1.32×10^{17}
Optimized	50

Table 5.2: Condition Number for Case 1 before/after Input Design

Table 5.2 shows that through input design, a decrease in condition

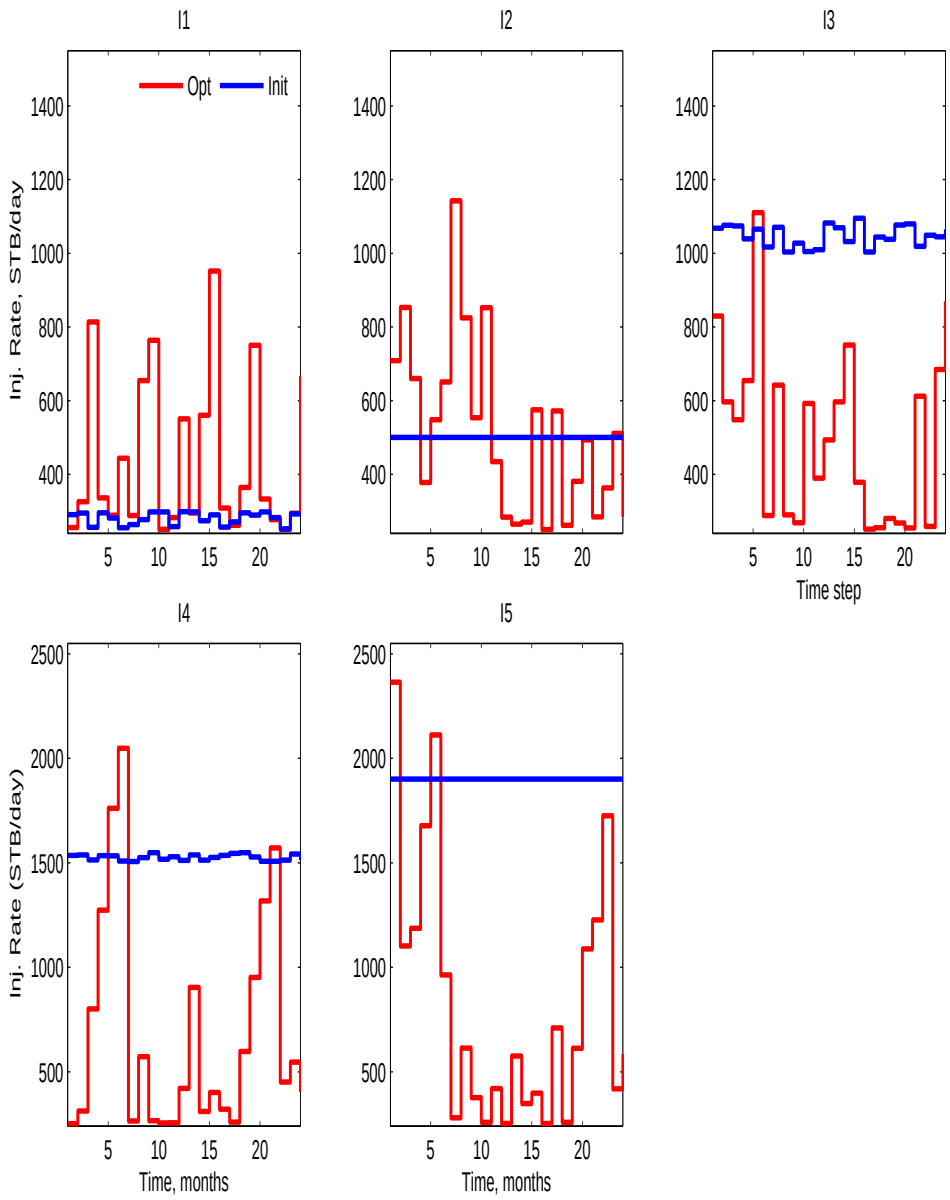

Figure 5.2: Optimized injection profile for Case 1

number from 1.32×10^{17} to 50 was observed. This illustrates the high robustness of this method, proving the relative well-conditioning of the optimized information matrix. Further, to determine whether the second necessary condition for persistent excitation is met, the optimized signals were decomposed into their constituent frequencies using discrete Fourier transform (DFT). The single-sided amplitude spectrum is plotted in Figure 5.3.

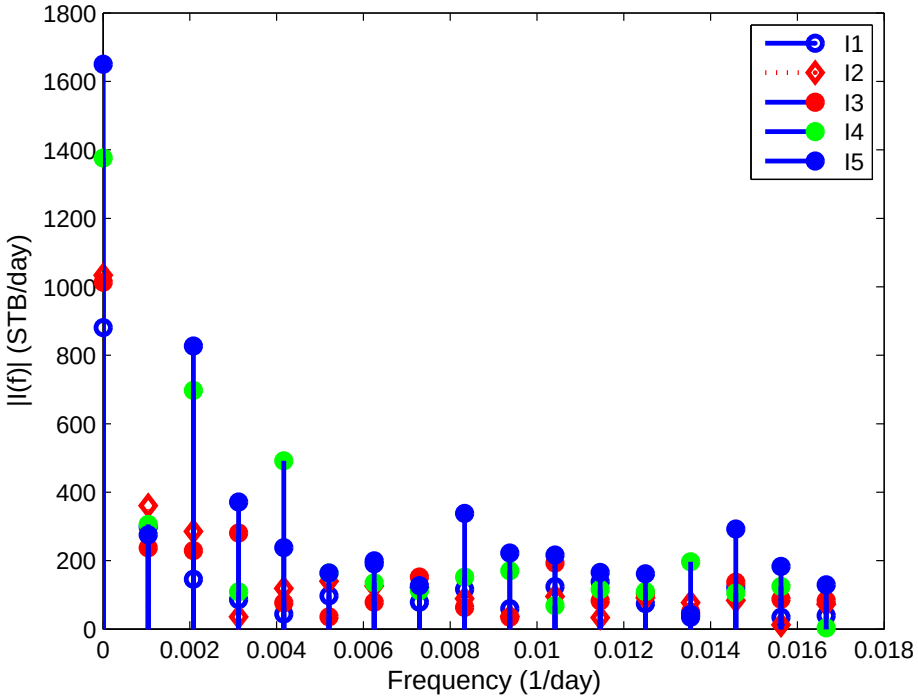

Figure 5.3: One-sided amplitude spectrum of optimized injection profile

The plot shows that the number of non-zero frequency points in the optimized spectrum (16 in this case) did exceed the minimum required (i.e, 3) and was below the maximum (i.e, 22). This observation, when combined with

the low condition number resulting from the P-optimal design, confirms that the design method yields persistently exciting signals.

To validate the optimized signals, simulation was performed comparing the designed signals with unoptimized, randomly generated pseudorandom binary sequences (PRBSs). The unoptimized PRBS are shown in Figure 5.4. Both signals were used to simulate production data through the CRM, using predetermined gains and time constant. The production data was then corrupted with 10% noise to replicate measurement noise prevalent in production data. These production data are shown in Figure 5.5. The corrupted data are fitted using the CRM and parameter estimates obtained and analyzed.

The results of this validation effort are presented through Figure 5.6. This figure shows the history-matching results for both optimized and unoptimized datasets and the corresponding R^2 values.

From Figure 5.6, it is apparent that the data generated using the optimized signal yields a better match relative to the unoptimized despite both being corrupted with the same level of noise. Because the optimized signals are persistently exciting, signal power is concentrated at the frequencies that are necessary for accurate estimation. The unoptimized PRBS, being a random sequence, has signal power evenly spread through all the frequencies and therefore does not prioritize the more relevant frequencies. This is further demonstrated through Figures 5.7 and 5.8, which show the values of the original parameters, the optimized ones, and the unoptimized.

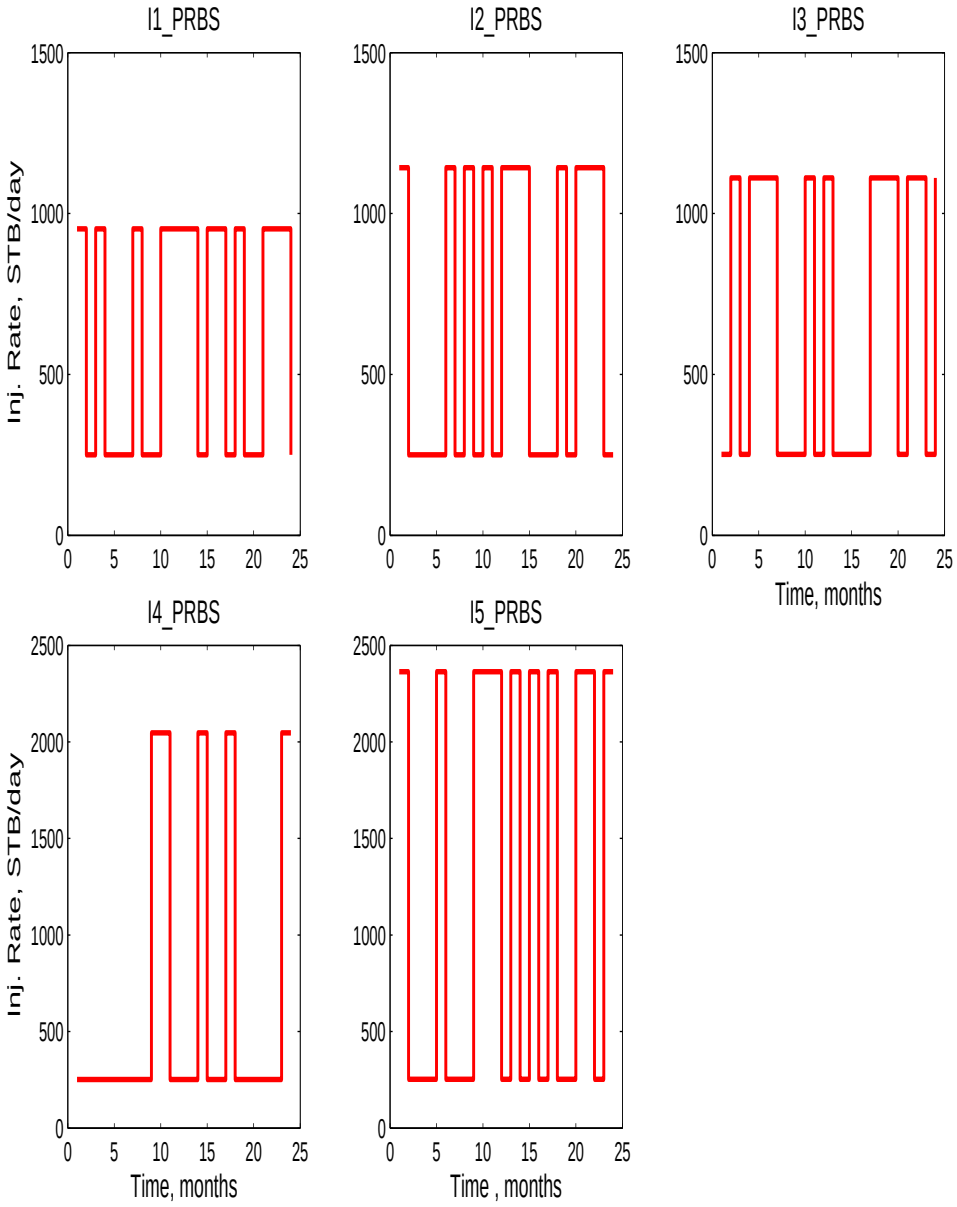

Figure 5.4: Unoptimized PRBS injection rates for Case 1

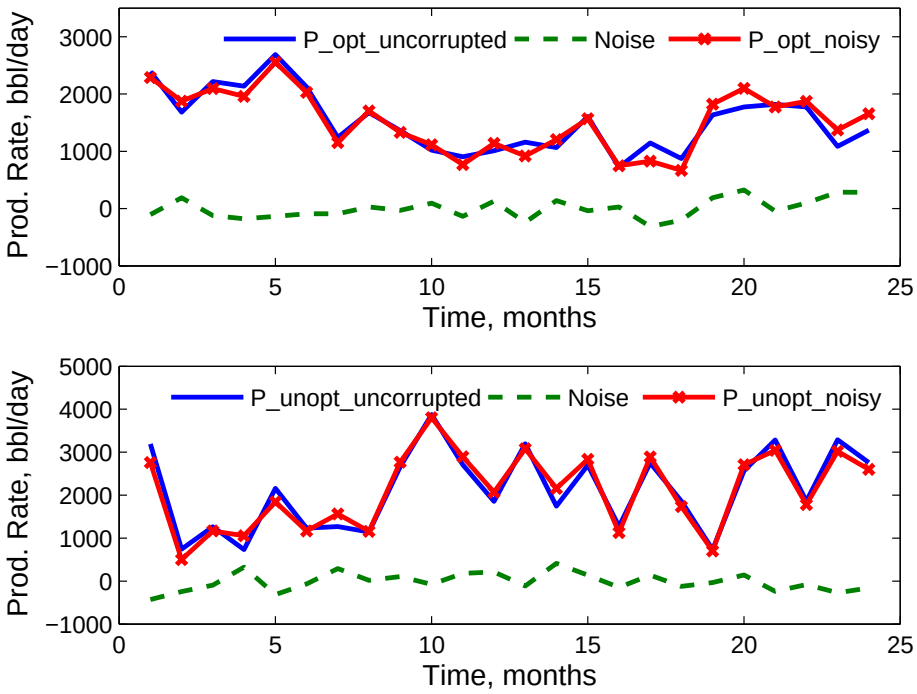

Figure 5.5: Production data simulated using optimized and unoptimized injection rates

	f1	f2	f3	f4	f5	τ (days)
Original	0.78	0.56	0.10	0.21	0.33	15
Optimized	0.87	0.50	0.16	0.19	0.31	15.62
Unoptimized	0.76	0.65	0.02	0.29	0.28	17.65

Table 5.3: Original parameter estimates compared with those from optimized and unoptimized injection rates

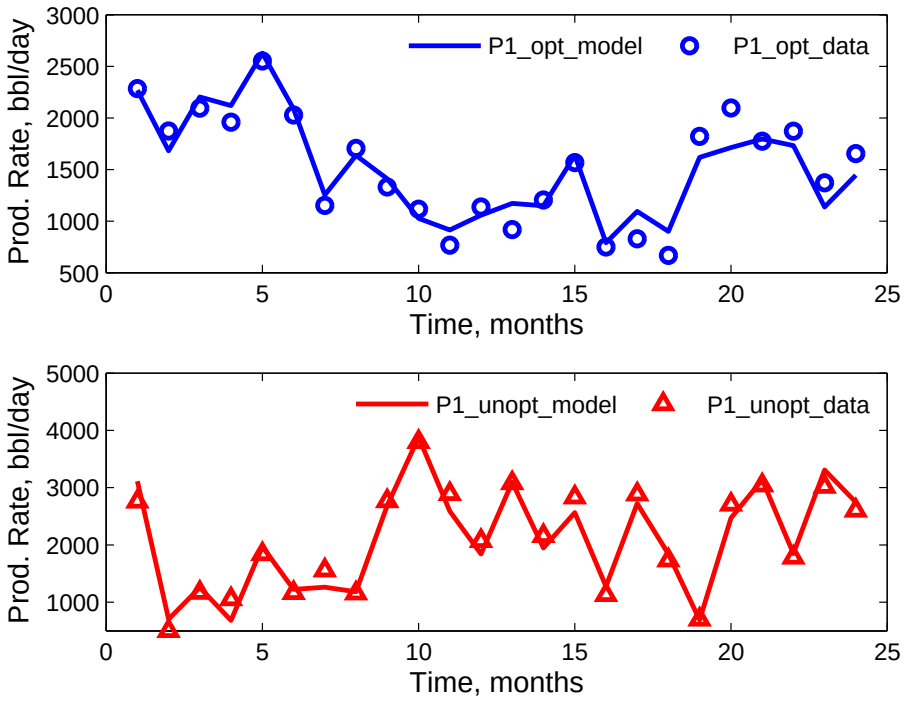

Figure 5.6: Historymatching results for optimized and unoptimized injection rates

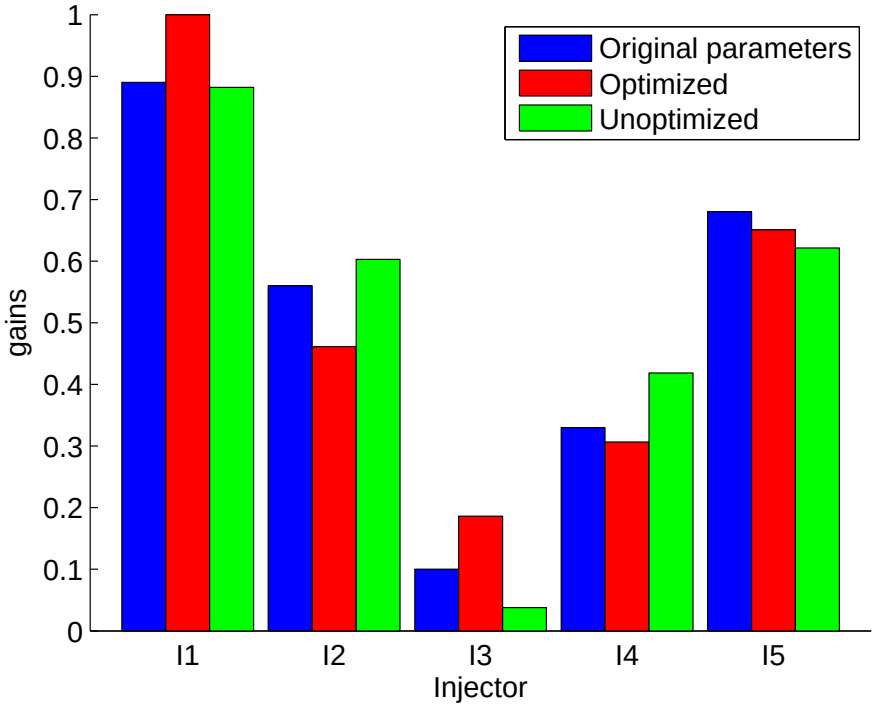

Figure 5.7: Comparison of gains from optimized and unoptimized injection rates to original

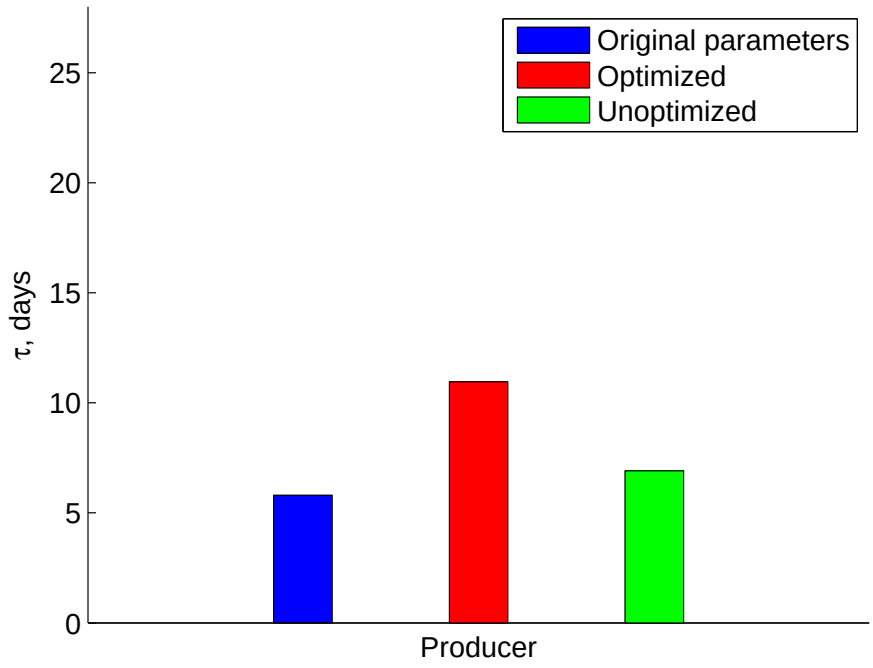

Figure 5.8: Comparison of τ estimates from optimized and unoptimized injection rates to original

Figures 5.7 and 5.8 visualize the comparison of the parameter estimates, obtained using optimized and unoptimized inputs, that are presented in Table 5.3. Figure 5.7 shows that the gains, obtained from the optimized data are generally closer to the original relative to those obtained using the unoptimized data. The greater proximity of these parameter estimates to their true value results in the better fit and higher R^2 value observed in Figure 5.6. This positive impact of injection design on the gains supports its prior implementation, when possible, in reservoir system where accurate reservoir characterization is a priority.

Figure 5.8, however, shows that while the gains from the optimized data perform better, the time constant does not. Because the injection rates were not optimized for the time constant, the power of the injection signals is distributed such that they excite frequency modes necessary for gain estimation at the expense of the time constants. As a consequence, the unoptimized signal is seen return time constant estimates closer to the original value.

5.3.2 Case 2: Gains and time constant for a one producer system

Like in the previous case, design of injection rates was performed for a five-injector-one-producer system using the P-optimality criterion. The well locations, design conditions, and constraints were the same as in the previous case. However, inputs were designed for both gains and time constant estimation. The design matrix involved a calculation of the derivative of the production rate relative to the time constant. This necessitated *a priori* knowl-

edge of the model parameters to be optimized for, suggesting the need for a sequential optimization routine.

The results of the injection optimization is as shown in Figure 5.9. This plot shows the optimized injection rates. Like in the previous case, the optimal inputs are multi-level, indicating an excitation of the different frequency modes of the system. The optimized signals are checked for persistent excitation by calculating the condition number of the information matrix before and after optimization. The condition number was found to decrease from 1.32×10^{17} to 2.11×10^{4}, signaling a significantly improved conditioning of the optimized information matrix due to injection rate design.

Further, the optimized signals were decomposed into their constituent frequencies and the single-sided amplitude spectrum plotted in Figure 5.10. Like in the previous case, the plot shows that the number of non-zero frequency points in the optimized spectrum (16 in this case) was between the bounds necessary for persistent excitation, confirming that the design method yields persistently exciting signals.

To test these optimized signals, simulation was performed comparing parameter estimates from the designed signals with those from unoptimized PRBS. The approach for this validation exercise, based on simulation, is as in Case 1 above. Figure 5.11 shows the unoptimized PRBS used for validation. Figure 5.12 presents the production rates simulated using the optimized and unoptimized injections before and after noise addition.

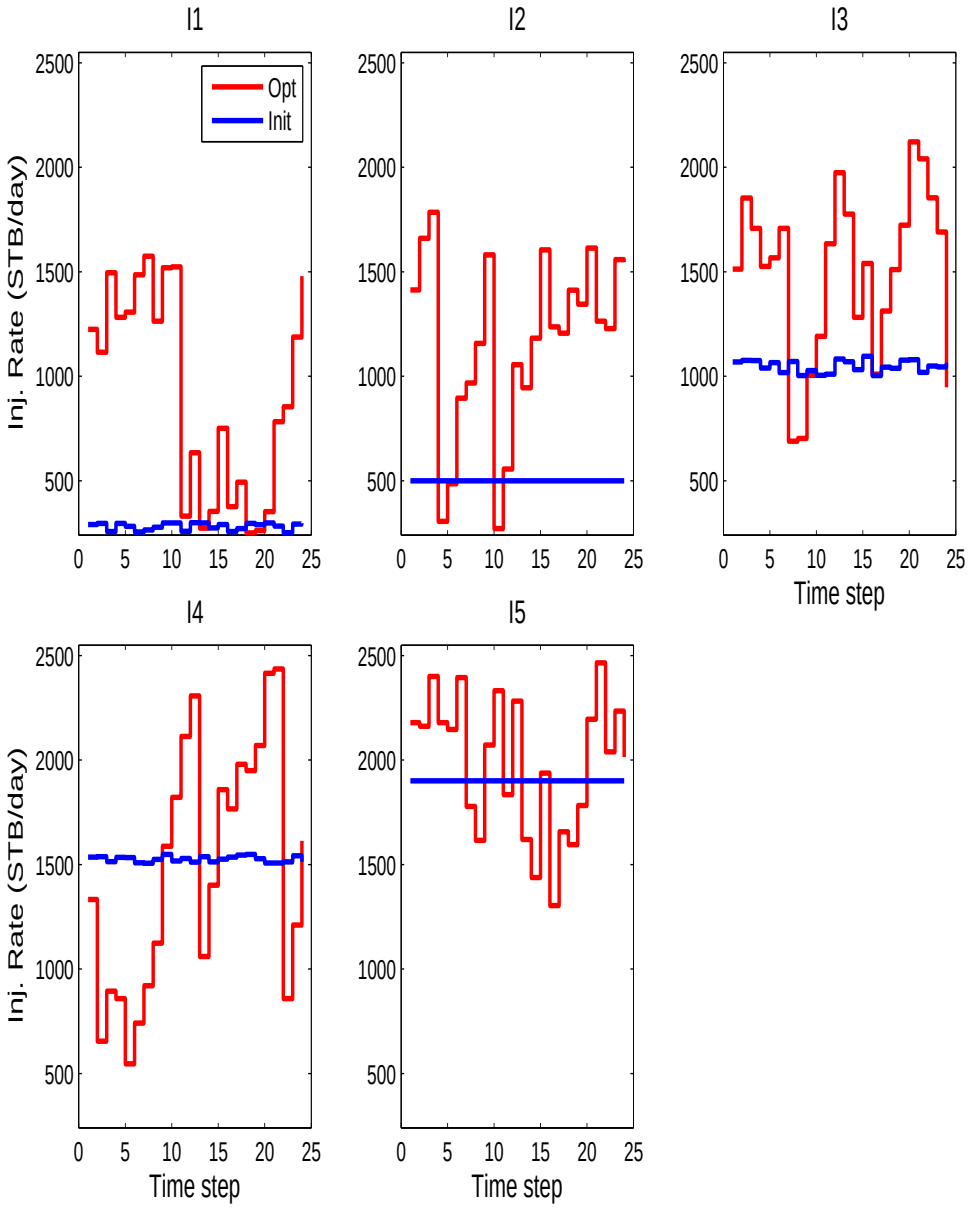

Figure 5.9: Optimized injection rates designed for joint estimation time constant and gains in Case 2

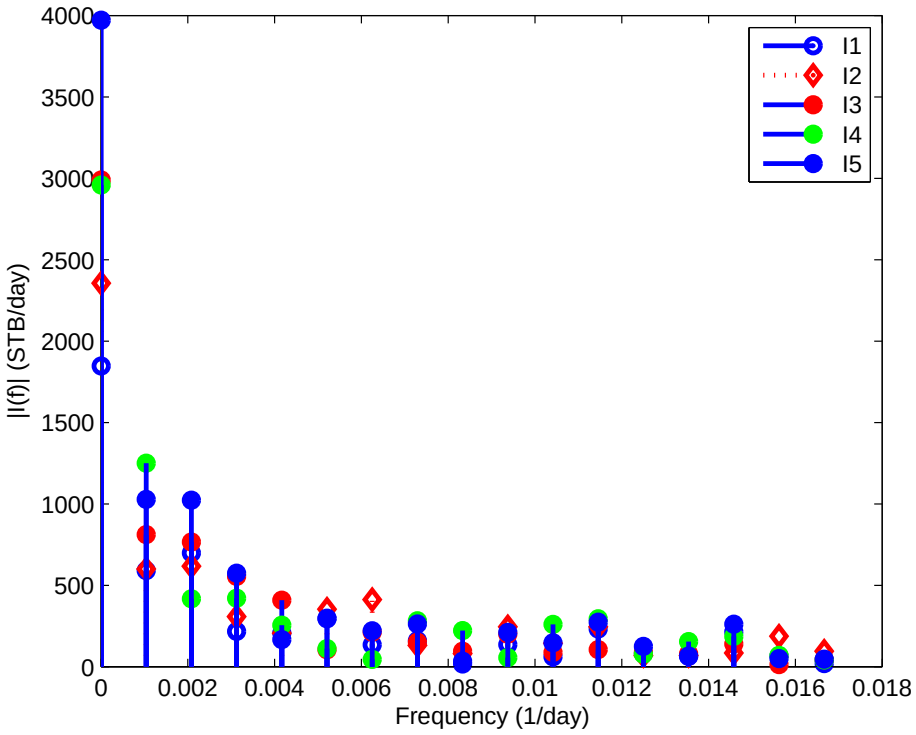

Figure 5.10: One-sided amplitude spectrum of optimized injection profile in Case 2

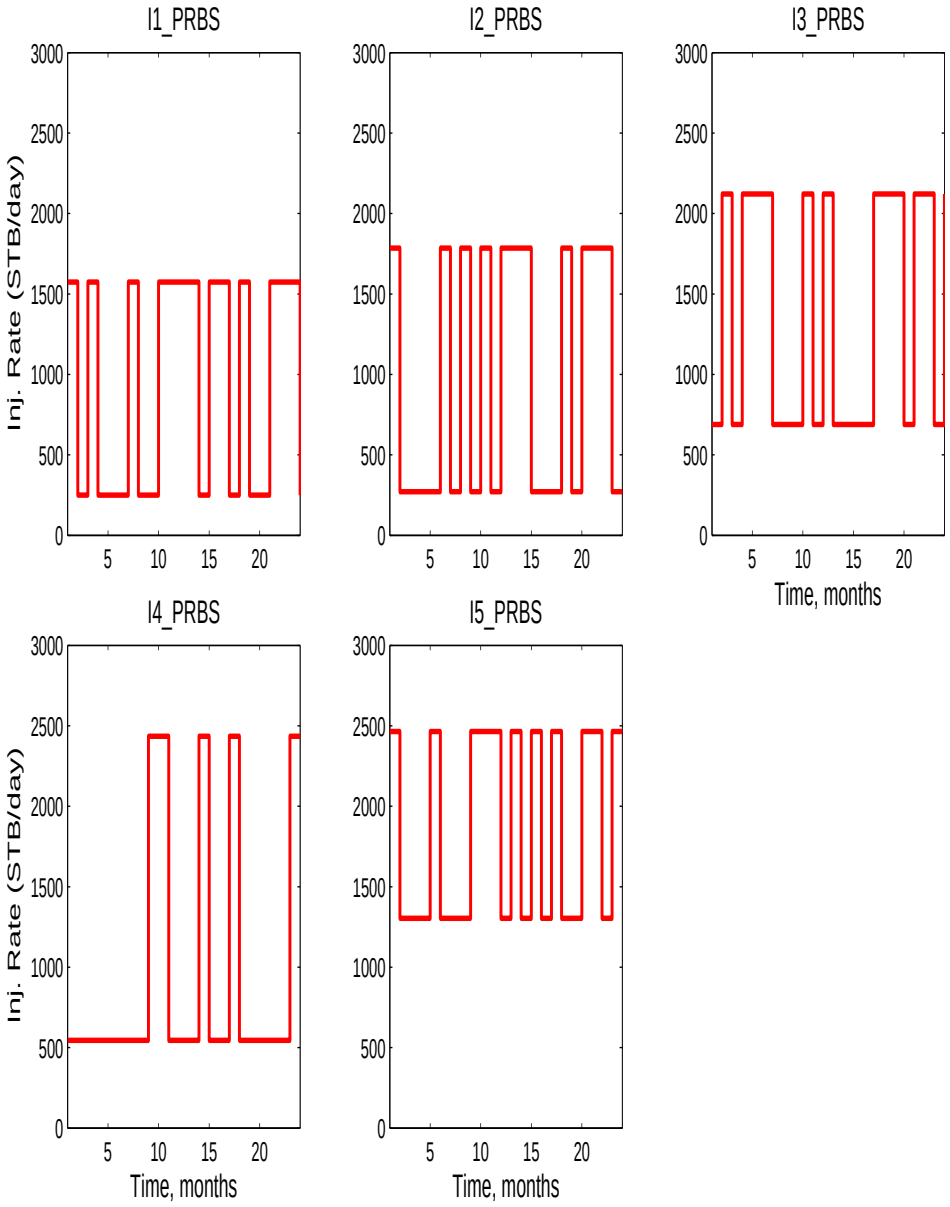

Figure 5.11: Unoptimized PRBS injection rates for Case 2

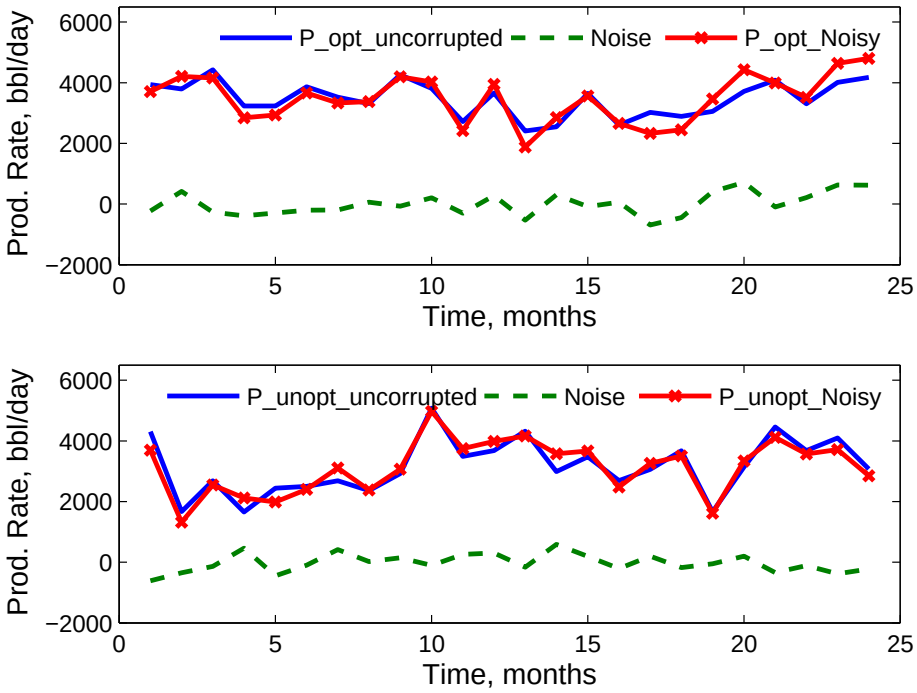

Figure 5.12: Production data simulated using optimized and unoptimized injection rates for Case 2

The results are presented in Table 5.4 and visualized through Figures 5.13 and 5.14. From Figure 5.13, it is apparent that data generated using the optimized signal now yields a slightly inferior gain estimate relative to the unoptimized despite both being corrupted with the same level of noise. However, from Figure 5.14, we also observe a superior parameter time constant estimate for the optimized injection sequence relative to the unoptimized. This is an improvement from the previous case in which the unoptimized PRBS returned better tau estimate.

	f1	f2	f3	f4	f5	τ (days)
Original	0.89	0.56	0.10	0.33	0.68	5.80
Optimized	1	0.76	0.15	0.38	0.44	5.00
Unoptimized	0.87	0.62	0.04	0.44	0.62	11.14

Table 5.4: Comparison of parameter estimates from optimized and unoptimized injection rates in Case 2

To explain this improvement in time constant estimation, the power spectrum of the optimized injection signals from Cases 1 and 2 are compared. Figure 5.15, showing the double-sided relative power spectrum of the optimized signals for Cases 1 and 2, presents this comparison. The figure shows that by when optimizing injection rates for time constant estimation, a greater percentage of signal power migrates to the lower frequency modes. This results in injection rates that remain constant for longer periods, agreeing with findings from [68] that such injection sequences may be required for ideal time constant estimation. This redistribution of signal power, while beneficial for time

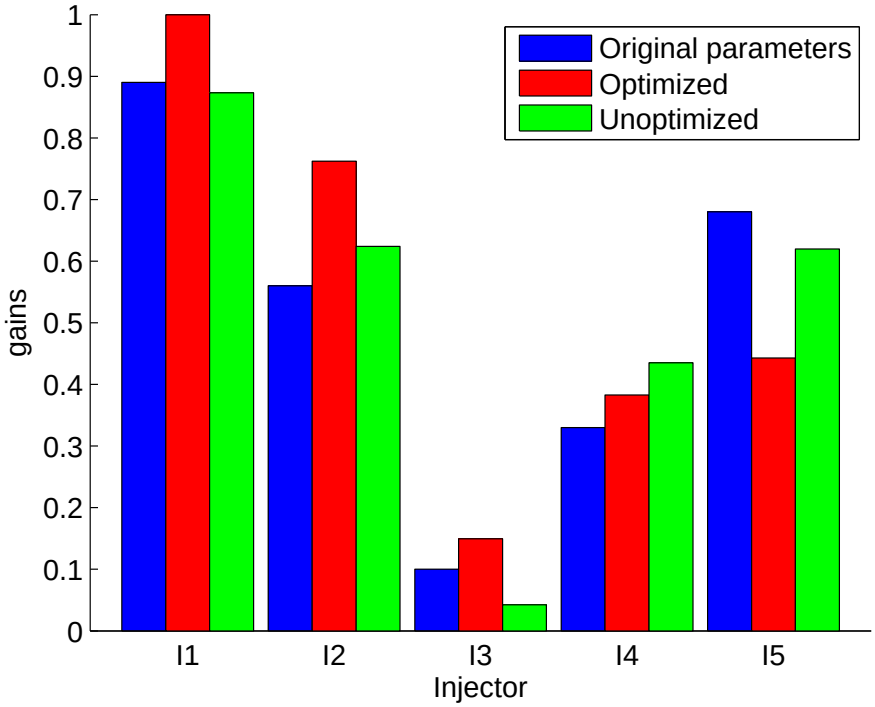

Figure 5.13: Comparison of gains from optimized and unoptimized injection rates in Case 2

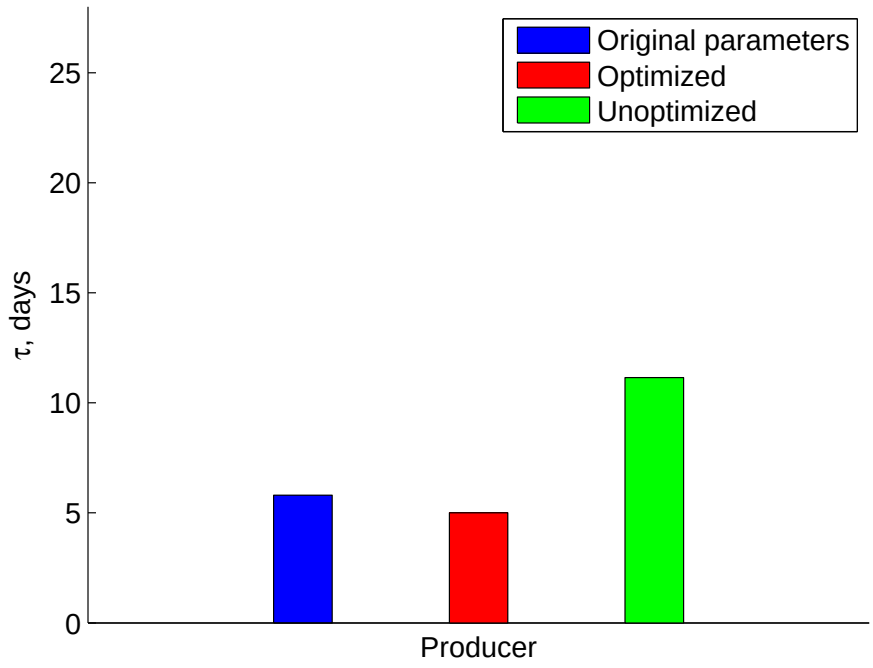

Figure 5.14: Comparison of τ estimates from optimized and unoptimized injection rates in Case 2

constant estimation, leads to less precise gain estimates but may be mitigated through a sequential injection design approach.

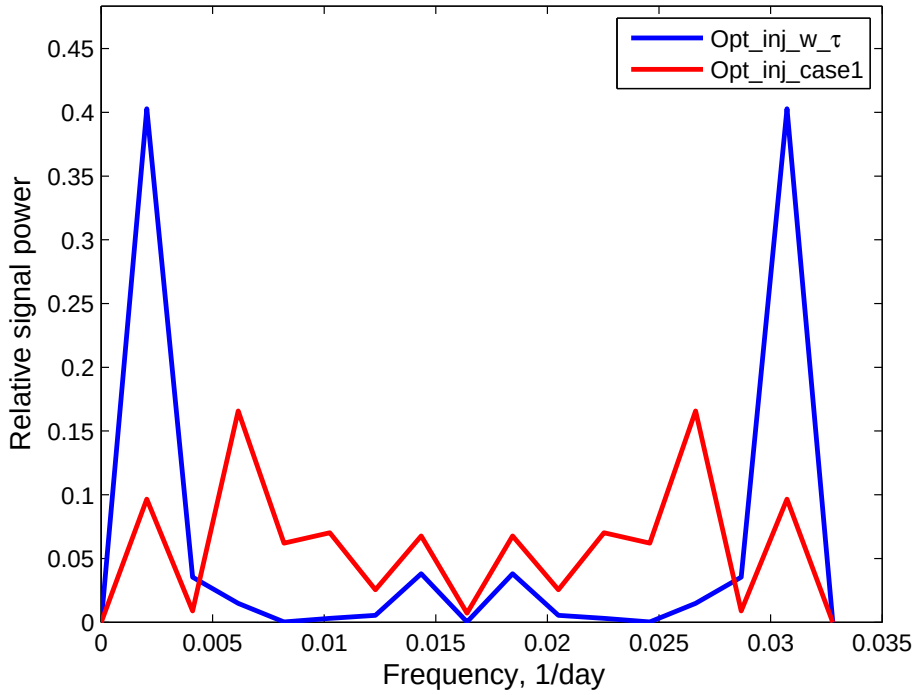

Figure 5.15: Power spectrum analysis for optimized injection signals from Cases 1 and 2

5.3.3 Case 3: Gains and time constant for a multi-producer system

The previous two cases addressed injection design for a single producer system. However, because many field operate with multiple injection and/or production wells, there is a need to implement the injection design method developed here for multi-well systems. In this case, P-optimal design of injection rates is performed for a system of five injectors and four producers. The

well location map for this Case is as shown in Fig. 5.16.

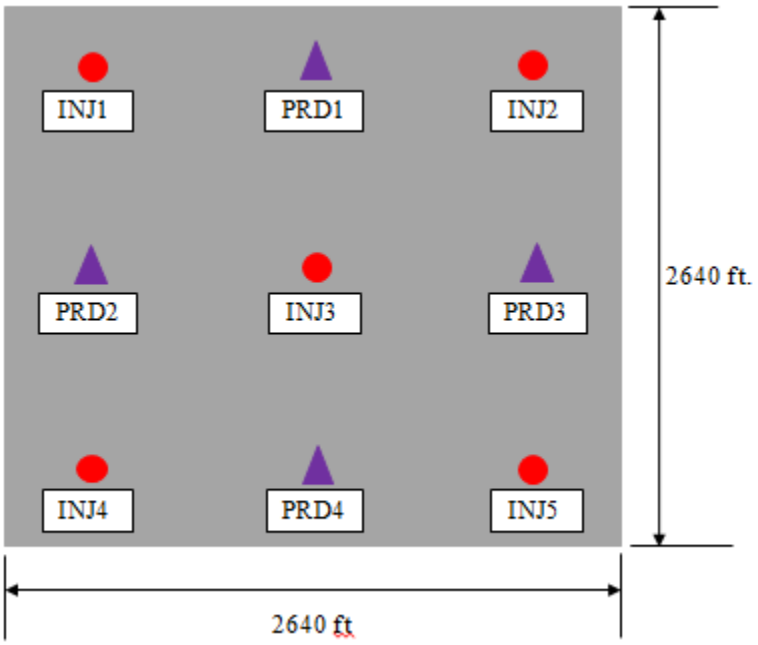

Figure 5.16: Well location map for Case 3

The system-wide FIM was calculated as the sum of the individual FIMs across all producers. The equation for this calculation is presented as Equation 5.5. All other design conditions and constraints were the same as in the preceding cases.

$$M_{sys} = \sum_{j=1}^{n_P} M_j \tag{5.5}$$

Figure 5.17 shows the optimized injection rates obtained for Case 3. Like in the previous case, the optimal inputs are multi-level, indicating an excitation of the different frequency modes of the system. The condition number

of the FIM was found to decrease from 3.75×10^{17} to 5.12×10^{4}, signaling, like in the previous cases, a significant improvement in the conditioning of the optimized information matrix due to injection rate design.

The optimized signals were decomposed into their constituent frequencies and the single-sided amplitude spectrum plotted in Figure 5.18. The plot shows that the number of non-zero frequency points in the optimized spectrum (14 for injector I4 and 16 for the rest) was between the bounds necessary for persistent excitation, confirming that the design method yields persistently exciting signals.

To test these optimized signals, simulation was performed comparing parameter estimates from the designed signals with those from unoptimized PRBS. Figure 5.19 shows the unoptimized PRBS used for validation. The PRBS were generated to have equivalent average power as the corresponding optimized injection signals. Figure 5.20 presents the production rates simulated using the optimized and unoptimized injection rate signals before and after noise addition.

The results are presented in Tables 5.5 - 5.7. Table 5.5 shows the original parameter estimates used in simulating the production rates via CRM. Table 5.6 shows the parameters obtained using data generated with the optimized injection signals while Table 5.7 shows estimates from the unoptimized data. The gain estimates are visualized through Figures 5.21 - 5.24 while Figure 5.25 presents the time constant estimates.

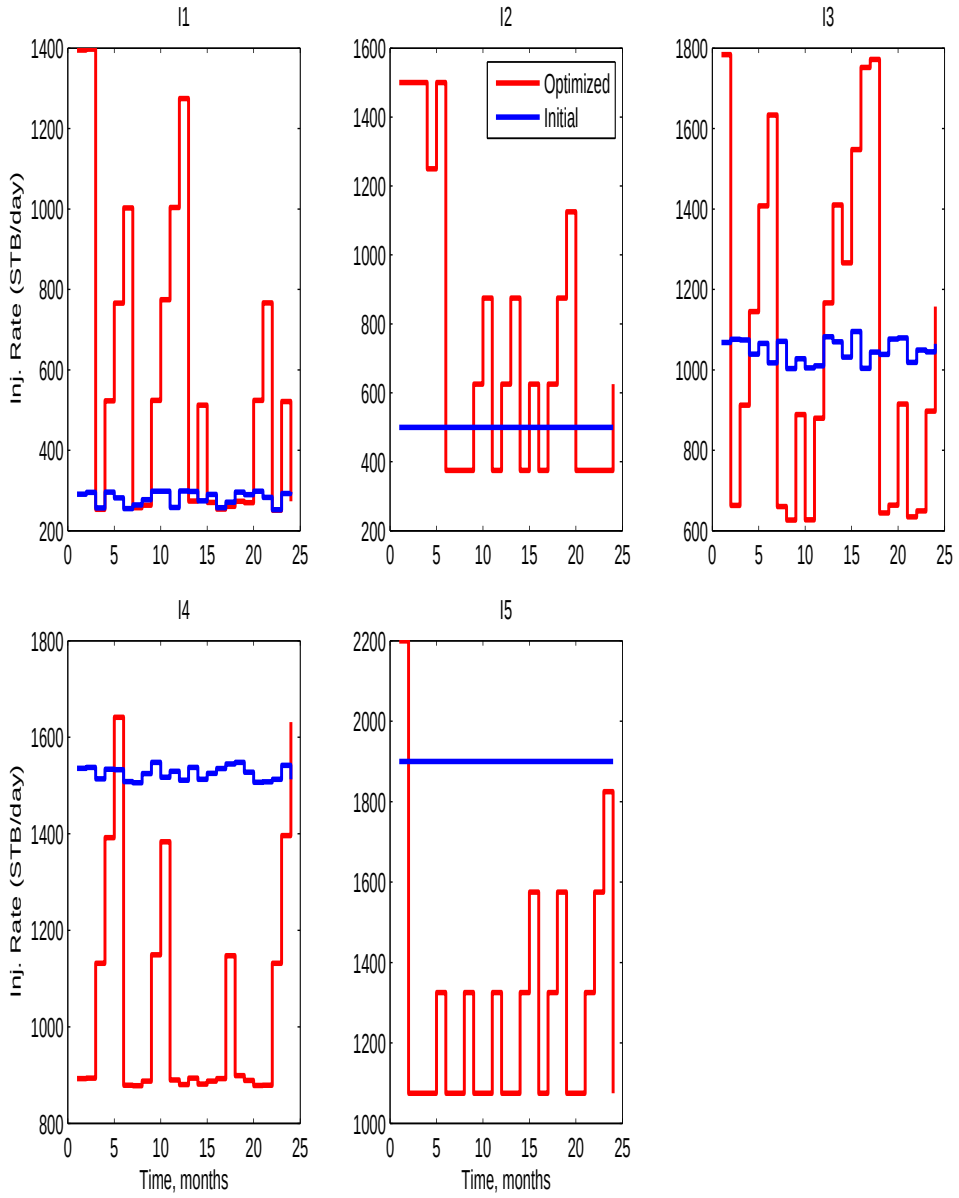

Figure 5.17: Optimized injection rates designed for joint estimation time constant and gains in Case 3

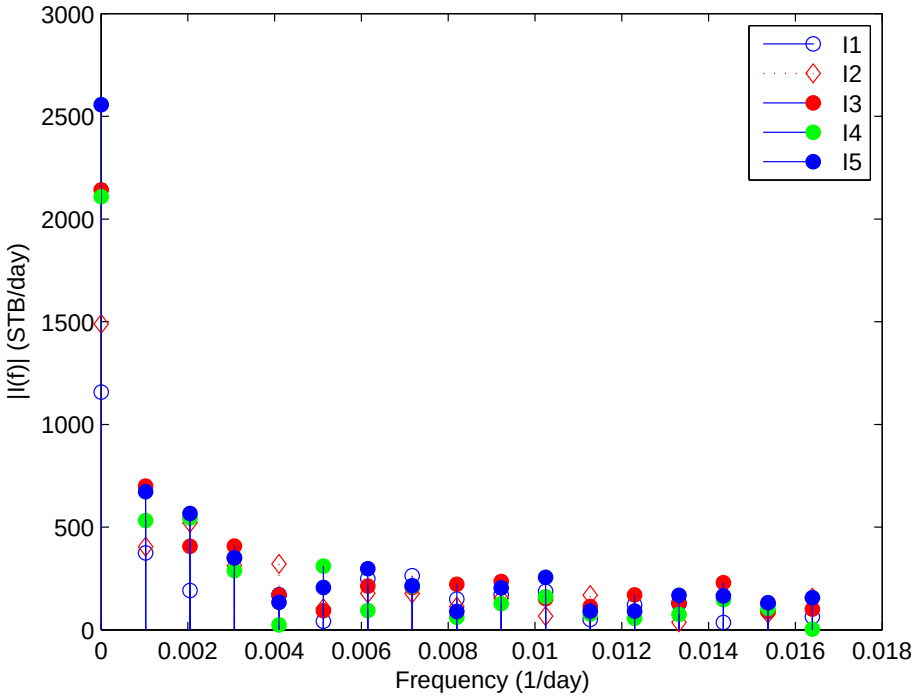

Figure 5.18: One-sided amplitude spectrum of optimized injection profile in Case 3

Producer	f1	f2	f3	f4	f5	τ_j (days)
P1	0.98	0.48	0.08	0.13	0.14	10.24
P2	0.01	0.06	0.02	0.14	0.00	44.30
P3	0.01	0.20	0.00	0.03	0.14	64.04
P4	0.00	0.25	0.90	0.70	0.71	33.09

Table 5.5: Original parameter values for Case 3

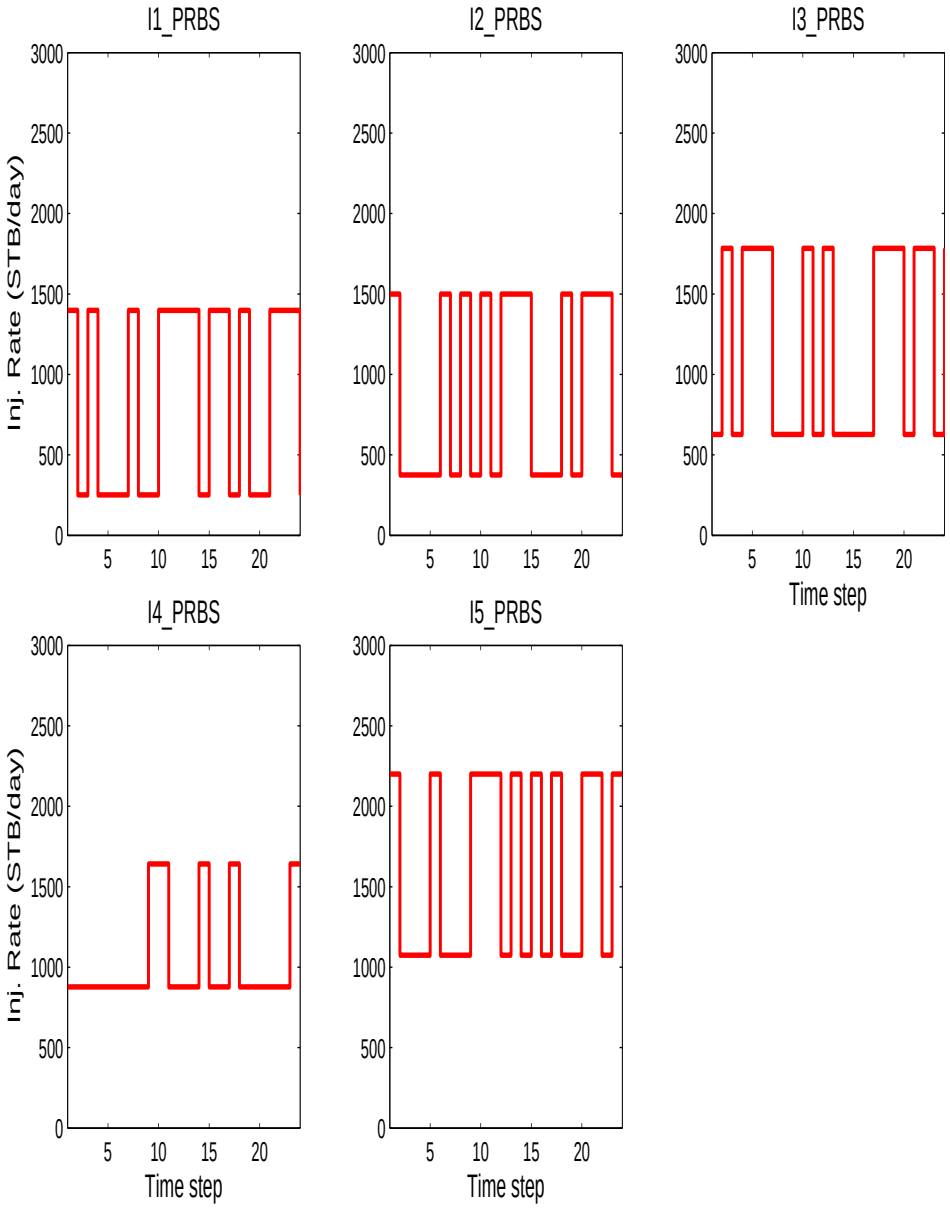

Figure 5.19: Unoptimized PRBS injection rates for Case 3

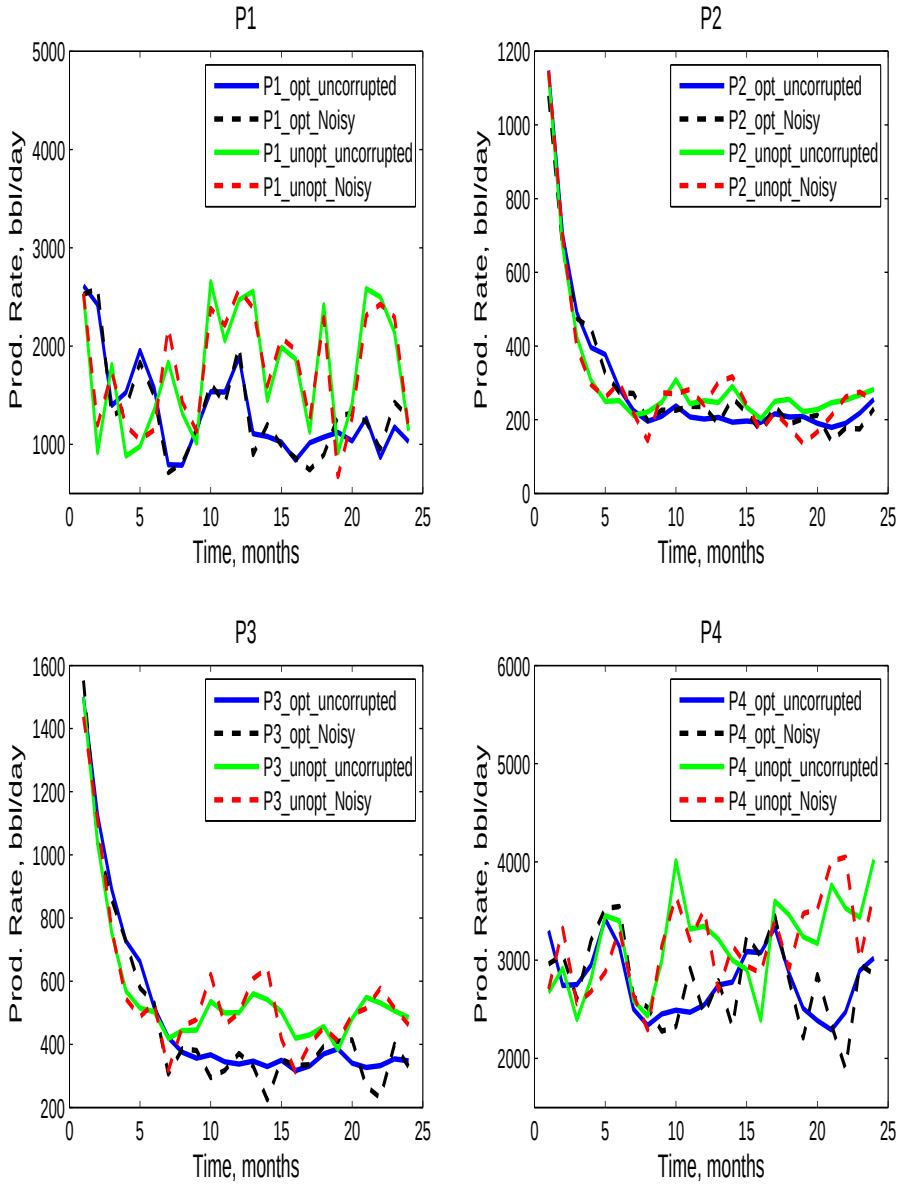

Figure 5.20: Production data simulated using optimized and unoptimized injection rates for Case 3

Producer	f1	f2	f3	f4	f5	τ_j (days)
P1	1.00	0.43	0.00	0.14	0.21	8.42
P2	0.00	0.00	0.00	0.00	0.15	91.85
P3	0.00	0.17	0.00	0.00	0.17	83.64
P4	0.00	0.28	0.86	0.86	0.47	47.41

Table 5.6: Parameter estimates from optimized injection data in Case 3

Producer	f1	f2	f3	f4	f5	τ_j (days)
P1	1.00	0.38	0.03	0.29	0.11	14.51
P2	0.00	0.00	0.00	0.00	0.13	77.36
P3	0.00	0.23	0.00	0.02	0.14	83.64
P4	0.00	0.39	0.97	0.65	0.62	53.83

Table 5.7: Parameter estimates from unoptimized injection data in Case 3

From Figures 5.21 to 5.24, it is apparent that data generated using the optimized signal returns better gains estimates. This is particularly the case for gain values that are significantly high, making the model more sensitive to them. Figure 5.25, we also observe a superior parameter time constant estimate for the optimized injection sequence relative to the unoptimized. This case demonstrates the applicability of the P-optimal design method for multi-producer system.

The observations obtained from this case are consistent with those obtained from analyzing the preceding cases namely that design of injection rates leads to improved history-matching results and more accurate parameter estimates. This demonstrates that the P-optimal input design method can be adequately implemented for a large field where rates for multiple injectors are to be designed simultaneous. Moreover, design for a system of five injectors

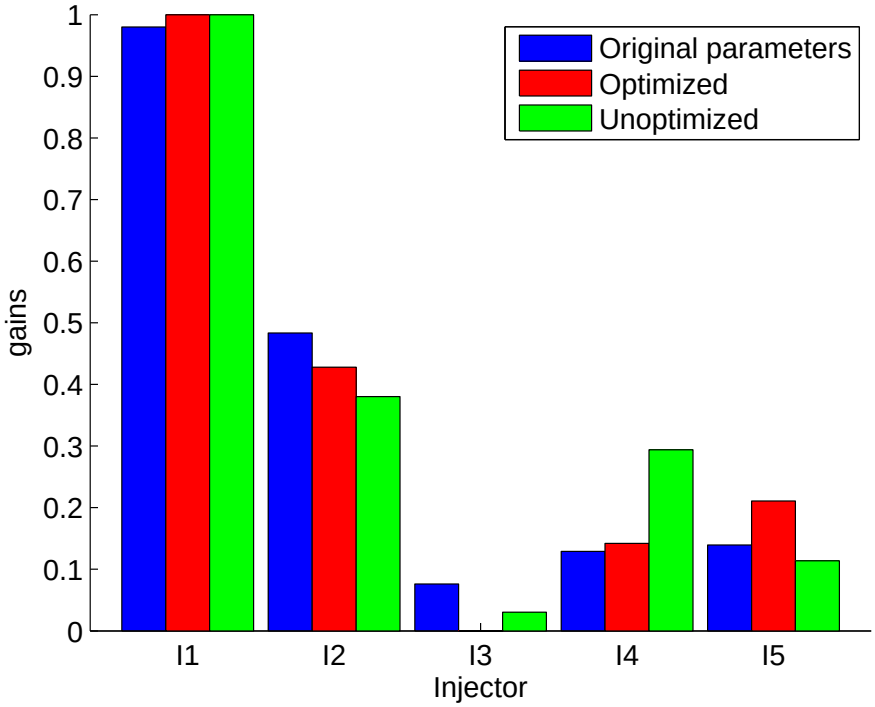

Figure 5.21: Comparison of gains for producer P1 from optimized and unoptimized injection rates in Case 3

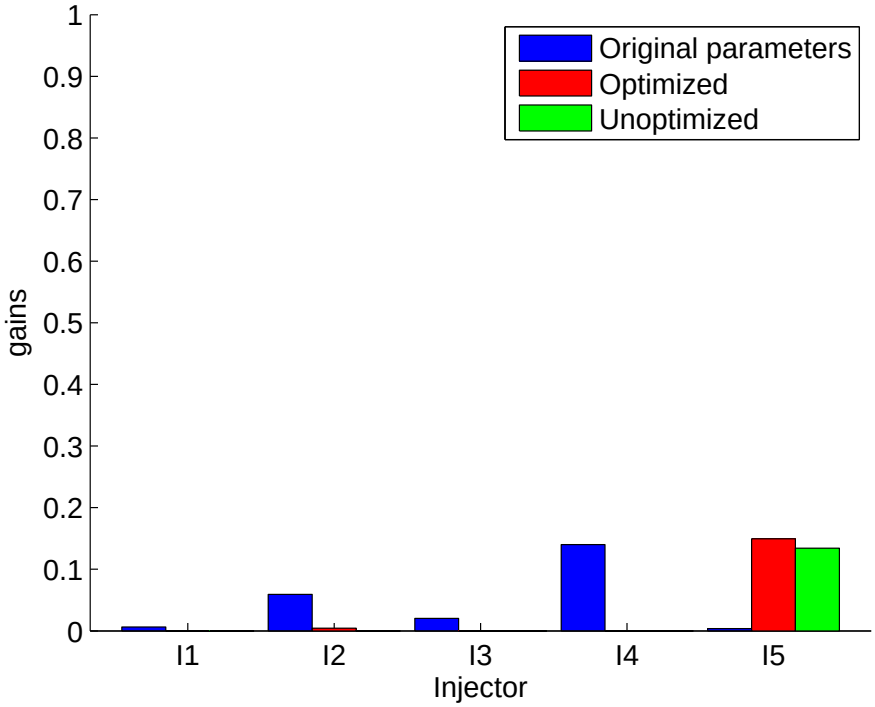

Figure 5.22: Comparison of gains for producer P2 from optimized and unoptimized injection rates in Case 3

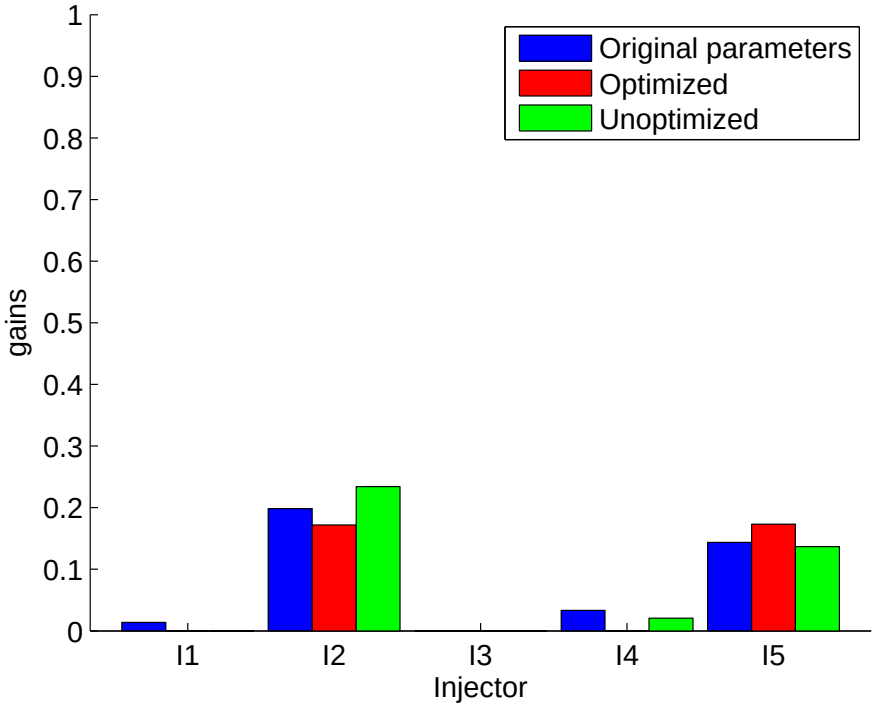

Figure 5.23: Comparison of gains for producer P3 from optimized and unoptimized injection rates in Case 3

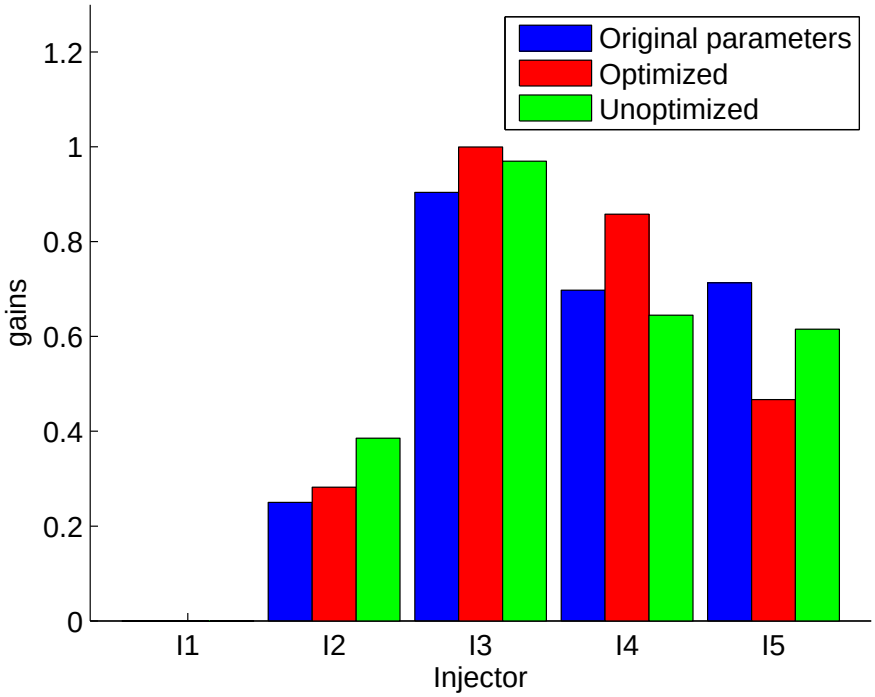

Figure 5.24: Comparison of gains for producer P4 from optimized and unoptimized injection rates in Case 3

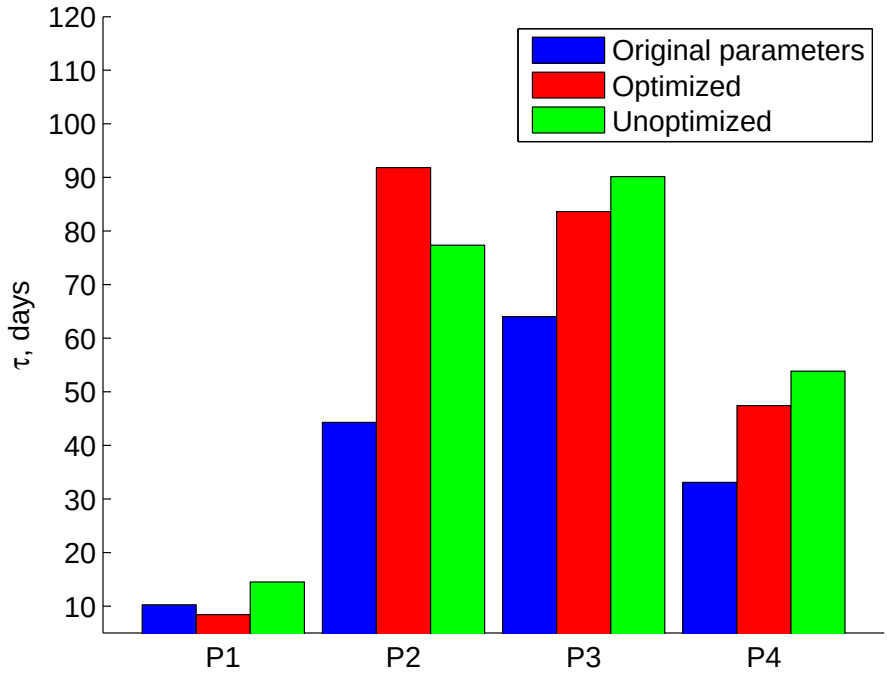

Figure 5.25: Comparison of τ estimates from optimized and unoptimized injection rates in Case 3

and four producers was performed in less than a minute using MATLAB® on a 4 RAM, Intel $i5-2430$M machine, indicating this approach is applicable with reasonable computational effort for injection rate design in large systems.

5.4 Conclusions

In this work, injection rates were optimized for CRM parameter estimation. A time domain approach was adopted and the P-optimal criterion was used. Our optimization algorithm proved robust, reducing the condition number from 1.32×10^{17} to 50 (design for gains only in a one producer system), from 1.32×10^{17} to 2.11×10^{4} (design for all parameters in a one producer system), and from 1.32×10^{17} to 5.12×10^{4} (design for all parameters 5-producer, 4-injector system). Also, the optimized inputs showed high levels of richness. Their single-sided amplitude spectrum showed appropriate numbers of distinct frequency components, which is a necessary if the signals are to be persistently exciting.

Further, the designed inputs were tested by comparing with unoptimized PRBS. Results demonstrate that even at the same levels of noise, optimized signals generally return more accurate parameter estimates relative to the unoptimized. High R^2 values were consistently obtained for the optimized signal in all cases. However, in cases where design is conducted for both gains and time constants, redistribution of signal power to lower frequency modes may cause better time constant estimates but worse gain estimates.

It was observed that the sensitivity of the time constant depends on

parameter values. This necessitates a good knowledge of the parameters to be designed for as the design method is only as good as the parameter estimates used. To overcome the problem of unknown/unavailable initial parameter estimates, a sequential implementation of the P-optimal design method demonstrated in this work is recommended. Here, PRBS excitation can be used to perturb the system to obtain crude parameter estimates that would then be refined using the design method presented in this dissertation.

Chapter 6

Development of a Thermal CRM Variant for Hot Waterflooding

6.1 Introduction

6.1.1 Motivation for Thermal CRM Development

The CRM is a reduced-order, input-output model that characterizes reservoirs using production/injection and BHP fluctuations. The model was primarily developed for waterflooding (secondary recovery) and has since been successfully applied to other primary and EOR process. The CRM is relatively fast, requires no geological data and is applicable to reservoirs with significant number of wells. These factors make developing such a model attractive for characterization and optimization of reservoirs under thermal stimulation.

This chapter will focus on extending the applicability of the capacitance resistance modeling method to thermal recovery processes. Hot waterflooding in particular is considered in this work. The focus on hot waterflooding is for two reasons:

- First, the simplicity of the hot waterflooding process as well as its similarity to cold waterflooding (relative to other processes in the thermal stimulation family) makes an extension of the CRM approach to hot

waterfloods a logical natural step. Successful extension of the CRM technology to hot waterflooding would provide solid basis to tackle more complex thermal stimulation processes such as steamflooding, SAGD, and in-situ combustion.

- Second, CRM's speed and low computational cost make it an attractive candidate for modeling hot waterflooding processes. Because characterization of hot waterflooding, like for many thermal processes, is oftentimes expensive and time consuming, a thermal CRM could provide a cheaper and faster alternative/complement relative to numerical thermal simulators.

Extending the current CRM to hot waterflooding will require the following four key steps:

- **Relaxation of the isothermal assumption in the current CRM**: As is, the CRM is incapable of capturing the temperature dynamics that occur in a hot waterflooding process. The isothermal assumption invoked in the development of the original CRM limits the ability of the model parameters to evolve as the reservoir is heated. Thus, the first objective in this work is to relax the isothermal assumption in the original CRM. This would necessitate the development of an energy balance model that will track the temperature changes in the reservoir as hot fluid is injected.

- **Evolution of model parameters using temperature dynamics**: A major assumption in this work is that viscosity reduction is the pri-

mary driver of oil mobilization and flow in the reservoir. Because CRM time constants depend on viscosity, the second objective is to devise effective means of evolving viscosity as a function of temperature and subsequently time constants as a function of viscosity.

- **Model validation**: To demonstrate the workability of the thermal CRM, the model is validated via numerical simulation. Simulation for a one dimensional reservoir under hot waterflooding is done using STARS thermal simulation software of the CMG. The simulation results are first compared to an analytical treatment of hot waterflooding to reconcile both. The analytical treatment involves a construction of the Walsh plot based on the Fractional Flow Theory. Subsequently, simulations is used to validate the developed thermal CRM.

- **Sensitivity analysis**: Beyond its use for reservoir characterization, the thermal CRM is to be used for production forecasting and optimization. Thus, the reliability of model predictions is of significant importance. A sensitivity of the model parameters to different reservoir/fluid conditions would elucidate the impact of these input parameters on the thermal CRM performance. Insights based on the results would provide guidance on the applicability of thermal CRM under certain (different) scenarios.

6.1.2 Chapter Layout

The remainder of this chapter is organized as follows: First, an analytical treatment of hot waterflooding process is presented. The results provides

a basis for quality assurance of simulation results from a commercial simulator. These simulation results will be used in validating the thermal CRM. Subsequently, development of the thermally coupled CRM (TCCRM) and the linearized coupled CRM (LCCRM) is presented, with detailed derivation of the necessary model equations. Model validation is conducted for different simulated cases to demonstrate model applicability to different reservoir conditions/configurations. The chapter concludes with a summary of key findings.

6.2 Analytical Treatment of Hot Waterflooding

6.2.1 Approach

This section considers an analytical treatment of hot waterflooding to serve as benchmark for the validation of subsequent simulations. The fractional flow approach is followed as described in [32]. Here, parameters a and b are calculated from rock and fluid properties used in [77]. These parameters are used to make the plots as shown below. Here, parameters a and b are plotted (b,a) on the fractional flow curve in contrast to (a,b) as seen in [32]. This switch comes from numerous unsuccessful attempts in to plot as (a,b). This view is also supported by Equation $11.3 - 15$ in the same book [32].

Figure 6.2 shows the effluent fractional flow of water as a function of dimensionless time. The plot is obtained by applying the fractional flow theory to the hot and cold water fractional flow curves as shown in Figure 6.1. This method has been extensively treated by many authors for hot waterflooding [52], and for other enhanced oil recovery techniques [66], [76], [6]. Figure 6.2

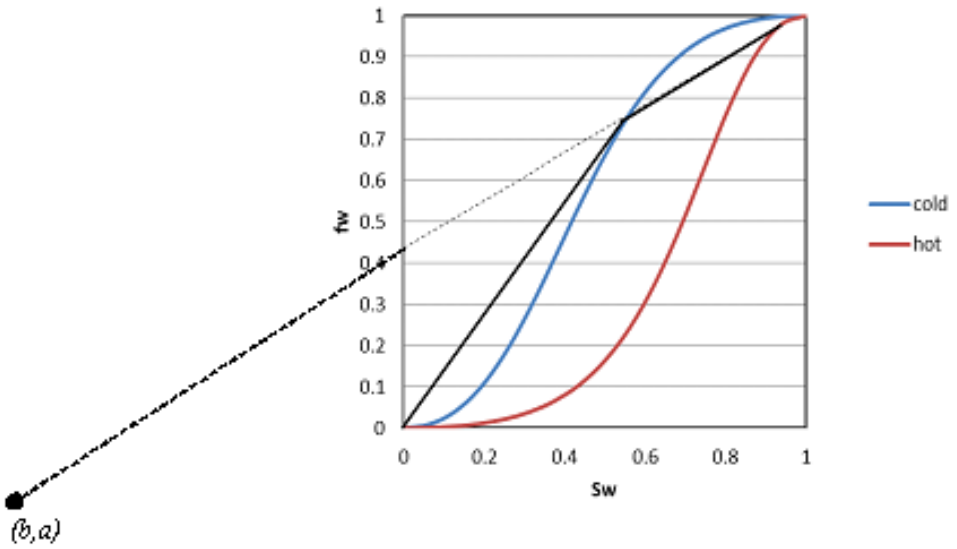

Figure 6.1: Graphical construction of hot waterflood based on relative permeability data and fractional flow calculations

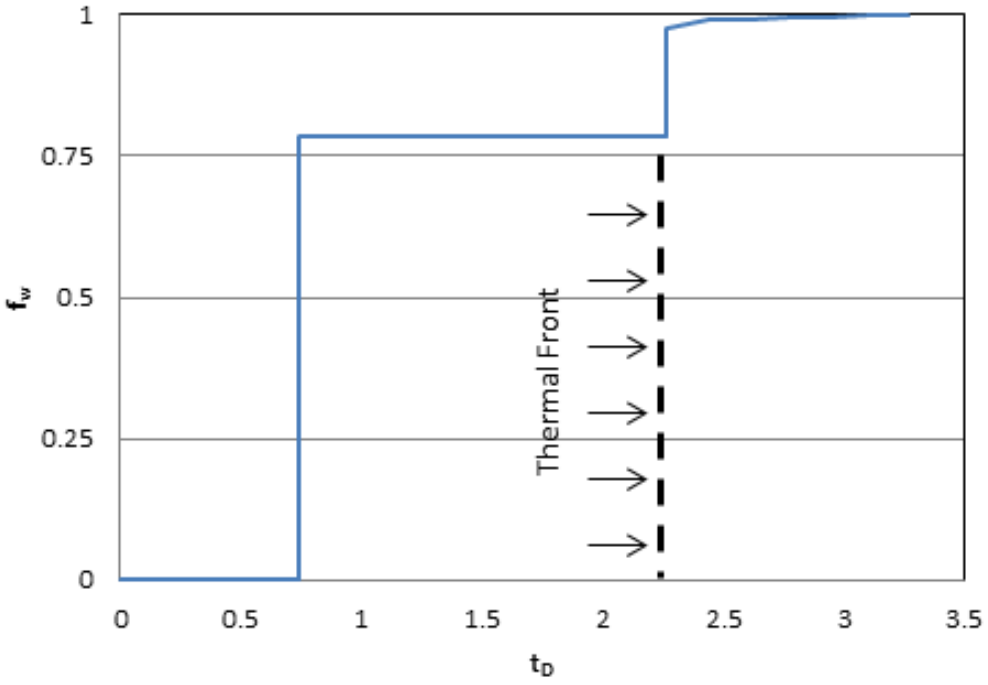

Figure 6.2: Effluent water fractional flow vs. dimensionless time obtained via analytical construction

is obtained following the same simplifying assumptions as presented in [52].

As expected, the plot shows two shocks. The first shock arriving at 0.73 dimensionless time (or pore volume of control volume around producer (PV) injected) indicates the arrival of the cold water front, while the later shock arriving at 2.27 PV indicates the arrival of the hot water (or thermal) front. The presence of two shocks is as a consequence three-component in a reservoir and was equally observed in the analytical treatment of hot waterflooding using the fractional flow theory by [32].

The following subsection presents a comparison between the analytical treatment presented here and numerical simulation of a hot waterflood using the same input data. The goal is to demonstrate agreement between the two approaches agree and thus establish simulation as an appropriate way to validate the thermal CRM.

6.2.2 Comparison of CMG Simulation with Analytical Treatment of Hot Waterflooding

6.2.2.1 Case 1: For μ_{oil} = 5 cp at reservoir conditions

Following the analytical solution of the hot waterflood presented earlier, simulation runs were performed in CMG STARS software for a 1D reservoir undergoing hot waterflooding. Figure 6.3 presents the dimensions and the well placement for this reservoir. The same assumptions as the ones used for the analytical development, particularly fluid incompressibility and no heat conduction, were used here. The rock and fluid properties used in the simulation

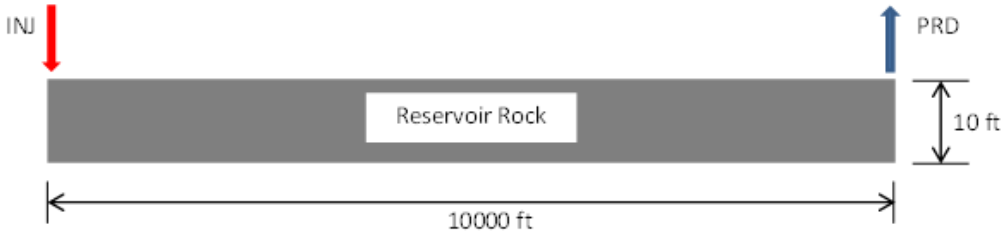

Figure 6.3: 1D Reservoir Dimensions and Well Configurations

are summarized in Tables 6.1 and 6.2.

Table 6.2 data is used to calculate the oil/water relative permeability curve as shown in Figure 6.4.

From the simulation results, a plot of water fractional flow (f_w) against dimensionless time (t_D) was made and compared to the analytically derived analog. The graphical comparison is shown through Figures 6.5 and 6.6:

Figure 6.6 show a good match between the analytical solution and simulation results. Specifically, we see that both approaches show two breakthroughs of similar magnitudes occurring at identical times. The first breakthrough, occurring as a shock at 0.73 PV (i.e., pore volumes of water injected), is the cold water breakthrough. At this point, the water cut of the producer synchronously becomes nonzero for the first time both in the simulation as well as in the analytical solution.

The second shock indicates the arrival of the thermal front and occurs at 2.24 PV. While the arrival of the hot water front is a sharp shock in the analytical solution, the corresponding shock in the simulation is diffuse. To confirm that the diffuse nature of the second shock is not caused by its small

SIMULATION DATA	
Oil viscosity	5 cp @ T=100 °F
	0.5 cp @ T=200 °F
Oil density	46.4 lb/ft^3
Oil specific heat capacity	0.5 btu/lb·°F
Water viscosity	0.5 cp
Water density	62.7 lb/ft^3
Water specific heat capacity	1 btu/lb·°F
Fluid conductivities	0
Compressibility	1×10^{-6} psi^{-1}
Volumetric heat capacity	35 btu/ft^3·°F
Grid dimensions	1000×1×1
Block size (in i,j,k directions)	10 ft
Permeability (in i,j,k directions)	1000 md
Porosity	0.3
Initial reservoir temperature	100 °F
Initial pressure	100 psi
Initial oil saturation	1
Initial water saturation	0
Initial gas saturation	0
Simulation time period	1/1/2000 - 1/1/2020
Injectant	HOT WATER
Injection flow rate	25 bbl/day
Steam quality	0
Injection temperature	200°F
Injection start time	1/1/2001
Injector gridblock location	1,1,1
Producer gridblock location	1000,1,1
Producer BHP	100 psi

Table 6.1: Simulation data for 1D hot waterflooding reservoir

Parameter	**Value**
SWCON - Endpoint Saturation: Connate Water	0
SWCRIT - Endpoint Saturation: Critical Water	0
SOIRW - Endpoint Saturation: Irreducible Oil for Water-Oil Table	0
SORW - Endpoint Saturation: Residual Oil for Water-Oil Table	0
SOIRG - Endpoint Saturation: Irreducible Oil for Gas-Liquid Table	0
SORG - Endpoint Saturation: Residual Oil for Gas-Liquid Table	0
SGCON - Endpoint Saturation: Connate Gas	1×10^{-3}
SGCRIT - Endpoint Saturation: Critical Gas	1×10^{-3}
KROCW - k_{ro} at Connate Water	1
KRWIRO - k_{rw} at Irreducible Oil	0.3
KRGCL - k_{rg} at Connate Liquid	1×10^{-3}
Exponent for calculating k_{rw} from KRWIRO	1.5
Exponent for calculating k_{row} from KROCW	3.5

Table 6.2: Oil/Water Relative Permeability Parameters

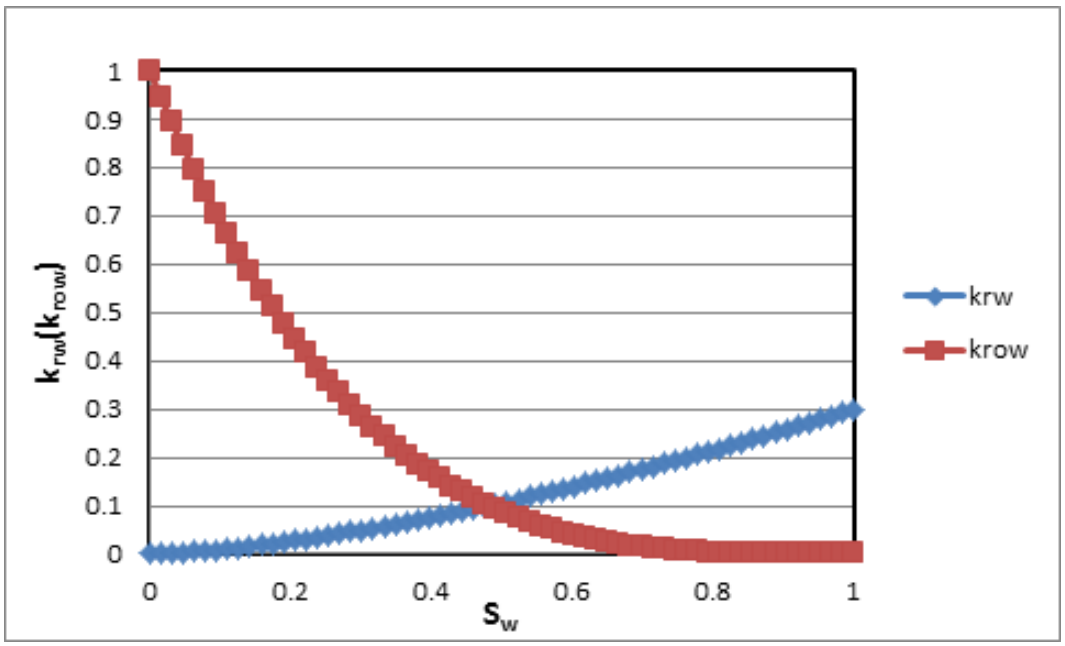

Figure 6.4: Oil/water relative permeability curves as calculated using Table 6.2 values

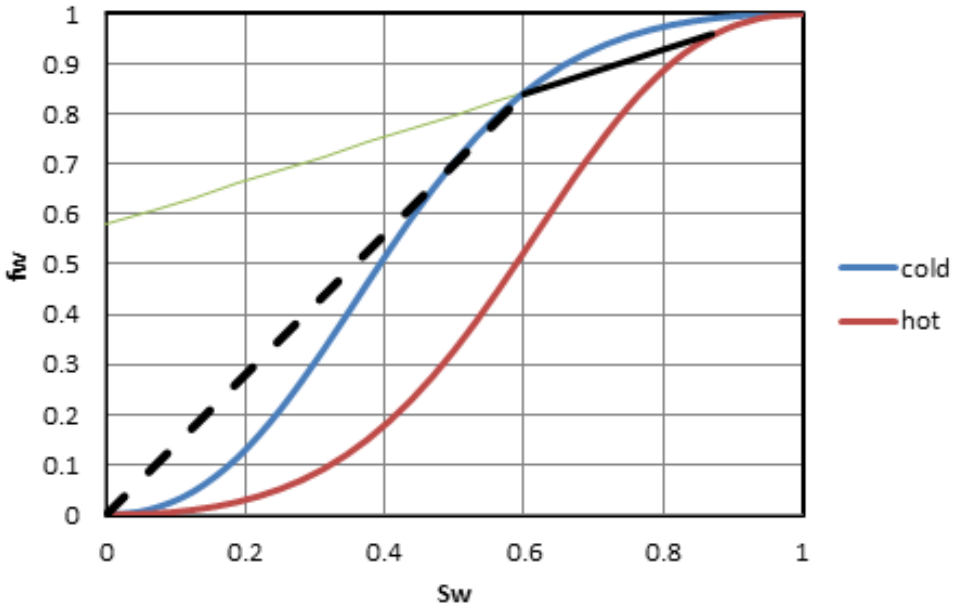

Figure 6.5: Effluent fractional flow curve based on simulation inputs for analytical calculation of hot waterflood

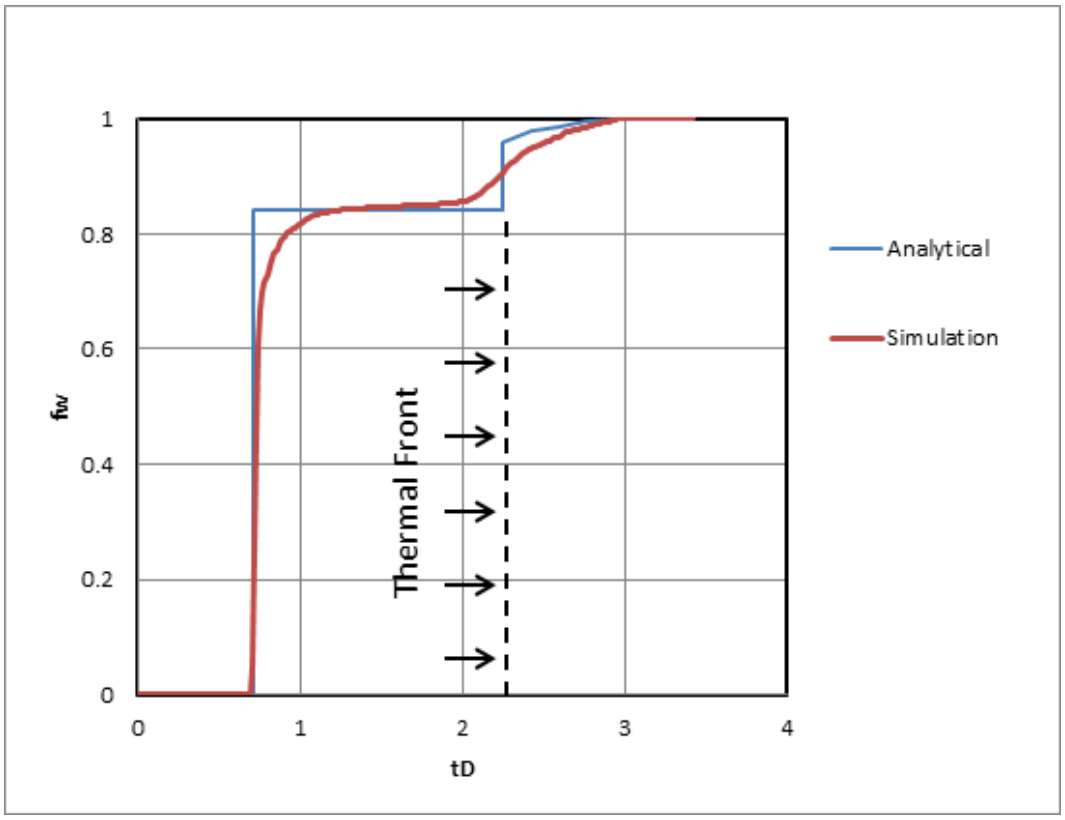

Figure 6.6: Graphical comparison of analytical solution to CMG simulation result

magnitude, another simulation run (Scenario 2) is performed and presented in the next subsection.

6.2.2.2 Case 1: For μ_{oil} = 28.86 cp at reservoir conditions

In this scenario, oil viscosity was increased over five-fold and key thermal properties adjusted to provide more thermal contrast between rock and fluid. These adjustment are intended to minimize the magnitude of the cold water shock and thus potentially yield a larger second shock. The adjusted simulation parameters are presented in Table 6.3. All other parameters retain the same value as in the first scenario.

ADJUSTED SIMULATION DATA FOR SCENARIO 2	
Oil viscosity	28.86 cp @ T=100°F
	0.49 cp @ T=200°F
Water specific heat capacity	6.66 btu/lb·°F
Volumetric heat capacity	120 btu/ft^3·°F

Table 6.3: Adjusted simulation data for Case 2

As in the first scenario, analytical construction for the hot waterflood using the adjusted simulation inputs is first perform. Subsequently, the data is applied to the CMG STARS simulator. The simulation output of oil/water production rate is used to calculate the effluent fractional flow curve and graphically compared to analytical solution. The analytical construction as well as the graphical comparison is presented in Figures 6.7 and 6.8:

Figure 6.8 shows a better match between the analytical and simulation

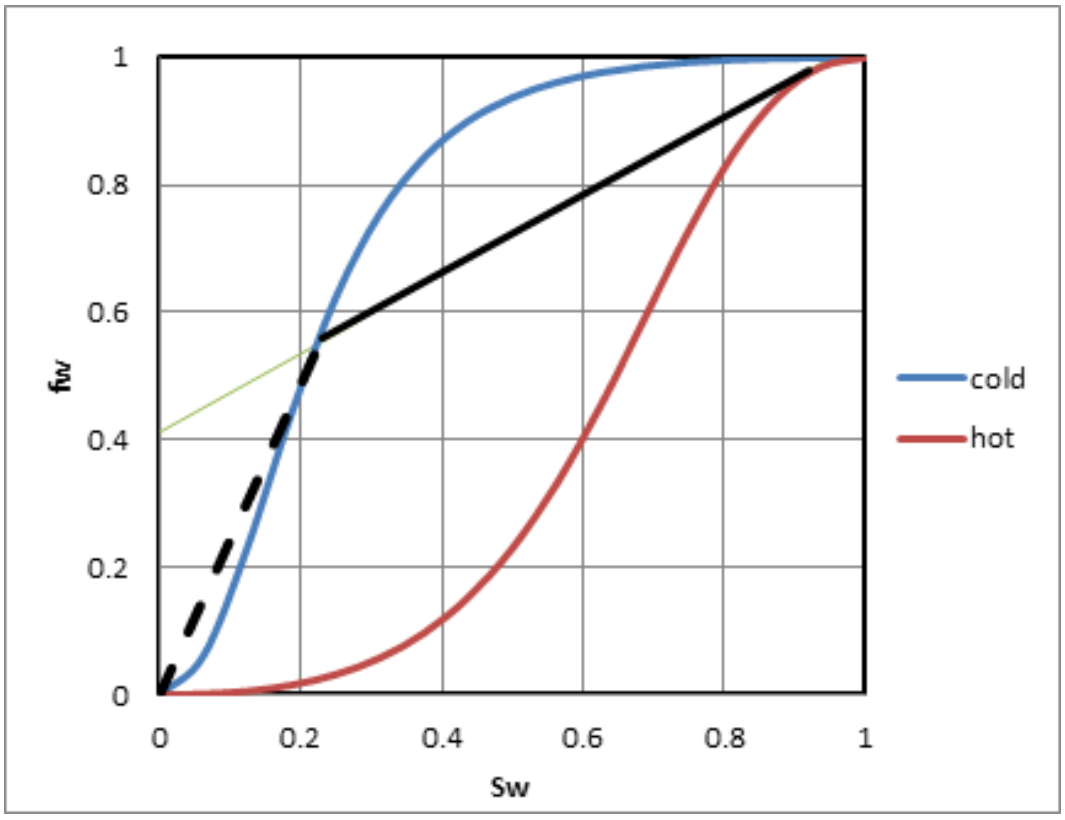

Figure 6.7: Analytical construction of hot waterflood using adjusted simulation parameters (Scenario 2)

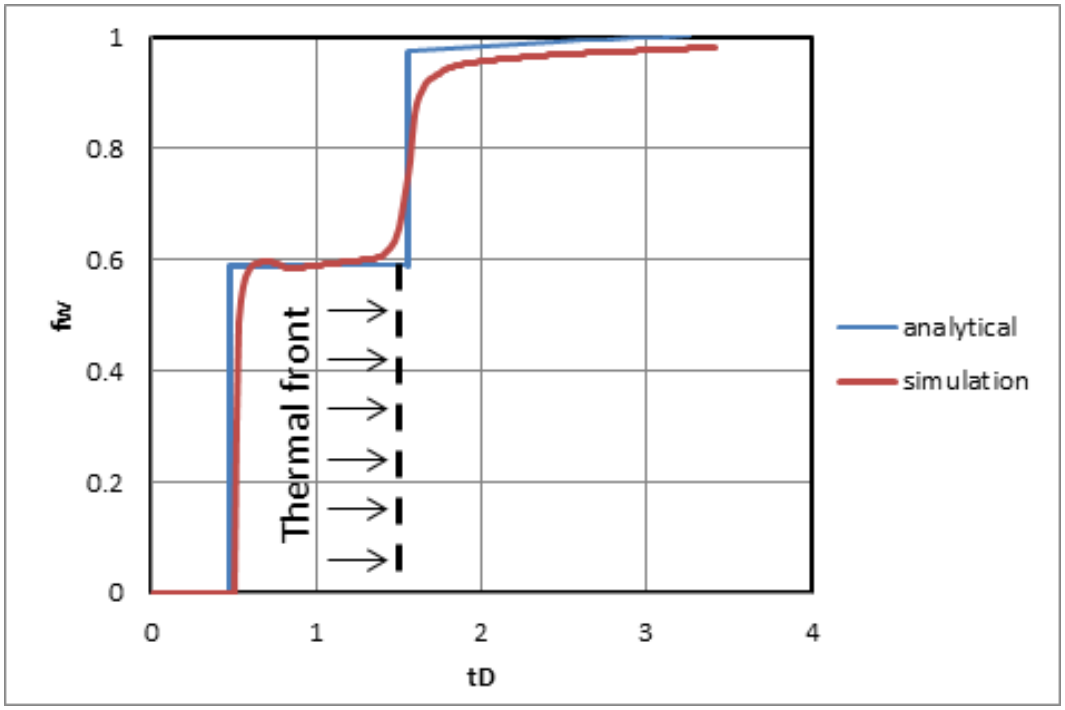

Figure 6.8: Graphical comparison of analytical solution and simulation for Scenario 2

solutions. Here, we see that both the cold and hot water arrival occur as sharper shocks relative to the first scenario. This confirms the equivalence of the analytical and simulation approaches and also provides insights into the impacts of parameters like fluid/rock heat capacities as well as fluid viscosities on breakthrough time in an incompressible hot waterflood. The slight smoothness in the edges of simulation results is mainly because of the inbuilt numerical stability routines embedded in CMG STARS software.

6.3 Development of the CRM for Hot Waterflooding

For the producer-based CRM (CRMP), the model is characterized by two model parameters: the gain or interwell connectivity (f_{ij}) and the time constant (τ_j). This variant of the CRM is shown in Equation 6.1.

$$q_j^k = q_j^{k-1} e^{\frac{-\Delta t}{\tau_j}} + (1 - e^{\frac{-\Delta t}{\tau_j}}) \sum_{i=1}^{N_{inj}} f_{ij} I_i^k \tag{6.1}$$

where q_j^k is the production rate from producer j at time step k, $q_j^k$is production rate from producer j at time step *k-1*, $\Delta t$is the time interval between time steps k and *k-1*, $\tau_j$is the time constant of producer j, f_{ij} is the gain or interwell connectivity between injector i and producer j, and I_i^k is the injection rate at injector i at time step k.

The gains describe the level of hydraulic interconnectedness or communication between an injector-producer well pair at steady state. Because reservoir heating does not significantly interfere with steady-state flow patterns

in a homogeneous reservoir, the physical meaning of gains remains unchanged even for a hot waterflood, barring any significant changes that may impact the overall reservoir characteristics and/or configuration such as well additions or shut-ins.

The CRM time constant for producer j is given by Equation 6.2:

$$\tau_j = \frac{c_t V_P}{J_j} \tag{6.2}$$

where c_t is the total compressibility, V_P is the producer pore volume, J_j is producer j's productivity index.

Unlike the gains, the time constants has been shown to vary significantly even for a cold water flood when saturation changes are significant [9]. In an immature cold waterflood, this evolution in time constant values arises when the productivity index, being a function of saturation, changes with time. The productivity index for a producer j is as shown in Equation 6.3. This equation, proposed by Peaceman [51], is valid when skin is ignored.

$$J_j = \frac{2\pi hk}{\frac{1}{2} ln \left[\frac{4A}{\gamma C_A r_w^2}\right]} \left(\frac{k_{ro}}{\mu_o} + \frac{k_{rw}}{\mu_w}\right) \tag{6.3}$$

where h is the thickness of the control volume, k is absolute permeability, A is the drainage area, $C_A$is shape factor, γ is Euler's coefficient, r_w is wellbore radius, $k_{ro}$and k_{rw} are oil and water relative permeabilities at time t respectively, μ_o and μ_w are oil and water viscosities at time t respectively.

Unlike for a producer in a mature waterflood, the productivity index for a hot waterflooded producer is not constant. The saturation changes cause evolution in the relative permeability values. Additionally, viscosity dynamics caused by reservoir heating, means the productivity index is also a function of temperature. Consequently, the time constant, which occurs as a constant in the original CRM, must vary in hot waterflooding.

To incorporate dynamics in the time constant, two approaches were pursued in this work. In the first, equations describing the temperature dynamics were developed and coupled with the pressure and saturation equations in a fashion similar to the coupled CRM (coupled CRM (CCRM)) approach proposed by Cao [9]. Cao's approach incorporated the saturation changes by developing and simultaneously solving the pressure and saturation CRM equations. Through this coupling mechanism, the time constant, while constant at each time step, was able to vary across the entire fitting window as the saturation dynamics dictated. The CCRM, when validated, showed impressive history matches demonstrating the applicability of this method and thus motivating our development of a TCCRM.

In the second approach, the differential equations describing pressure, saturation, and temperature dynamics are developed, linearized, and combined to yield a non-first order transfer function that models the total fluid production rate. This approach, referred to in this work as the LCCRM, is pursued to obtain a model that is potentially more capable at capturing high-order dynamics resulting from the interactions between the three fundamental

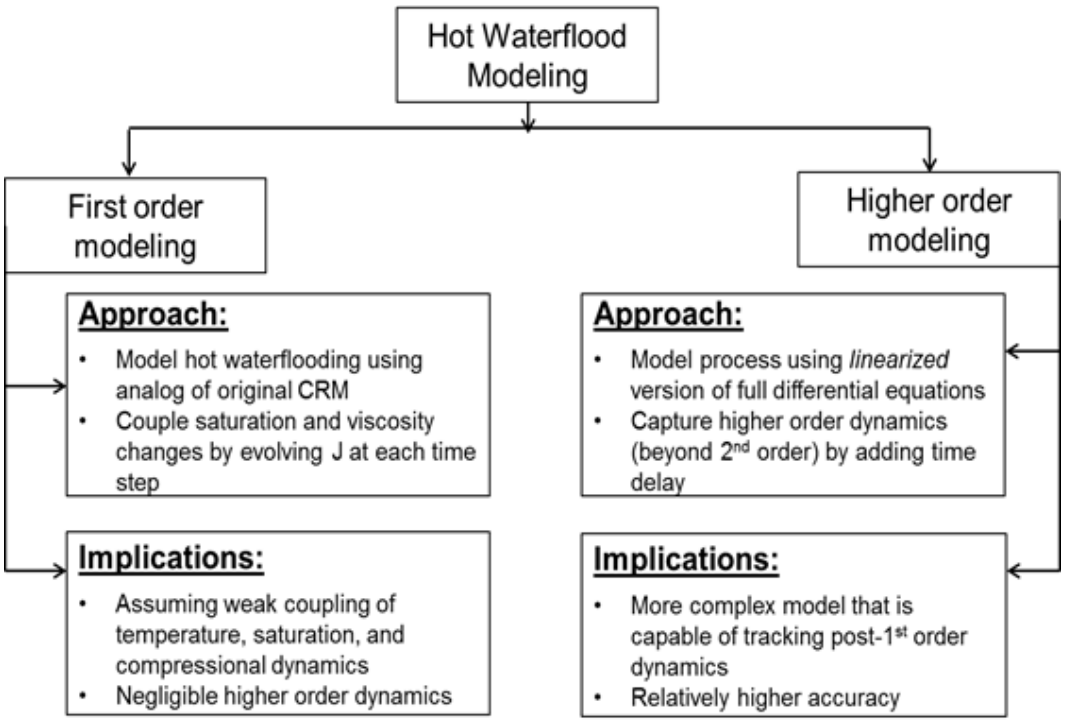

Figure 6.9: Hot waterflood modeling approaches

processes (hydraulic, saturation changes, and reservoir heating) inherent in a hot waterflooding process. These approaches are summarized in Figure 6.9 and described in more details in the subsequent sections.

6.3.1 Derivation of the Thermal Coupled CRM (TCCRM)

For the drainage area surrounding a producer, Sayarpour [55] solved the differential equation for the CRM using the principle of superposition in time to obtain an analytical form for the producer-based CRM (CRMP). The model parameters, i.e., the time constant and interwell connectivities or

gains, were estimated through a constrained least squares fitting procedure. Although the model was developed initially for mature waterflooding where water cut is high and constant, Cao et al., [11] developed a CRM variant applicable to early stage water floods in which the water cut is typically low and rapidly changing. This CRM variant was able to achieve better results in early water floods by coupling the pressure equation, i.e., the original CRM, with a numerically integrated saturation model. The coupling of the pressure and saturation equations enabled an update of the productivity indices to reflect the dynamics in fluid flow, making the time constants, which were constant in the original CRM, to become time varying.

In developing a capacitance resistance model applicable to thermally stimulated, heavy oil reservoirs, we start by coupling ODEs describing saturation and temperature dynamics with the original CRM equation. The solutions to these ordinary differential equation (ODE) are used, like in Cao et al's work, to update the time constants and thus enable the capture of changes in reservoir conditions that drive production. This gives rise to the thermal coupled TCCRM, the development and validation of which the following sections describe in detail.

6.3.1.1 Derivation of the Pressure Equation

The TCCRM is derived by coupling the pressure equation with the saturation and temperature equations. This coupling is achieved by solving the ODEs describing saturation and temperature changes and then using the

results to update the time constants of the pressure equation. The derivation is done for a control volume representing the drainage area surrounding a single producer in a hot waterflooded reservoir.

In deriving the TCCRM, we invoke the following assumptions:

- Water and oil phases coexist immiscibly in the reservoir. No gas is present in the reservoir.
- Rock properties and all fluid properties (excluding oil viscosity) do not change significantly and are thus considered constant.
- The number of wells, as well as overall reservoir configuration remain unchanged within the considered (i.e., fitting) time period.
- Capillary pressure and gravity effects are negligible.
- Darcy's law applies.

These assumptions mirror those invoked in the development of the original CRM as presented in [57]. The only difference is that here we do not assume constant productivity index for the producer(s) because of the non-isothermal nature of hot waterflooding. As we will show, this difference is the source of the time varying nature of the time constant terms in the TCCRM.

The mass conservation equations for oil and gas phases respectively in the control volume around a producer j, can be written as follows:

$$V_b \frac{d(\varphi \rho_w \bar{S}_w)}{dt} = \sum_{i=1}^{N_{inj}} f_{ij} \rho_w I_i(t) - \rho_w q_w(t) \tag{6.4}$$

$$V_b \frac{d(\varphi \rho_o \bar{S}_o)}{dt} = - \rho_o q_o(t) \tag{6.5}$$

where V_b is the bulk volume of the control volume, φ is porosity, ρ is fluid density, $\bar{S}$is average fluid saturation in the control volume, N_{inj} is the total number of injectors, f_{ij} is the fraction of water from injector i flowing into producer j's control volume at steady state, $I_i(t)$ is water injection rate of injector i at time t, and $q(t)$ is fluid production rate. Subscripts "w" and "o" denote water and oil phase properties respectively.

Using the product rule, Equations 6.4 and 6.5 can be expanded to yield:

$$V_P \left[\frac{d\bar{S}_w}{dt} + \bar{S}_w (c_f + c_w) \frac{d\bar{P}}{dt} \right] = \sum_{i=1}^{N_{inj}} f_{ij} I_i(t) - q_w(t) \tag{6.6}$$

$$V_P \left[\frac{d\bar{S}_o}{dt} + \bar{S}_o (c_f + c_o) \frac{d\bar{P}}{dt} \right] = - q_o(t) \tag{6.7}$$

Here, $\bar{P}$ denotes the average pressure within the control volume, c_f, $c_o$and c_w represent formation, oil and water compressibilities respectively. Knowing that $\bar{S}_w + \bar{S}_o = 1$, since only water and oil phases are present in the reservoir, we can combine Equations 6.6 and 6.7, eliminate saturation derivatives, and obtain:

$$V_P c_t \frac{d\bar{P}}{dt} = \sum_{i=1}^{N_{inj}} f_{ij} I_i(t) - q_t(t) \tag{6.8}$$

where c_t is the total compressibility, which is given as $c_f + \bar{S}_o c_o + \bar{S}_w c_w$, and q_t is the total fluid production, calculated as $q_o(t) + q_w(t)$.

Equation 6.8, which is called the pressure equation, is the governing material balance equation for the entire control volume on a total fluid basis. To enable integrating this equation, an intermediate relationship linking the total production rate with the average pressure is required. A linear productivity model for producer j as defined in Walsh and Lake (2003) is used to satisfy this requirement. This productivity equation is shown in Equation 6.9:

$$q_t(t) = J_j(t)\left[\bar{P}(t) - P_{wf}(t)\right] \tag{6.9}$$

where $J_j(t)$ is producer j's productivity index, and $P_{wf}(t)$ is the producer's bottomhole pressure at time t.

Eliminating $\bar{P}(t)$ in Equation 6.8 using Equation 6.9 gives:

$$V_P c_t \frac{d}{dt}\left[\frac{q_t(t)}{J_j(t)} + P_{wf}(t)\right] = \sum_{i=1}^{N_{inj}} f_{ij} I_i(t) - q_t(t) \tag{6.10}$$

The productivity index, $J_j(t)$, is given as:

$$J_j(t) = \frac{2\pi hk}{\frac{1}{2} ln\left[\frac{4A}{\gamma C_A r_{w_j}^2}\right]}\left(\frac{k_{ro_j}(t)}{\mu_{o_j}(t)} + \frac{k_{rw_j}(t)}{\mu_{w_j}(t)}\right) \tag{6.11}$$

where h is the thickness of the control volume, k is absolute permeability, A is the drainage area, C_A is shape factor, γ is Euler's coefficient, r_w is wellbore radius, $k_{ro}(t)$ and $k_{rw}(t)$ are oil and water relative permeabilities at time t respectively, $\mu_o(t)$ and $\mu_w(t)$ are oil and water viscosities at time t respectively.

As can be seen, the productivity index for a hot waterflooded reservoir, unlike that of a mature water flood, is not constant but evolves with changes in oil and water relative permeabilities and viscosities. Therefore, to calculate production rates using Equation 6.10, ancillary equations describing the dynamics in saturation and viscosity of the fluid phases are required.

By assuming constant producer BHP, J_j, and I_i at each discrete time step k, Equation 6.10 can be integrated to obtain the Thermally Coupled CRM equation as shown in Equation 6.12. These assumptions result in a time constant, τ_j, which is constant for each time step k. The time constant is given by Equation 6.13.

$$q_j^k = q_j^{k-1} e^{\frac{-\Delta t}{\tau_j^k}} + (1 - e^{\frac{-\Delta t}{\tau_j^k}}) \sum_{i=1}^{N_{inj}} f_{ij} I_i^k \tag{6.12}$$

$$\tau_j^k = \frac{c_t V_P}{{J_j}^k} \tag{6.13}$$

where q_j^k is the production rate from producer j at time step k, q_j^{k-1} is production rate from producer j at time step *k-1*, $\Delta t$is the time interval between time steps k and *k-1*, $\tau_j^k$is the time constant of producer j at time

step k, f_{ij} is the gain or interwell connectivity between injector i and producer j, and I_i^k is the injection rate at injector$i$ at time step k.

Details of the integration are presented in [11]. Because waterflooding is isothermal, Cao's Coupled CRM (CCRM) required updating the time constants at each time step with only the current relative permeability values. In the TCCRM however, the time constants, τ_j^k, must be updated at each time step k with current relative permeability and viscosity values. The following section will discuss the development and coupling of the temperature and saturation equations with the CCRM to give the TCCRM.

6.3.1.2 Derivation of the Saturation Equation

Equation 6.11 shows that the productivity index depends on time-varying relative permeabilities. These relative permeabilities depend directly on saturation dynamics by way of Corey-type power law correlations [14]. Thus,

$$k_{ro}(t) = k_{ro}(S_o) = k_{ro}^o \left(\frac{S_o(t) - S_{o,r}}{1 - S_{o,r} - S_{w,r}} \right)^{n_1} \tag{6.14}$$

$$k_{rw}(t) = k_{rw}(S_w) = k_{rw}^o \left(\frac{S_w(t) - S_{w,r}}{1 - S_{o,r} - S_{w,r}} \right)^{n_2} \tag{6.15}$$

where k_{ro}^o and k_{rw}^o are oil and water endpoint relative permeabilities respectively, $S_{o,r}$and $S_{w,}$ are oil and water residual saturations respectively,

$S_o$and S_w are oil and water saturations at the outlet (i.e., producer), and n_1 and n_2 are the exponents for oil and water correlations respectively.

To derive the saturation equation, we eliminate the pressure derivative in Equation 6.6 using Equation 6.7:

$$V_P \frac{d\bar{S}_o}{dt} = -\frac{\bar{S}_o(c_f + c_o)}{c_t} \left[\sum_{i=1}^{N_{inj}} f_{ij} I_i(t) - q_t(t) \right] - q_o(t) \tag{6.16}$$

Assuming that c_t varies negligibly with saturation and solving numerically for producer j, the explicit solution for Equation 6.16 at discrete time step k is:

$$\bar{S}_{o,j}^k = \bar{S}_{o,j}^{k-1} - \frac{\Delta t}{V_{p,j}} \left[\frac{\bar{S}_{o,j}^{k-1}(c_f + c_o)}{c_t} \left(\sum_{i=1}^{N_{inj}} f_{ij} I_i^k - q_{t,j}^k \right) + q_{o,j}^k \right] \tag{6.17}$$

In order to use Equation 6.17 to update the time constant, a relationship between the average saturation within the control volume and the outlet saturation, upon which relative permeability depends, is required. The Welge equation [69] provides this link as shown below.

$$S_{o,j}{}^k = \bar{S}_{o,j}^k + W_i(1 - f_w|_{x_D=1}) \tag{6.18}$$

where W_i is cumulative pore volume of water injected into the control volume (CV), calculated via Equation 6.19, and $f_w|_{x_D=1}$ is outlet water cut, calculated using Equation 6.20.

$$W_i = \sum_k \sum_i \frac{f_{ij} I_i^k}{V_{p,j}} \tag{6.19}$$

$$f_w|_{x_D=1} = 1 - \frac{q_o}{q_t} \tag{6.20}$$

Calculating W_i requires *a priori* knowledge of $V_{p,j}$, which is estimated using the Koval fractional flow equation [31]. This fractional flow relationship, which is used in history-matching water cut data to determine V_p, is shown in Equation 6.21.

$$f_w|_{x_D=1} = \begin{cases} 0, & W_i < \frac{1}{K_{val}} \\ \frac{K_{val} - \sqrt{\frac{K_{val}}{W_i}}}{K_{val} - 1}, & \frac{1}{K_{val}} < W_i < K_{val} \\ 1, & W_i > K_{val} \end{cases} \tag{6.21}$$

where K_{val} is the Koval factor. The Koval factor is also determined through history-matching.

6.3.1.3 Derivation of the Temperature Equation

Assuming negligible change in water viscosity with temperature, the dynamics in oil viscosity must be used in updating the productivity index and subsequently in calculating τ_j^k. In this work, it is assumed temperature is the primary cause of viscosity changes. This temperature effects on viscosity is modeled using the Andrade equation [5], which represents an exponential relationship between oil viscosity and average temperature within the control volume. This viscosity model due to Andrade is used in this work because

of its simplicity. Particularly, this model does not require knowledge of fluid properties such as specific gravity, pour point temperature etc that are unique properties for a particular oil.

$$\mu_{o_j}(t) = A \cdot e^{\frac{B}{T_j(t)}} \tag{6.22}$$

where A and B are predetermined correlation parameters.

We model the average reservoir temperature by developing an EBTM for the control volume surrounding a single producer. According to Lake [32], the energy balance for the control volume with no conductive heat transport and negligible heat loss can be written as follows:

$$V_b \frac{d}{dt}(\rho \bar{U}) + \dot{H}_P - \dot{H}_{inj} = -\dot{Q} \tag{6.23}$$

where $\dot{H}_P$ is rate of enthalpy production, $\dot{H}_{inj}$is rate of enthalpy injection, and $\dot{Q}$ is rate of energy loss in the control volume (CV).

Neglecting compression work and replacing U with H, assuming no energy losses in the CV and rearranging, the Equation 6.23 can be rewritten as follows:

$$V_b \frac{d}{dt}(\rho \bar{H}) = \dot{H}_{inj} - \dot{H}_P \tag{6.24}$$

For the three components in the reservoir system, i.e., water, oil and reservoir rock, Equation 6.24 can be expanded to obtain:

$$V_b \frac{d}{dt}\left[\varphi\left(\rho_w S_w H_w + \rho_o S_o \bar{H}_o\right) + (1-\varphi)\rho_R H_R\right] = \dot{H}_{inj} - \dot{H}_P \qquad (6.25)$$

where subscript R applies to rock properties, "w" and "o" to water and oil respectively.

Using the definition of enthalpy, we expand Equation 6.25 further to obtain:

$$V_b \frac{d}{dt}\left[\varphi\left(\rho_w S_w C_{p,w} T + \rho_o S_o \bar{C}_{p,o} T\right) + (1-\varphi)\rho_R C_{p,R} T\right] = \dot{H}_{inj} - \dot{H}_P \quad (6.26)$$

Assuming porosity, individual densities and heat capacities are negligible functions of time, then Equation 6.26 becomes:

$$V_b \left[\varphi\rho_w C_{p,w} \frac{d\bar{S}_w \bar{T}}{dt} + \varphi\rho_o C_{p,o} \frac{d\bar{S}_o \bar{T}}{dt} + (1-\varphi)\rho_R C_{p,R} \frac{d\bar{T}}{dt}\right] = \dot{H}_{inj} - \dot{H}_P \qquad (6.27)$$

where $\bar{T}$ is the average temperature in the control volume (CV) and all other variables retain their assigned meanings.

Knowing that $\bar{S}_w + \bar{S}_o = 1$, Equation 6.27 can be rewritten as follows:

$$V_b \left[\varphi\rho_w C_{p,w} \frac{d(1-\bar{S}_o)\bar{T}}{dt} + \varphi\rho_o C_{p,o} \frac{d\bar{S}_o \bar{T}}{dt} + (1-\varphi)\rho_R C_{p,R} \frac{d\bar{T}}{dt}\right] = \dot{H}_{inj} - \dot{H}_P \quad (6.28)$$

Expanding the derivative on the left side of Equation 6.28:

$$V_b\left[\varphi\rho_w C_{p,w}(\frac{d\bar{T}}{dt}-\frac{d\bar{S}_o\bar{T}}{dt})+\varphi\rho_o C_{p,o}\frac{dS_o\bar{T}}{dt}+(1-\varphi)\rho_R C_{p,R}\frac{d\bar{T}}{dt}\right]= \dot{H}_{inj}-\ \dot{H}_P \quad (6.29)$$

Expanding and rearranging the right side of Equation 6.29:

$$V_b\left[\left(\varphi\rho_o C_{p,o}-\varphi\rho_w C_{p,w}\right)\frac{d\bar{S}_o\bar{T}}{dt}+\left[(1-\varphi)\,\rho_R C_{p,R}+\varphi\rho_w C_{p,w}\right]\frac{d\bar{T}}{dt}\ \right] \quad (6.30)$$

$$V_b\Bigg[\left(\varphi\rho_o C_{p,o}-\varphi\rho_w C_{p,w}\right)\left(\frac{\bar{S}_o d\bar{T}}{dt}+\frac{\bar{T}d\bar{S}_o}{dt}\right)+ \left[(1-\varphi)\,\rho_R C_{p,R}+\varphi\rho_w C_{p,w}\right]\frac{d\bar{T}}{dt}\Bigg] \quad (6.31)$$

$$V_b\Bigg[\left(\varphi\rho_o C_{p,o}-\varphi\rho_w C_{p,w}\right)\frac{\bar{T}d\bar{S}_o}{dt}+\left(\varphi\rho_o C_{p,o}-\varphi\rho_w C_{p,w}\right)\frac{\bar{S}_o d\bar{T}}{dt}+ \left[(1-\varphi)\,\rho_R C_{p,R}+\varphi\rho_w C_{p,w}\right]\frac{d\bar{T}}{dt}\Bigg] \quad (6.32)$$

$$V_b\Bigg[\left(\varphi\rho_o C_{p,o}-\varphi\rho_w C_{p,w}\right)\frac{\bar{T}d\bar{S}_o}{dt}+\{(1-\varphi)\,\rho_R C_{p,R}+\varphi\rho_w C_{p,w}+ \bar{S}_o\left(\varphi\rho_o C_{p,o}-\varphi\rho_w C_{p,w}\right)\}\frac{d\bar{T}}{dt}\Bigg] \quad (6.33)$$

For the left side of Equation 6.29:

$$\dot{H}_{inj} = \sum_{i=1}^{N_{inj}} f_{ij} I_i \rho_w C_{p,W} T_{inj,i} \tag{6.34}$$

$$\dot{H}_P = q_w \rho_w C_{p,w} \bar{T} + q_o \rho_o C_{p,o} \bar{T} = (f_w \rho_w C_{p,w} + f_o \rho_o C_{p,o}) q_t \bar{T} \tag{6.35}$$

Knowing that $f_w + f_o = 1$, Equation 6.35 becomes:

$$\dot{H}_P = ((1 - f_o)\rho_w C_{p,w} + f_o \rho_o C_{p,o}) q \bar{T} = \left(f_o(\rho_o C_{p,o} - \rho_w C_{p,w}) + \rho_w C_{p,w}\right) q_t \bar{T} \tag{6.36}$$

Combining Equations 6.33, 6.34, 6.36, and dividing through by the expression $(\rho_o C_{p,o} - \rho_w C_{p,w})$, we obtain the energy balance tank model (EBTM).

$$V_b \varphi \left[\frac{\bar{T} d\bar{S}_o}{dt} + \{ \frac{\rho_w C_{p,w} + \frac{(1-\varphi)}{\varphi} \rho_R C_{p,R}}{\rho_o C_{p,o} - \rho_w C_{p,w}} + \bar{S}_o \} \frac{d\bar{T}}{dt} \right] = \frac{\rho_w C_{p,w}}{\rho_o C_{p,o} - \rho_w C_{p,w}} \sum_{i=1}^{N_{inj}} f_{ij} I_i T_{inj,i} - \left(f_o + \frac{\rho_w C_{p,w}}{\rho_o C_{p,o} - \rho_w C_{p,w}} \right) q_t \bar{T} \tag{6.37}$$

This equation captures the dynamics in average reservoir temperature, which is necessary for accurate evolution of the time constants. Denoting $\frac{\rho_w C_{p,w}}{\rho_o C_{p,o} - \rho_w C_{p,w}}$ as α and $\frac{\rho_w C_{p,w} + \frac{(1-\varphi)}{\varphi} \rho_R C_{p,R}}{\rho_o C_{p,o} - \rho_w C_{p,w}}$ as β, the EBTM equation can be written in a compact form as:

$$V_P \left[\frac{\bar{T} d\bar{S}_o}{dt} + \{\bar{S}_o + \beta\} \frac{d\bar{T}}{dt} \right] = \alpha \sum_{i=1}^{N_{inj}} f_{ij} I_i T_{inj,i} - (f_o + \alpha) q_t \bar{T} \qquad (6.38)$$

Equation 6.38 is solved numerically coupled with the saturation and pressure equations, and then used to update productivity index and then time constant values.

6.3.2 Derivation of the Linearized Coupled Capacitance Resistance Model (LCCRM)

As shown in the previous section, the dynamics of hot waterflooding can be fully described by solving the pressure, saturation, and temperature equations simultaneously. Section 6.3.1 showed a method of modifying the original CRM by updating the time constants based on temperature and saturation calculations. The underlying assumption in the above approach is a weak interaction between saturation/temperature dynamics and the dominant pressure dynamics, which will cause minimal deviation from the exponential approach profile of the production response to a step change in injection rate. This assumption holds true for mature hot water floods where temperature, saturation, and pressure dynamics are at or close to steady state. In early hot water flood scenarios, however, the interactions between saturation and pressure dynamics and particularly between temperature and pressure dynamics are strong, greatly increasing the influence of temperature and saturation changes on production rates. In this section, we develop a linearized Coupled Capacitance Resistance Model (LCCRM) that is capable of capturing these

dynamics in early and late hot water flood.

From the previous section, the governing equations for a hot water flood can be written in matrix form as follows:

$$\begin{bmatrix} V_p c_t & 0 & 0 \\ V_p \bar{S}_o (c_f + c_o) & V_p & 0 \\ 0 & V_p \bar{T} & V_p \left(\bar{S}_o + \beta\right) \end{bmatrix} \begin{bmatrix} \frac{d\bar{P}}{dt} \\ \frac{d\bar{S}_o}{dt} \\ \frac{d\bar{T}}{dt} \end{bmatrix} = \begin{bmatrix} \sum_i f_{ij} I_i - J_t \left(\bar{P} - \bar{P}_{wf}\right) \\ -q_o \\ \alpha \sum_i f_{ij} I_i T_{inj,i} - \left(f_o + \alpha\right) q_t \bar{T} \end{bmatrix} \tag{6.39}$$

Using the linear productivity model and assuming constant bottomhole pressure and water viscosity, Equation 6.39 can be rewritten as:

$$\begin{aligned} \frac{d\bar{T}}{dt} &= \frac{\alpha}{V_P(\bar{S}_o+\beta)} \sum_{i=1}^{N_{inj}} f_{ij} I_i T_{inj,i} - \left[\frac{(f_o+\alpha) q_t}{V_P(\bar{S}_o+\beta)} - \frac{\bar{S}_o\left(c_f + c_o\right)\left(\sum_{i=1}^{N_{inj}} f_{ij} I_i - q_t\right)}{c_t V_P\left(\bar{S}_o+\beta\right)} - \right. \\ &\qquad \left. \frac{q_o}{V_P(\bar{S}_o+\beta)} \right] \bar{T} \\ \frac{d\bar{S}_o}{dt} &= \frac{-\bar{S}_o\left(c_f+c_o\right)}{c_t V_P} \left(\sum_{i=1}^{N_{inj}} f_{ij} I_i - q_t\right) - \frac{q_o}{V_p} \\ \frac{dq}{dt} &= \frac{J' \left[\frac{k_{ro}}{\mu_o} + \frac{k_{rw}}{\mu_w}\right]}{c_t V_p} \left(\sum_{i=1}^{N_{inj}} f_{ij} I_i - q_t\right) \end{aligned} \tag{6.40}$$

Equation 6.40, which we call the state equation, describes the evolution of the state variables namely, the average reservoir temperature (upon which oil viscosity depends), average oil saturation (upon which relative permeability depends), and total fluid production. The injection rate and the temperature of the injected fluid in each injector are considered the input (or manipulated)

variables, as they can be manipulated externally to alter the state (i.e., the temperature, saturation, and/or pressure) of the control volume.

The state equations are strongly nonlinear. The nonlinearities emanate chiefly from the exponential dependence of oil viscosity on temperature and also from the power law relationship between the relative permeabilities and saturation. These equations can be linearized using Taylors series expansion around an equilibrium point the following set of ordinary differential equations written in terms of deviation variables:

$$\begin{aligned} \frac{d\bar{T}}{dt} &= k_1 \textstyle\sum_i f_{ij} I_i + k_2 \sum_i \alpha f_{ij} I_{i,e} T_{inj,i} - k_3 q_t + k_4 \bar{S}_o - k_5 \bar{T} \\ \frac{d\bar{S}_o}{dt} &= -k_6 \bar{S}_o - k_7 \textstyle\sum_i f_{ij} I_i + k_8 q_t \\ \frac{dq}{dt} &= k_9 \textstyle\sum_i f_{ij} I_i - k_9 q_t + k_{10} \bar{S}_o + k_{11} \bar{T} \end{aligned} \tag{6.41}$$

Applying Laplace transforms and denoting $\alpha f_{ij} I_{i,e}$ as h_{ij}:

$$\begin{aligned} s\bar{T} &= k_1 \textstyle\sum_i f_{ij} I_i + k_2 \sum_i h_{ij} T_{inj,i} - k_3 Q + k_4 \bar{S}_o - k_5 \bar{T} \\ s\bar{S}_o &= -k_6 \bar{S}_o - k_7 \textstyle\sum_i f_{ij} I_i + k_8 Q \\ sQ &= k_9 \textstyle\sum_i f_{ij} I_i - k_9 Q + k_{10} \bar{S}_o + k_{11} \bar{T} \end{aligned} \tag{6.42}$$

Deriving the individual transfer functions:

$$\begin{aligned} \bar{T} &= \tfrac{k_1}{s+k_5} \textstyle\sum_i f_{ij} I_i + \tfrac{k_2}{s+k_5} \sum_i h_{ij} T_{inj,i} - \tfrac{k_3}{s+k_5} Q + \tfrac{k_4}{s+k_5} \bar{S}_o \\ \bar{S}_o &= -\tfrac{k_7}{s+k_6} \textstyle\sum_i f_{ij} I_i + \tfrac{k_8}{s+k_6} Q \\ Q &= \tfrac{k_9}{s+k_9} \textstyle\sum_i f_{ij} I_i + \tfrac{k_{10}}{s+k_9} \bar{S}_o + \tfrac{k_{11}}{s+k_9} \bar{T} \end{aligned} \tag{6.43}$$

From Equation 6.43, we see that the three equations are tightly coupled. We proceed to derive the input-output relationship between the observable

state or output, i.e., the total production and the inputs – injection rate and temperature of injected fluid at each injector.

By substituting the first two relationship in Equation 6.43 into the third and writing for a single producer j, we obtain:

$$Q_j = \frac{k_9\left(s+k_5\right)\left(s+k_6\right)-k_7k_{10}\left(s+k_5\right)+k_1k_{11}\left(s+k_6\right)-k_4k_7k_{11}}{\left(s+k_5\right)\left(s+k_6\right)\left(s+k_9\right)-k_8k_{10}\left(s+k_5\right)+k_3k_{11}\left(s+k_6\right)+k_4k_8k_{11}}\sum_i f_{ij}I_i + \frac{k_2k_{11}\left(s+k_6\right)}{\left(s+k_5\right)\left(s+k_6\right)\left(s+k_9\right)-k_8k_{10}\left(s+k_5\right)+k_3k_{11}\left(s+k_6\right)+k_4k_8k_{11}}\sum_i h_{ij}T_{inj,i} \tag{6.44}$$

where h_{ij} represents the fractional enthalpy from injector i that contributes towards heating producer j's control volume at steady state. Observing the above equation, it can be seen that the transfer function indicates a third order process with second order numerator dynamics for the injection/production rate relationship, and a third order process with first order numerator dynamics for the injection temperature/production rate relationship. This is in stark contrast with the first-order process with no numerator dynamics observed in a cold water flooding scenario and can be attributed directly to the effect of saturation and temperature changes due to reservoir heating during hot water injection.

6.3.3 Model Validation

6.3.3.1 Validation of the Energy Balance Model

To track the evolution of viscosity (and consequently other key variables that depend on it), the changes in reservoir temperature over time must be obtained. One way to obtain the temporal changes in temperature is to develop a tank based energy (specifically heat) balance, the solution of which would yield the necessary temperature profile of the reservoir. Section 6.3.1.3 covered the derivation of this energy balance model. In this section, numerical solution of this model and comparison with simulated data is presented to demonstrate model validation.

The energy balance tank model was validated by solving numerically in MATLAB using the differential equation solver *ode45*. The solution was then compared to the average temperature of the reservoir as simulated in a commercial thermal simulator (CMG STARS). The graphical comparison is show in Figure 6.10. Further, a calculation of the viscosity using the EBTM generated temperature data is compared to the average oil viscosity obtained from the simulation. The result is presented in Figure 6.11.

As seen from Figure 6.10, there is a good match between the average reservoir temperature obtained from simulation and that predicted by the model, particularly early on in the hot waterflooding process. There is some mismatch around the middle of the hot waterflood, when all the three fundamental processes are in unsteady state and possibly coupling to create strong interactions. This mismatch dissipates towards the end of the thermal

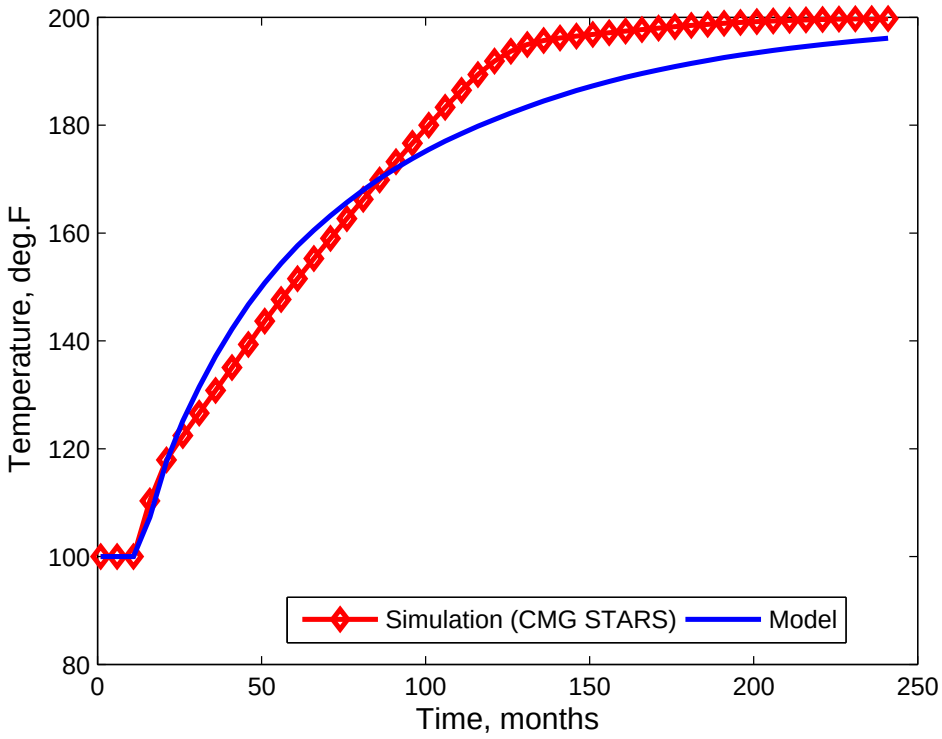

Figure 6.10: Graphical comparison between average temperature from simulation and from EBTM

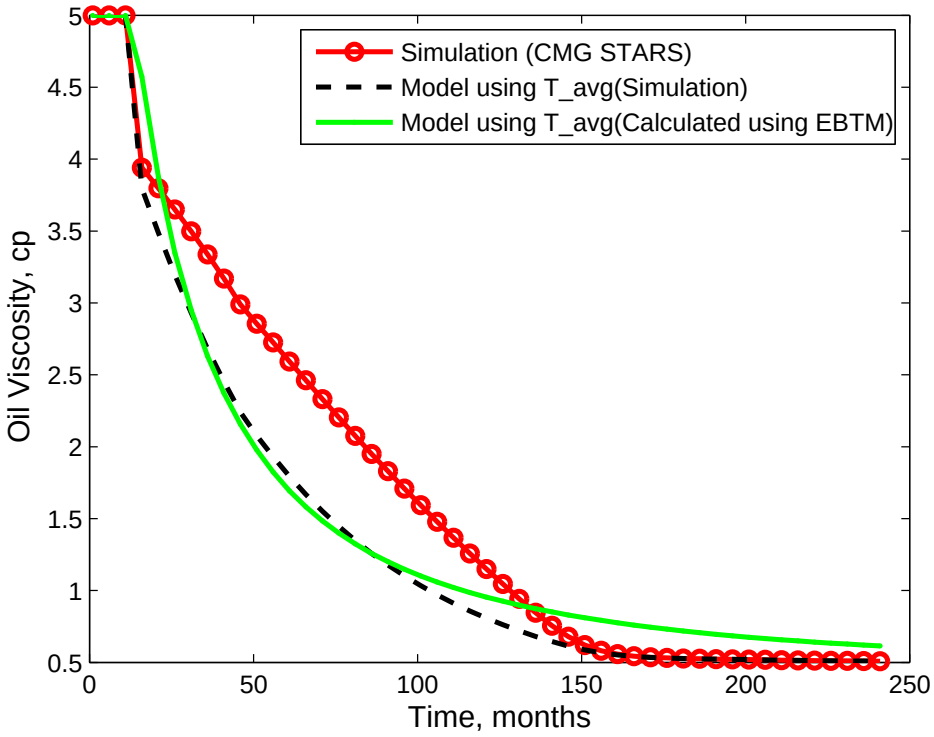

Figure 6.11: Comparison between Average Oil Viscosities from Simulation and Model

stimulation as the processes approach steady state.

Figure 6.10 shows that the EBTM developed in this work is sufficiently robust to describe the dynamics in reservoir temperature. To our knowledge, this is the first demonstration of the efficacy of this modeling approach for thermal stimulation modeling. Thus, while this model was used for hot waterflood modeling in this work, the modeling approach is general and can be applied, with the appropriate adjustments, to other thermal stimulation processes such as steamflooding, in situ combustion, SAGD, etc.

Figure 6.11 compares average oil viscosity obtained from the simulation to those calculated by applying EBTM generated simulation generated average temperature data to the Andrade equation [5]. The figure shows an impressive match between the viscosity values calculated by applying average temperature data to the Andrade equation. However, the match between calculated and simulated viscosity values, while satisfactory, is not as impressive. This is mainly because of the empirical nature of the Andrade equation in which the dependence of viscosity on temperature is described exponentially by only two constants, A and B. While this equation has remained in use as a simple way to capture viscosity-temperature relationship in the first order, its shortcomings have been demonstrated (Jones, 1981). Thus, improving the Andrade equation and/or exploring other viscosity-temperature modeling approaches that could yield better matches is a future effort that would be worthwhile towards extending the CRM to thermal recovery processes.

6.3.4 Validation of the TCCRM

In this section, the validation of the TCCRM using synthetic data is presented. Three test cases were simulated with different injection profiles and well configurations in a commercial reservoir simulator (CMG STARS). To validate TCCRM, production data generated by the reservoir simulation software were compared to model predicted production rates for each of the three cases.

In each case, the model was initialized by providing starting guesses of the model parameters (f_{ij} and θ_j). This requires provision of $N_{prd}(N_{inj}+1)$ initial estimates for a reservoir with N_{inj} injectors and N_{prd} producers. Initial parameter estimates are passed to the saturation and temperature equations, where they are used to track the saturation and average temperature changes in the producer control volume. At each time step k, the total mobility ratio, $M_j\,(k)$, is calculated using current values of outlet oil saturation and average temperature using Equation 6.45. The total mobility is then used to update θ_j to obtain the full time constant at time step k, $\tau_j\,(k)$, as shown in Equation 6.46.

$$M_j\,(k) = \left[\frac{k_{ro}(S_{oj})}{\mu_o(\bar{T}_j)} + \frac{k_{rw}(S_{oj})}{\mu_w}\right] \tag{6.45}$$

$$\tau_j\,(k) = \frac{\theta_j}{M_j(k)} \tag{6.46}$$

Reservoir temperature is calculated using the Energy Balance Tank Model (EBTM) derived in Section 6.3.1.3, while outlet oil saturation is calculated using the Welge equation as described in 6.3.1.2. In this work, the initial values of average oil saturation ($\bar{S}^0_{o,j}$)and average temperature ($\bar{T}^0_j$) are assumed to be known parameters. They may, however, be estimated in the model when unknown, increasing the number of estimated parameters in such a case to $N_{prd}(N_{inj}+3)$.

A least squares optimization approach was used to match the model predictions to the simulated data. This optimization routine was implemented in MATLAB® using a global search function that partitions the function space of the objective function into basins and scans through each basin to arrive at a good estimate of the global minimum. The optimization was subject to relevant constraints and bounds. The sections below details the two test cases performed to validate the model.

6.3.4.1 Case 1: Step Testing on a 1D Reservoir

In this scenario, a 1D reservoir was perturbed with a simultaneous step change in injection rate and temperature. Injection of hot water at 200°F was initiated January 2001 and continued until the end of the simulation. Simulation inputs are as shown in Table 6.4. Reservoir/well configurations are as shown in Figure 6.3.

Results of the simulation are presented in Figure 6.12, which shows three different stages of the production response. The first stage occurs before the breakthrough of the cold waterfront during which a cold water bank forms and only oil is produced from the reservoir (water cut is zero). The initial oil viscosity plays a dominant role in determining the production response as oil is the primary flowing phase. In the second stage, the cold water bank formed in the first stage breaks through. Here, the mobility of the heated oil relative to that of water and the relative permeability of the reservoir influence production. The final stage begins with the breakthrough of the hot water front and continues as the remaining mobile oil in the reservoir is produced (Jones, 1981); [38].

The results of the history-matching are presented in Figure 6.13. Figure 6.13A shows graphical comparison of model predicted production rate to that obtained via simulation. Figure 6.13B plots calculated and estimated time constant. Plotting TCCRM predicted production rates against CMG simulated rates showed a good match especially during the late stages of the hot water flood. Model mismatch was observed during the early and middle production stages, in which thermal maturity has not yet been attained. This mismatch was particularly significant during the early stages where saturation effects dominate flow. A comparison between calculated and model estimated time constant values also showed a good match particularly after thermal maturity.

From the results obtained, two key points are apparent. First, ther-

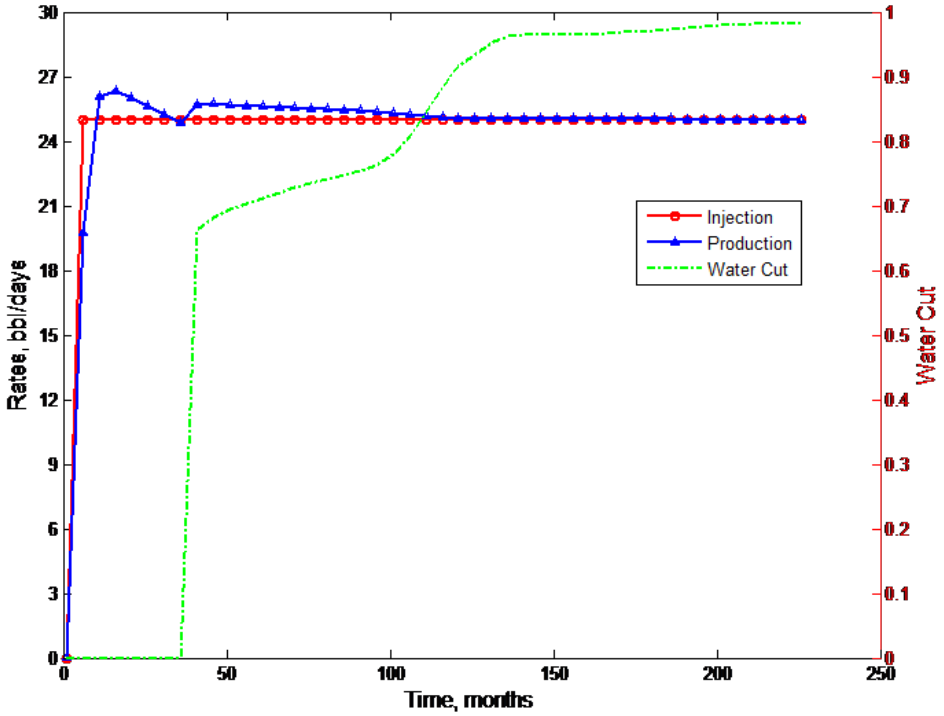

Figure 6.12: Rates and water cut as a function of time

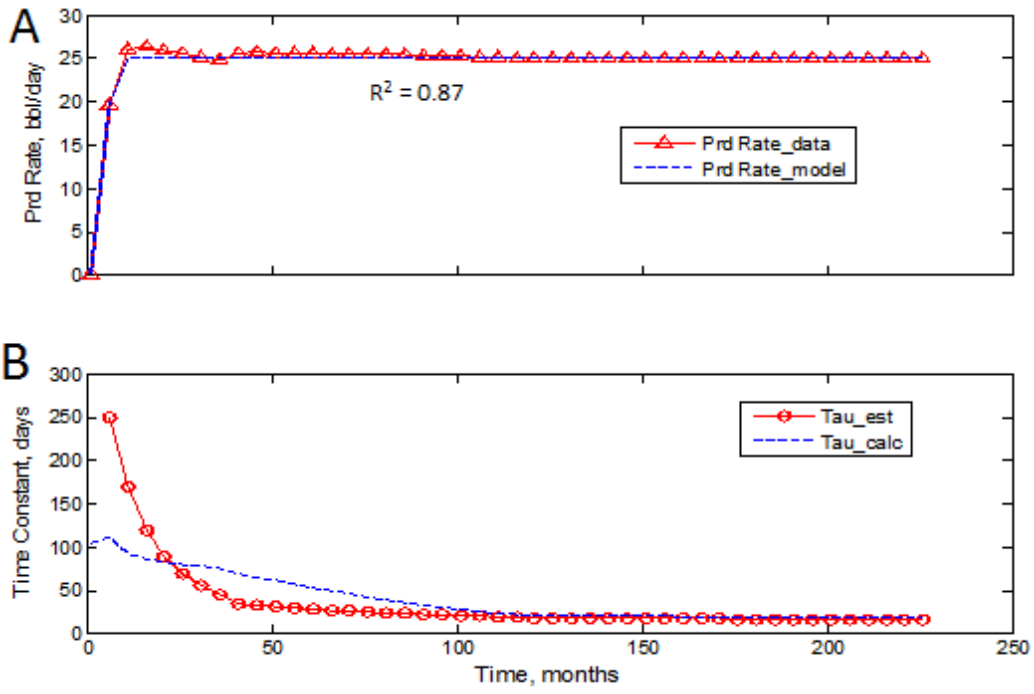

Figure 6.13: Results of history-matching for Case 1

mal stimulation is not a first-order process. This conclusion is based on the overshoot observed in the production response. Conceptually, the production response seems more consistent with the behavior of a higher order process (at least second order) observed in process control domain. The combination of saturation, compressional, and heat flow processes (each of which is first order) in a thermal stimulation process seems to result in a high order process that is exhibited by the production response.

Second, despite fitting a higher order process with a first order model, an overall good fit was obtained (as shown by a high R^2 value of 87%). We observed a poor fit at early times when the overshoot occurred because of the model structure mismatch. As shown in Figure 6.14, the mismatch coincided with a period of rapid reservoir temperature increase (as well as high but rapidly decreasing oil saturation), suggesting that the TCCRM, may be best applicable at stages when changes in the reservoir are more gradual. As the dimensionless average temperature, $\bar{T}_D$, (calculated via Equation 6.47) and average oil saturation stabilize after this period, an excellent match between model prediction and simulation data was observed.

$$\bar{T}_D(t) = \frac{\bar{T}(t) - T_o}{T_{inj} - T_o} \tag{6.47}$$

where $\bar{T}_D$ is the dimensionless average temperature, $\bar{T}$ is the average reservoir temperature at time t, $T_0$is the initial reservoir temperature, and T_{inj} is the temperature of the injected fluid.

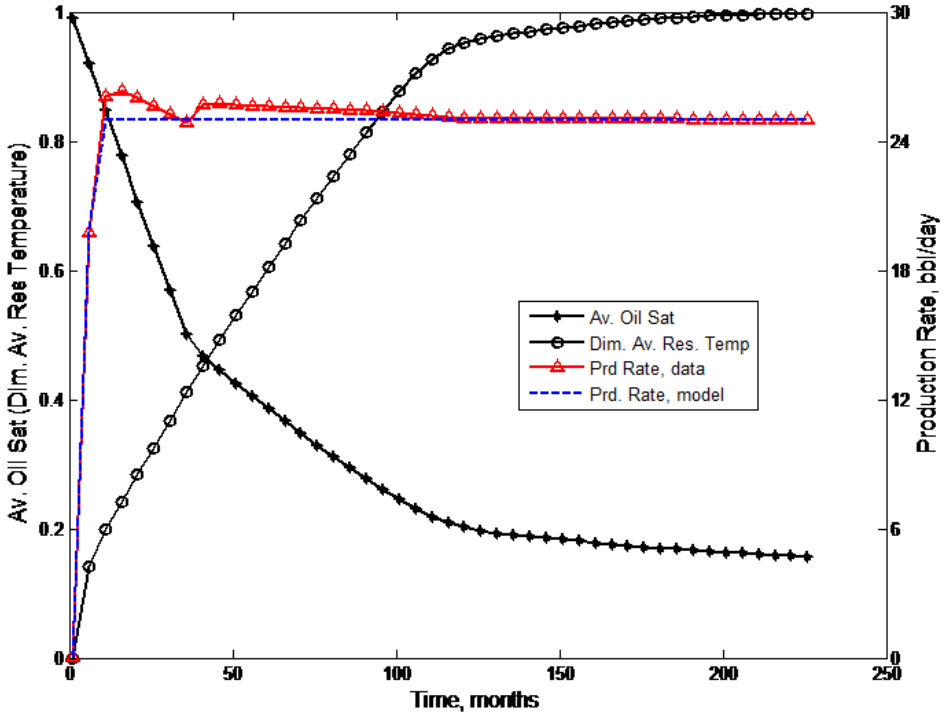

Figure 6.14: Average Saturation and Temperature Dynamics

6.3.4.2 Case 2: Validation with Variable Injection Rate in 2D Reservoir

For this Case, TCCRM was used in history-matching simulated data in which perturbations occurred on a monthly basis. The objectives here were twofold:

1. first, to demonstrate the robustness of the model for more complex reservoir configurations and injection profiles. This would provide insight into whether constant perturbation would be helpful in achieving better matches.

2. The previous case, in which significant mismatch was observed around sharp temperature and saturation changes (i.e., saturation and thermal fronts) suggested TCCRM incapability to track the fast dynamics. This is intuitive since the TCCRM is a first order model but intends to history-match a higher order process. Thus, a second objective is to confirm whether the TCCRM is more applicable at times when saturation and temperature are changing only gradually.

The simulation data used in this Case were the same as in the previous except for the input data summarized in Table 6.5. Low initial oil saturation was used in this Case in an attempt isolate and diminish the heavy influence

of saturation dynamics typical in immature hot waterfloods. The well configuration is shown in Figure 6.15. Figure 6.16 presents the injection rates applied to the reservoir. The reservoir configuration, as well as the injection rates for the five injectors, is identical to the streak case studied by Albertoni [3]. This streak case has been used by many researchers for model validation since it was introduced in 2003.

The reservoir is homogenous and the permeability is set to 5 md. This low permeability value is intended to restrict fluid flow and thus modulate hot water breakthrough. Such a scenario would allow for an observation of TCCRM performance at times when saturation and temperature are changing only gradually.

The results of history-matching production rates of the four producers in Case 2 are presented in Table 6.6 and through Figures 6.18 and 6.19. Table 6.6 shows the interwell connectivity estimates for producer-injector well pairs, while Figure 6.18 shows the evolution of producer time constants. The time constant estimates showed good agreement with calculated values. High values were observed for both model estimates and calculated time constants due to the low permeability nature of the reservoir in this Case.

Figure 6.19 shows a comparison of between simulation results and model estimate of production rate for each producer. Good matches were observed for all four producers with high R^2 values in each case. This results supports the hypothesis of TCCRM's applicability for hot water floods in which reservoir changes, as demonstrated in Figure 6.17, are more gradual.

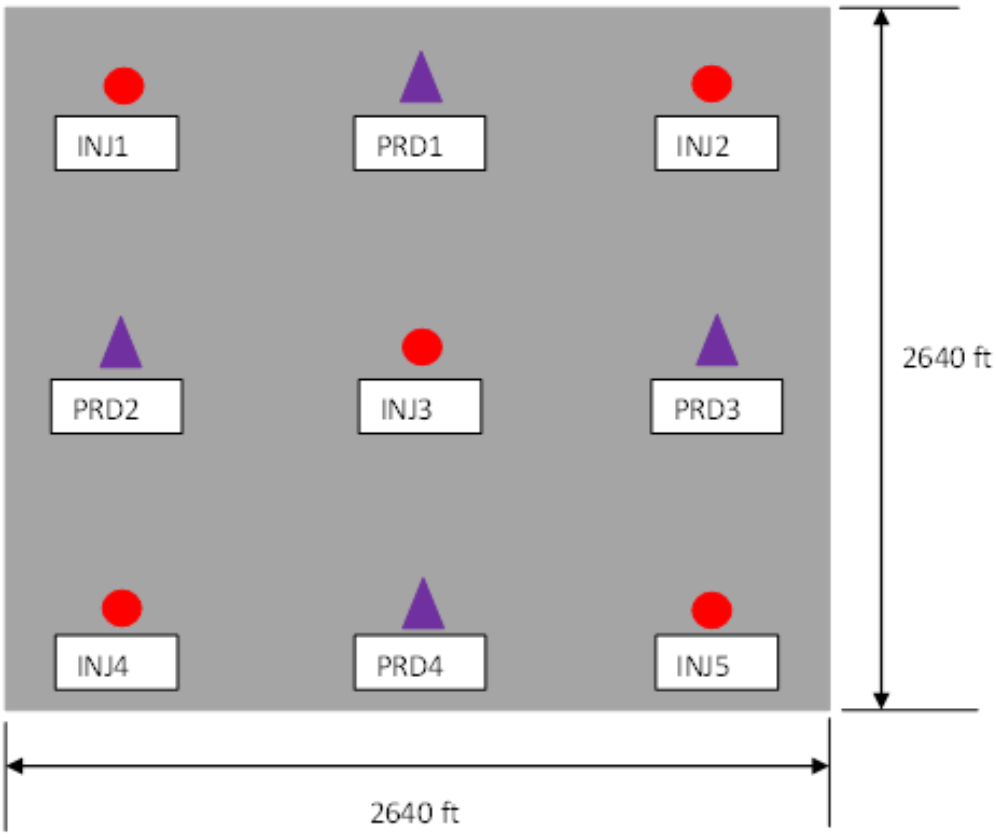

Figure 6.15: Reservoir dimensions and well configuration for Case 2

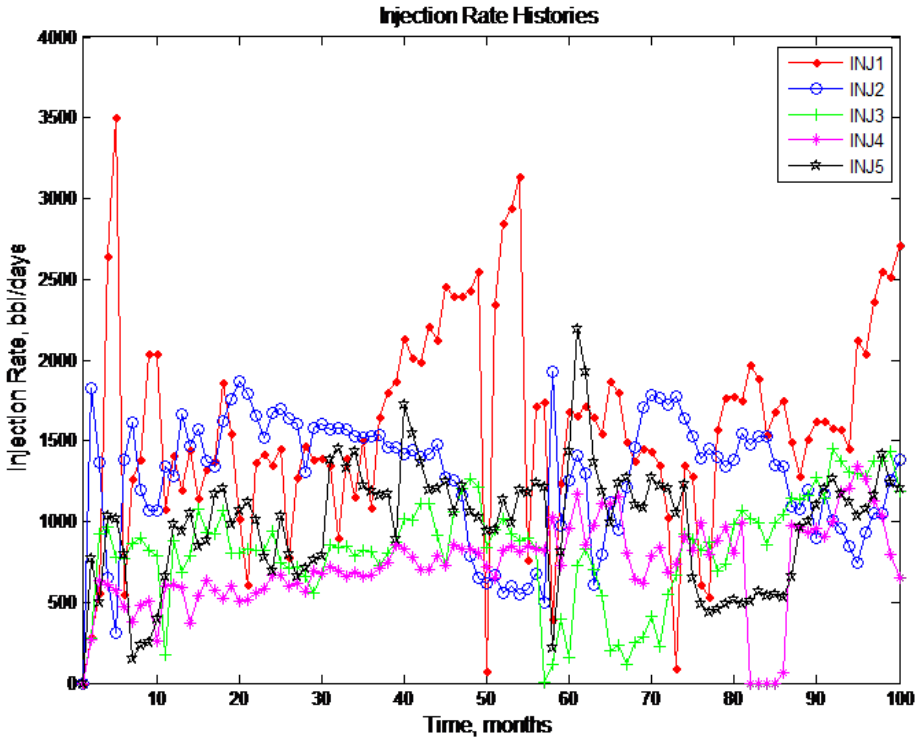

Figure 6.16: Variable hot water injection profile

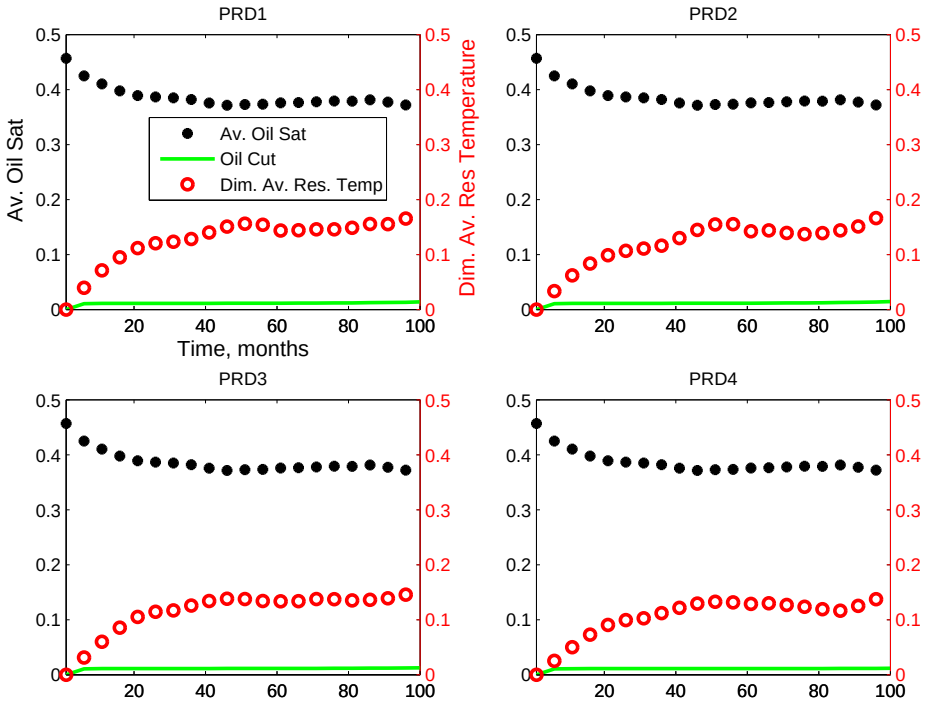

Figure 6.17: Average Saturation and Temperature Dynamics for Case 2

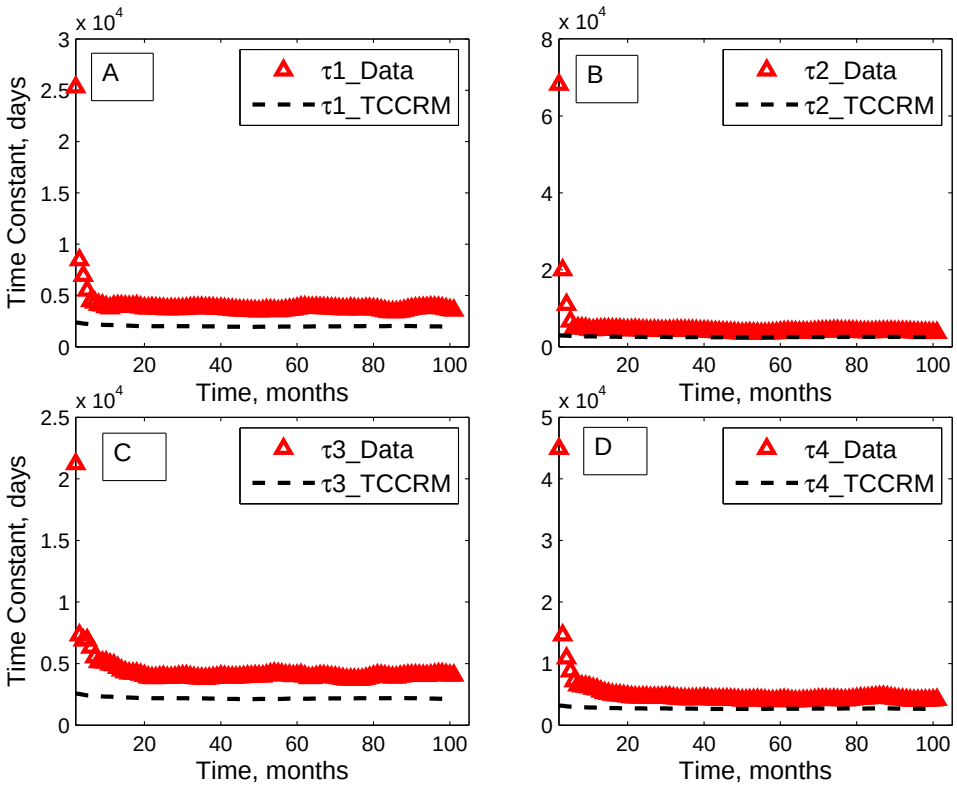

Figure 6.18: Comparison between calculated and estimated τ values for Case 2

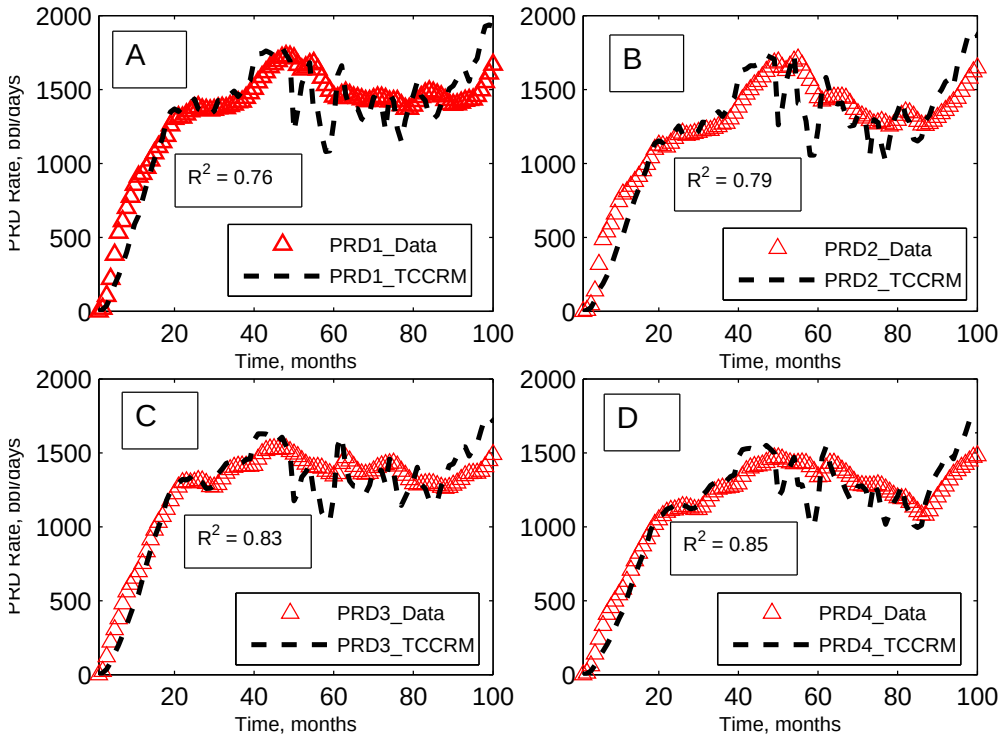

Figure 6.19: History-matching results for Case 2

6.3.4.3 Case 3: Validation with Variable Injection Rates in a Heterogeneous Field

To demonstrate TCCRM's applicability to heterogeneous reservoirs, the model was used in history-matching data simulated in CMG STARS for a 2D reservoir with two permeability streaks. The input data used in this Case were the same as in Case 2 except for the two high permeability channels connecting injector-producer pairs I1-P1 (5000 md) and I4-P3 (2000 md). The remainder of the reservoir matrix was kept at 5 md permeability value. The well configuration is shown in Figure 6.20.

History-matching results for Case 3 are presented in Table 6.7 and Figures 6.21 and 6.22. Table 6.7 shows the model estimates of the gains, while Figure 6.21 demonstrates the close match between simulated and model calculated production rate data for producers P1 to P4. Figure 6.22 shows the evolution of time constants for each of the producers. The figure shows a significantly reduced time constant values relative to Case 2 for producers connected to a high permeability channel.

We observe better matches for producers connected to the high permeability channels namely P1 and P4. Because the permeability channels are redistributing water away from producers P2 and P3 to producers P1 and P4, the production rates from P1 and P4 are higher, meaning that they make larger contributions to the overall objective function. Consequently, the residuals of these producers dominate the objective function since the overall fit is more sensitivity to these producer relative to P2 and P3. This effect is also

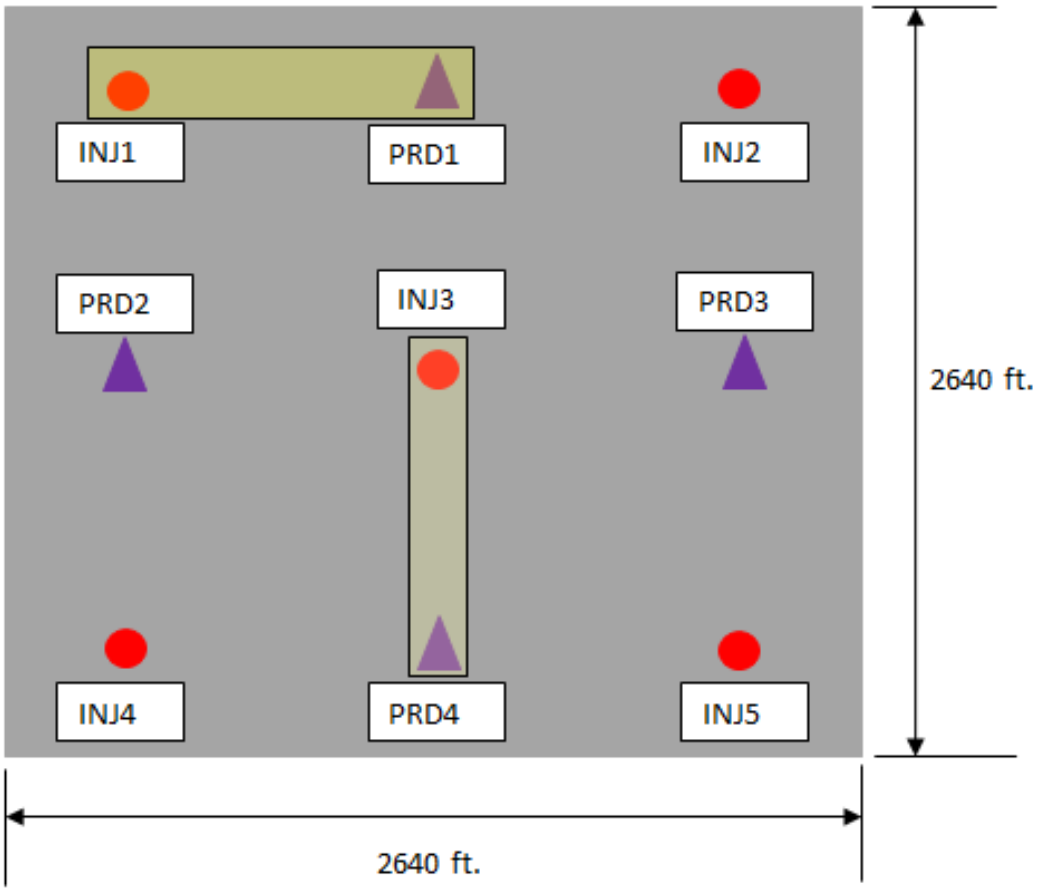

Figure 6.20: Reservoir dimensions and well configuration for Case 3

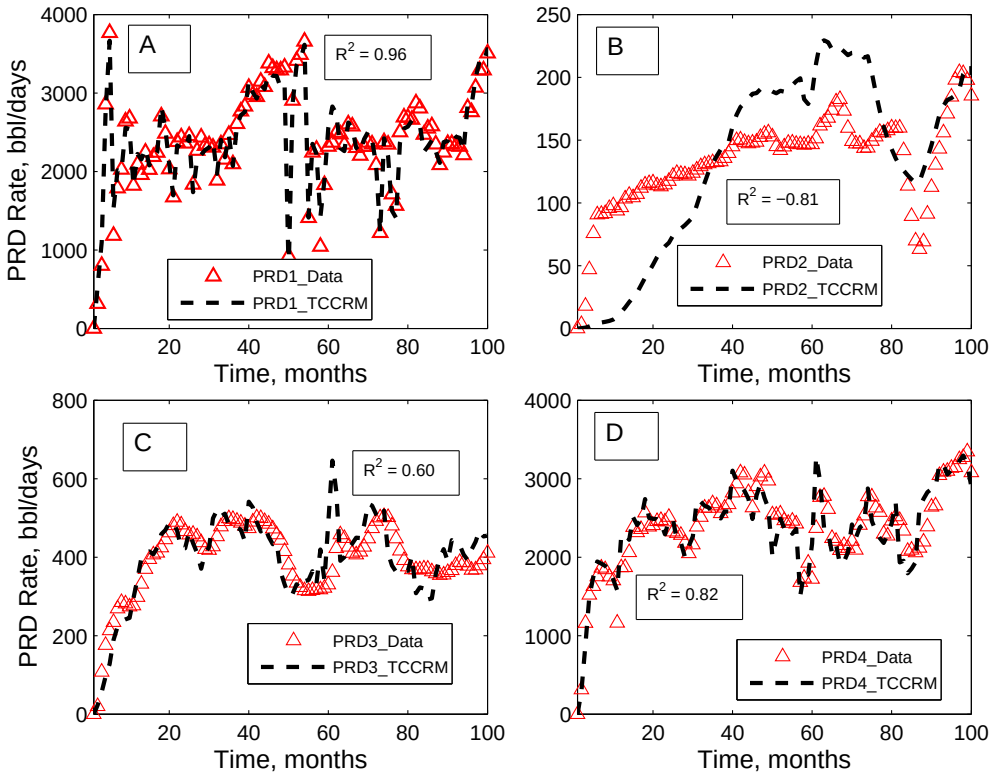

Figure 6.21: History-matching results for Case 3

observed when using the CRM for cold waterflooding as both models share a common objective function.

Results show that the TCCRM is capable of capturing the heterogeneity of the reservoir through the parameter estimates, particularly when the contrast in heterogeneity is high. This is illustrated by comparing history-matching results for Cases 2 and 3, as shown in Figure 6.23.

From Figure 6.23, it is apparent that where higher permeability contrast

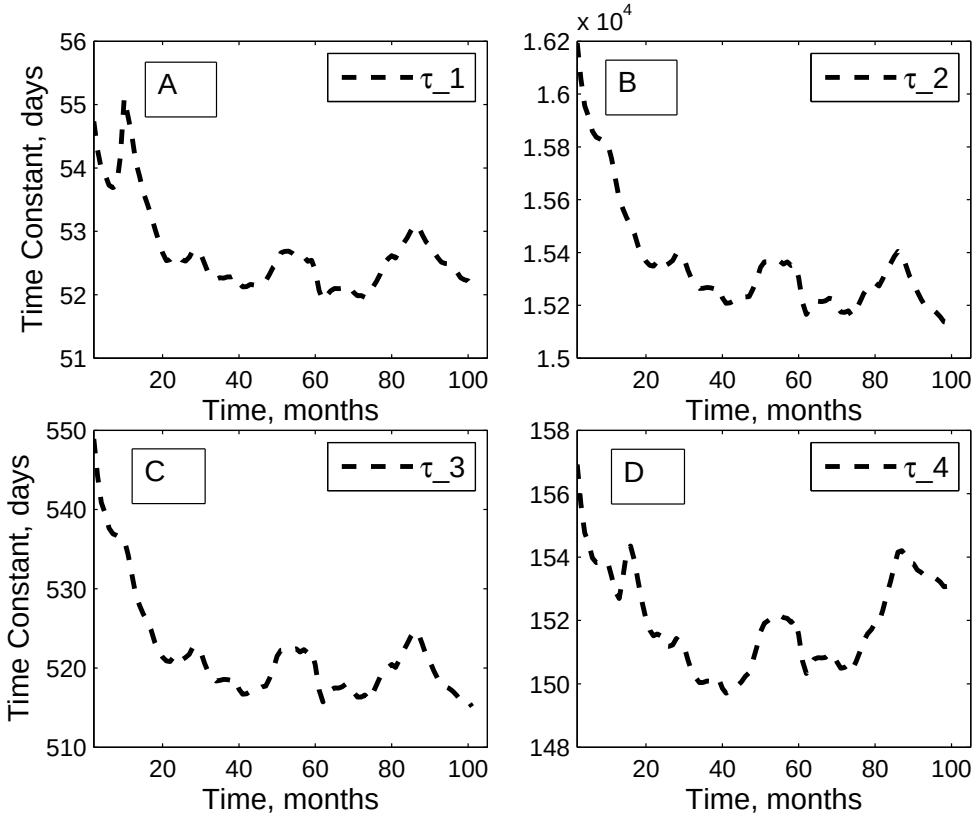

Figure 6.22: Comparison between calculated and estimated τ values for Case 3

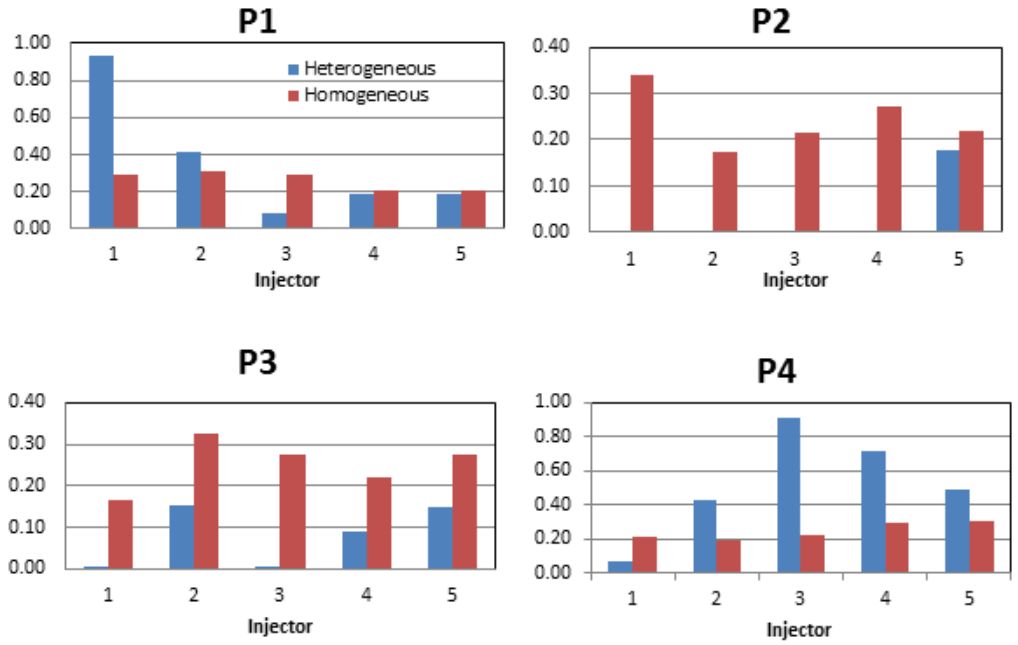

Figure 6.23: Comparison between calculated and estimated τ values for Case 3

exists (as in the high permeability channel connecting I1 and P1), there is a greater increase in the gains as well as a reduction in the time constant. These two occurrences go hand-in-hand as the reduction in response time for P1 is due to a higher share of hot water from I1 at steady state. The increase in gains and simultaneous decrease in time constant is observed to a much lesser extent for the high permeability streak between I3 and P4, suggesting an impact of the lower permeability contrast between the reservoir matrix and the I3-P4 permeability streak.

6.3.5 Validation of the Linearized Coupled Capacitance Resistance Model (LCCRM)

The LCCRM was validated for a simple 1D, single producer reservoir using the same synthetic data as in Case 1 (see Section 6.3.4.1 above). The production/injection data was used to estimate the value of the model parameters and then compared to those calculated using simulation inputs.

Model was rewritten as follows:

$$Q_j = \frac{a_2 s^2 + a_1 s + a_0}{b_3 s^3 + b_2 s^2 + b_1 s + b_0} \sum_i f_{ij} I_i + \frac{c_1 s + c_0}{b_3 s^3 + b_2 s^2 + b_1 s + b_0} \sum_i h_{ij} T_{inj,i} \tag{6.48}$$

where:

$$a_0 = \; k_5 k_6 k_9 - k_5 k_7 k_{10} + k_1 k_6 k_{11} - k_4 k_7 k_{11} \tag{6.49}$$

$$a_1 = \ k_9k_5 + k_9k_6 - k_7k_{10} + k_1k_{11} \tag{6.50}$$

$$a_2 = \ k_9 \tag{6.51}$$

$$b_0 = \ k_5k_6k_9 - k_5k_8k_{10} + k_3k_6k_{11} + k_4k_8k_{11} \tag{6.52}$$

$$b_1 = \ k_5k_6 + k_5k_9 + k_9k_6 - k_8k_{10} + k_3k_{11} \tag{6.53}$$

$$b_2 = \ k_5 + k_6 + k_9 \tag{6.54}$$

$$b_3 = \ 1 \tag{6.55}$$

$$c_0 = \ k_2k_{11}k_6 \tag{6.56}$$

$$c_1 = \ k_2k_{11} \tag{6.57}$$

This transfer function model was estimated in MATLAB using the *tfest* function. Initial parameter estimates based on steady state production response were provided. Additionally, non-negativity constraints was imposed

on some of the transfer function coefficients (such as a_2) because of their physical meaning.

Figure 6.24 presents results of production rate history-matching using the LCCRM. A superior match was observed for the LCCRM relative to the TCCRM. This result is intuitive. Because the LCCRM is a third order model (with second order numerator dynamics), it is more capable of modeling higher order behavior relative to the first-order TCCRM. However, this increased accuracy comes at a cost. The LCCRM is not as simple as the LCCRM and a derivation of the time domain representation for this model is not as straightforward. The problem of complexity may be overcome through the application of model reduction techniques such as the continued fraction expansion method. Simplification of this model while retaining its accuracy would expand the applicability of this model even further.

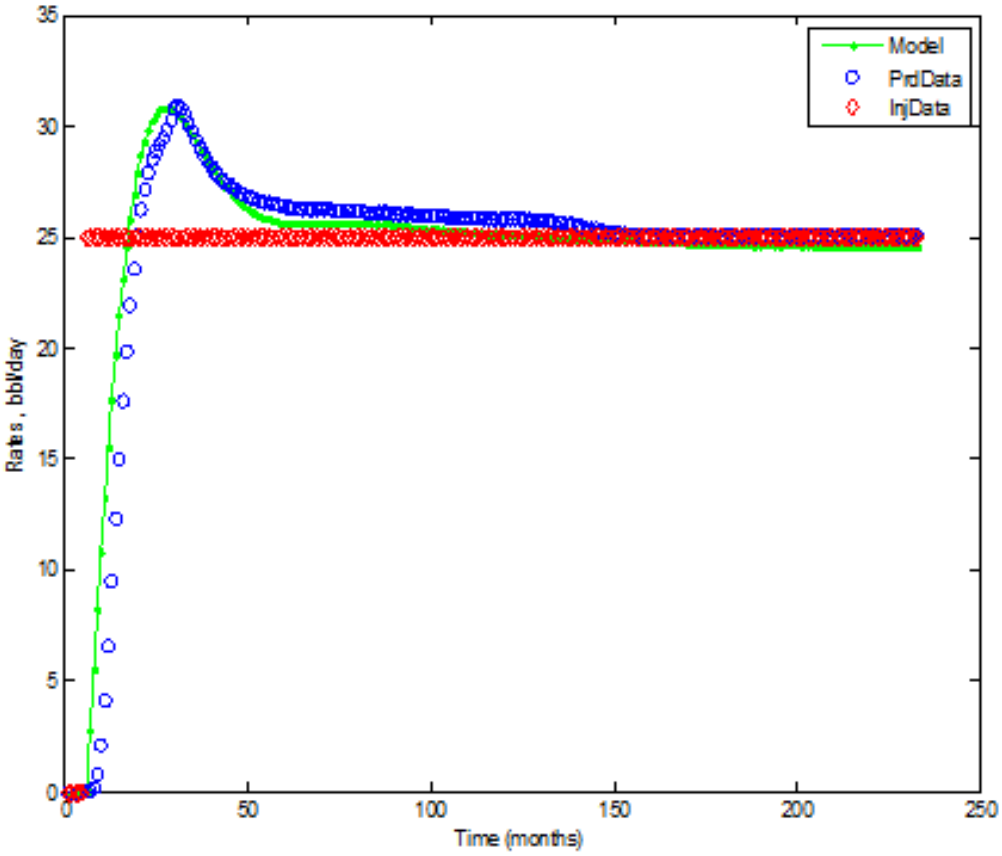

Figure 6.24: Graphical comparison of LCCRM prediction with simulation

SIMULATION DATA	
Oil viscosity	25 @ T=100°F
	0.5 @ T=200°F
Oil density	61.29 lb/ft^3
Oil specific heat capacity	0.5 btu/lb·°F
Water viscosity	0.5 cp
Water density	62.69 lb/ft^3
Water specific heat capacity	1.077 btu/lb·°F
Fluid conductivities	0
Oil compressibility	1×10^{-5} psi^{-1}
Water compressibility	1×10^{-6} psi^{-1}
Rock compressibility	1×10^{-6} psi^{-1}
Volumetric heat capacity	35 btu/ft^3·°F
RESERVOIR CONDITIONS	
Grid dimensions	1000×1×1
Block size (in i,j,k directions)	10 ft
Permeability (in i,j,k directions)	1000
Porosity	0.3
Initial reservoir temperature	100 °F
Initial pressure	100 psi
Initial oil saturation	0.99
Initial water saturation	0.01
Simulation time period	1/1/2000 - 1/1/2020
Injectant	HOT WATER
Injection temperature	200°F
Producer BHP	100 psi

Table 6.4: Simulation Input Data

RESERVOIR/FLUID CONDITIONS (ALL IN FIELD UNITS)	
Grid dimensions	33×33×1
Block size (in i and j directions)	80 ft
Block size (in k direction)	65 ft
Permeability	5 md
Initial oil saturation	0.46
Initial water saturation	0.54
Simulation time period	1/1/2000 - 5/1/2008

Table 6.5: Additional Simulation Inputs for Case 2

	I1	I2	I3	I4	I5
P1	0.286	0.309	0.288	0.208	0.204
P2	0.341	0.174	0.216	0.272	0.200
P3	0.167	0.327	0.276	0.200	0.275
P4	0.206	0.190	0.219	0.297	0.300

Table 6.6: Interwell Connectivity Estimates for Case 2

	I1	I2	I3	I4	I5
P1	0.936	0.415	0.086	0.191	0.186
P2	0.001	0.001	0.001	0.001	0.178
P3	0.001	0.155	0.001	0.089	0.149
P4	0.06	0.429	0.912	0.719	0.487

Table 6.7: Interwell Connectivity Estimates for Case 3

Chapter 7

Conclusions

7.1 Summary of research contributions

The Capacitance Resistance Model (CRM) is a reduced-order, input-output model that characterizes reservoirs using production/injection and BHP fluctuations. The model was primarily developed for waterflooding (secondary recovery) operations and has since been successfully applied to primary recovery and other EOR process. This research focused on improving CRM capabilities for characterization of waterflooded reservoirs as well as extending the CRM technology to thermal stimulation projects. Below is a summary of the key technical contributions from this research:

- **Investigation of noise impact on CRM/ICRM performance:** Because of the data centric nature of the CRM technology, the importance of data quality cannot be overemphasized. This research investigated the impact of noise on the performance of the CRM and its linear counterpart, ICRM. Because of their difference in structure, the results showed that the two models exhibit different levels of noise tolerance. Production noise was observed to have more impact on ICRM parameters estimates relative to CRM estimates. Specifically, production data with SNR levels

below 1000 showed inaccurate parameter, more so for the ICRM than for the CRM. Minimal influence of injection data noise on CRM and ICRM parameter estimates was observed because of the models' structure as low pass filters.

The observations indicate a need for careful model selection depending on the measured/perceived level of noise in the data. For datasets with SNR levels above 1000, the results support a choice of ICRM over CRM because ICRM, being linear in terms of parameters, requires less computational effort to achieve results of better or comparable quality. For datasets with noise level below 100, CRM, which is less sensitive to noise accumulation relative to the ICRM, seems to be a better choice.

- **Denoising of production data for CRM parameter estimation:** The need to denoise production data becomes more apparent particularly after the impact of noise on model performance is demonstrated. In this work, three noise removal strategies (Savitsky-Golay, Exponentially Weighted Moving Average, and Wavelet filters) were implemented and analyzed. Comparative analysis of the denoising strategies showed that the Savitsky-Golay (SG) filter, because of its favorable frequency domain characteristics, generally performs better relative to the other filters.

  Additionally, results showed that time constant estimates were more sensitive to denoising more than the gains. This difference in sensitivities emanates from how differently both parameters occur in the CRM model.

The gains occur linearly while the time constants occur exponentially. Sensitivity analysis was conducted for each of the denoising strategies to determine the preferential suitability of each strategy under different noise conditions. The results provide useful additions to the engineer/practitioner's toolkit for treating noise in data.

- **Implementation of a bootstrapping algorithm for CRM confidence intermal estimation:** Confidence interval estimation for CRM parameters is challenging because of the nonlinear nature of the model. This work introduced bootstrapping as a viable way to estimate confidence intervals for CRM parameter estimates. The bootstrapping routine introduced here obviates the need (and inherent inaccuraccies) associated with the current method of calculating confidence intervals for CRM gains and makes quantifying the uncertainty in time constant estimates fast and easy.

- **Design of injection rates for optimal parameter estimation:** Because the CRM is an input-output model, characterization with this technology is only as good as the data used. This research effort focused on designing injection rate profiles, using design of experiment (DOE) concepts, to optimally perturb a reservoir in a way that yields the most accurate parameter estimates.

  Results showed that designed inputs yielded more accurate estimates relative to unoptimized pseudo-random binary sequence (PRBS) signals.

Because injection design through PCA optimization involved redistribution of signal power to the more pertinent frequencies, R^2 values for the optimized injection rates were consistently higher than for unoptimized optimized PRBS signals. Validation of the PCA design method presented in this work showed the usefulness of properly designed injection rates when accurate parameter estimation is desired.

- **Extension of the CRM technology to thermal recovery projects:** The CRM is particularly attractive for characterization of thermal (specifically hot waterflooding) projects because of its relative speed, no reliance on geological data, and applicability to reservoirs with significant number of wells. A thermal variant of the CRM technology would provide a useful reservoir management and optimization tool that is simple and fast to complement numerical reservoir simulators.

  To develop CRM for hot waterflooded reservoirs, the following steps were taken:

  1. Relaxation of the isothermal assumption in the current CRM. This was to accommodate the evolution of model parameters with reservoir heating and necessitated the development/validation of an energy balance model to track reservoir temperature changes due to hot fluid injection.
  2. Evolution of model parameters using temperature dynamics. Because the CRM time constants depend on viscosity, which is a

strong function of temperature, modeling of the temperature-viscosity relationship was conducted for subsequent use in the updating of CRM time constants.

3. Model validation. The energy balance model developed in this work. The thermally coupled CRM and the linearized coupled CRM, were validated via numerical simulation in CMG STARS. Both models showed good agreement with simulated data, indicating the applicability of the CRM modeling approach to hot waterflooded reservoirs.

7.2 Recommendation for future work

Various aspects of the CRM technology were studied. The following are recommendations for future work:

- Research on optimizing/improving CRM implementation in the presence of noise:

    1. **Determination of noise level estimation strategies for production/injection signals prior to cleaning and/or CRM (ICRM) application.** This work has demonstrated that when significant noise is present, parameter estimation using both models is negatively affected. We have also shown that data cleaning, while helpful for very noisy data, can actually be detrimental when

noise levels are very low. Thus, development of noise level estimation techniques would help practitioners make an informed decision as to when data cleaning may be needful.

2. **Simultaneous noise cleaning and outlier removal from production and injection data.** This work has shown that denoising prior to CRM application is beneficial for accurate parameter estimation. Also, previous work, particularly by Weber [68], has also shown the usefulness of outlier removal for CRM application. Given the demonstrated value of these two aspects of data cleaning, we recommend the development of a single routine in which both processes are unified. That would provide practitioners with a one stop tool for effective data preprocessing prior to CRM application.

3. **Investigation of the influence and/or removal noise from bottomhole pressure data.** This work focused on the impact and removal of noise from production rate data. Because BHP data is also necessary when fluctuations in the BHP are present, the impact of noise in BHP measurements as well as viable ways of reducing adverse noise impacts should be investigated. Additionally, comparative analysis of the impact of BHP noise relative to that in the production rate data would give insights as to where accurate measurements are more pertinent. These insights may provide useful guidance when preferential placement of measurement devices is being considered.

4. **Denoising for ICRM.** Chapter 4 presented denoising techniques for production data prior to CRM application. The results demonstrated the usefulness of data cleaning in obtaining superior CRM parameter estimates. Common sense suggests that denoising should lead to improved parameter estimates for the ICRM. Confirmation of this hypothesis is recommended.

5. **Design and optimization of injection rates for joint optimality in terms of parameter estimation and economics.** This work has shown that design of injection sequences for optimal parameter estimation is both possible and useful. However, because the objective functions are formulated differently, it is not clear that an injection sequence optimal for parameter estimation will also be optimal economically. Understanding the relationship between these two objectives will provide insight into the potential economic cost of injection rate optimization for parameter estimation. Additionally, investigating the possibility of designing rates that are optimal both economically and in terms of parameter estimation is worthwhile.

- Research on improving the thermal CRM variants:

    1. **Sensitivity analysis.** Sensitivity analysis on the models introduced in this work would be useful deepening understanding of their applicability and capabilities. Key parameters such as viscos-

ity, initial oil saturation, volumetric heat capacity of the reservoir rock, and oil/water relative permeability curves should be varied to understand their influence on the performance of both model.

2. **Field application of the Thermal Coupled CRM (TCCRM) and Linearized Coupled CRM (LCCRM).** This work has demonstrated the applicability of TCCRM and LCCRM for heavy oil reservoirs. Synthetic injection/production histories were used to validate the models, the results of which showed good agreement. Further testing of the models using field data is recommended to build upon the experience of using synthetic data.

3. **Assessment of validity and impact of assumption of equality between average reservoir temperature and outlet well temperature.** In developing that temperature model used for TCCRM and LCCRM, we assumed negligible difference between the average reservoir temperature and the outlet well temperature. This assumption, which assumes perfect mixing within a reservoir control volume, in part obviates the need for spatial modeling of heat transfer, greatly simplifying the model. In field operations, where flowrates and well spacing parameters may vary substantially, this assumption could be a limitation. Thus, we recommend an assessment of the impact of the above assumption on the performance of the models when field data is used.

4. **Development of oil production rate/fractional flow model**

applicable for Thermal CRM. This work has proposed and validated a model for the total fluid production in a hot waterflooding process. The model, however, does not provide a means for modeling oil production rate itself which is of significant importance during oil exploration. For the isothermal CRM, estimation of the oil production rate is typically done using a fractional flow model. However, this approach has been found limited by previous researchers [9]. Moreover, the more complicated nature of the hot waterflooding, caused by an additional interacting thermal process, necessitates a model reflective of this salient feature. Thus, development of such fractional flow model to complement the thermal CRM models presented in this work is recommended.

5. **Investigate the possibility of incorporating another viscosity-temperature model**. In this work, the Andrade Equation [5] was used to model the evolution of viscosity due to reservoir heating. This simplicity of this model and its independence from specific fluid properties made it an excellent fit for the CRM modeling approach. But the simplicity came with a tradeoff in accuracy. Thus, improvements to the present viscosity model and/or research into the applicability of other viscosity models would be useful in increasing the thermal CRM's history-matching capability.

6. **Extension of the EBTM modeling approach to other thermal recovery processes.** This work has demonstrated that a tank

formulation of the energy balance for a hot waterflood is useful for obtaining average reservoir temperature. Extending this modeling approach to other thermal EOR processes such as SAGD, steamflooding, and in-situ combustion process is recommended.

7. **Extending the linearized thermal CRM (LCCRM) to multi-well characterization.** The LCCRM as developed in this work showed superior history-matching capabilities for a 1D, single producer reservoir. Applying this model to reservoirs with multiple producers is therefore recommended. Such an extension may entail reduction of model order via methods such as continued fraction expansion.

8. **Development of thermal CRM variants for smaller drainage volumes.** This dissertation developed the thermal CRM models for a producer-based drainage volume. It is recommended to develop the models based on smaller drainage volumes between a particular producer-injector pair. The increase in granularity has the potential of increasing accuracy. Additionally, more useful information may be obtained due to the increase in detail.

Appendices

Appendix A

Additional plots for Chapters 3

Appendix A presents supplementary plots for Chapter 3. Production rate plots before and after noise addition are included for SNR levels from 10^5 to 10^2. Additionally, power spectrums obtained from FFT decomposition of production rate data corresponding to SNR levels 10^5 to 10^2 are presented. Plots presented in the main body of the dissertation are omitted here to avoid duplication.

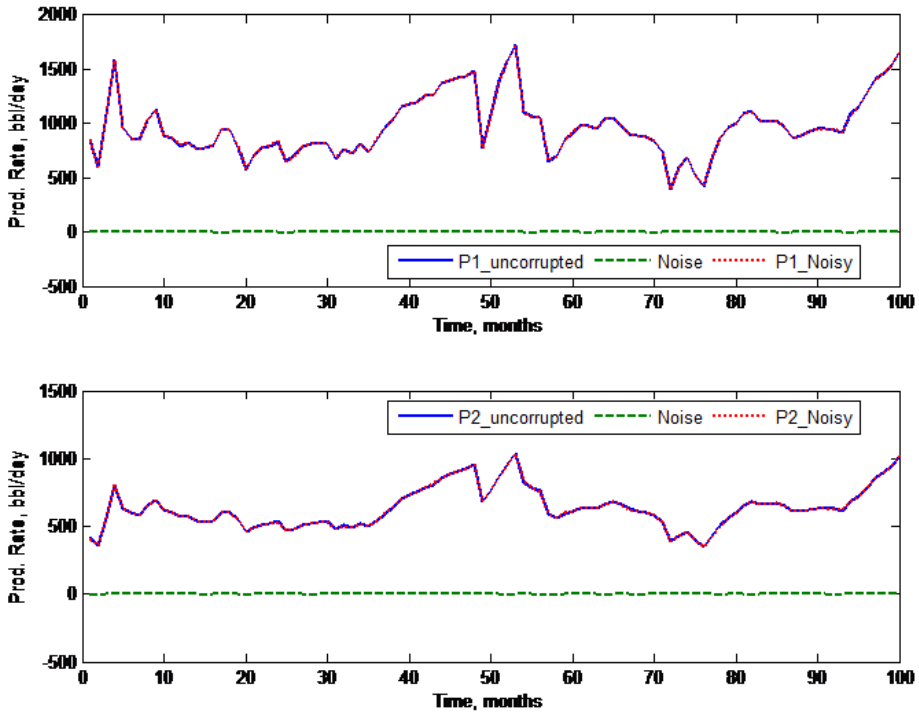

Figure A.1: Production rate profiles before and after noise addition for SNR $= 10^5$

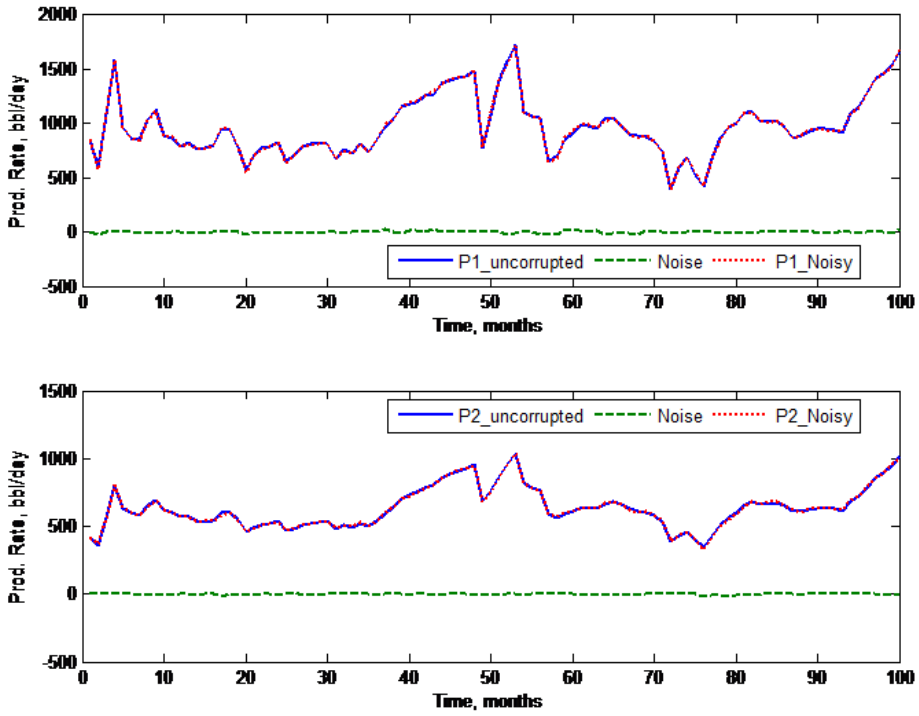

Figure A.2: Production rate profiles before and after noise addition for SNR $= 10^4$

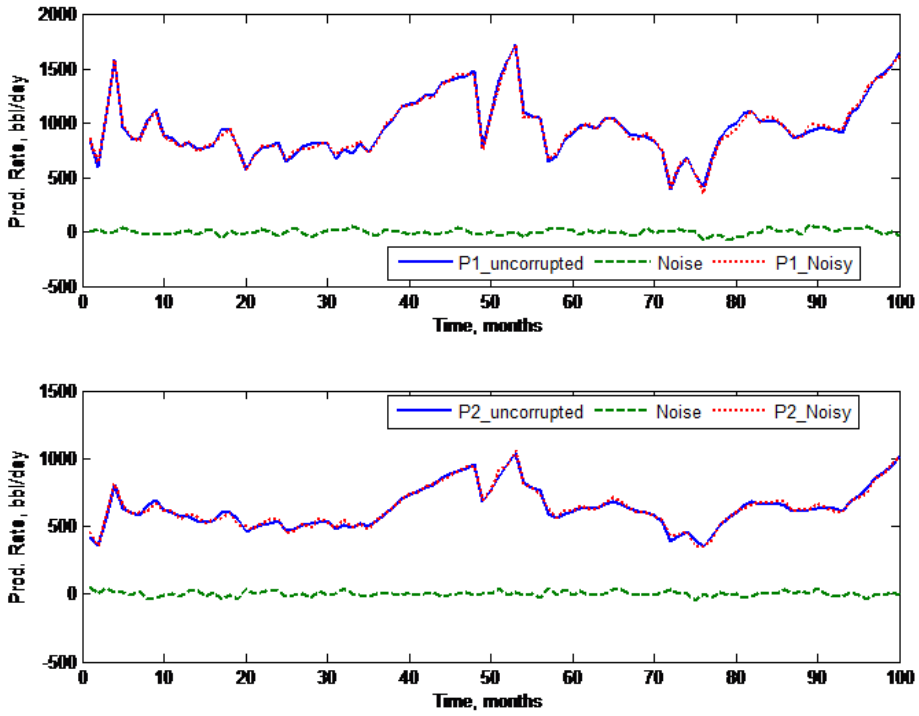

Figure A.3: Production rate profiles before and after noise addition for SNR $= 10^3$

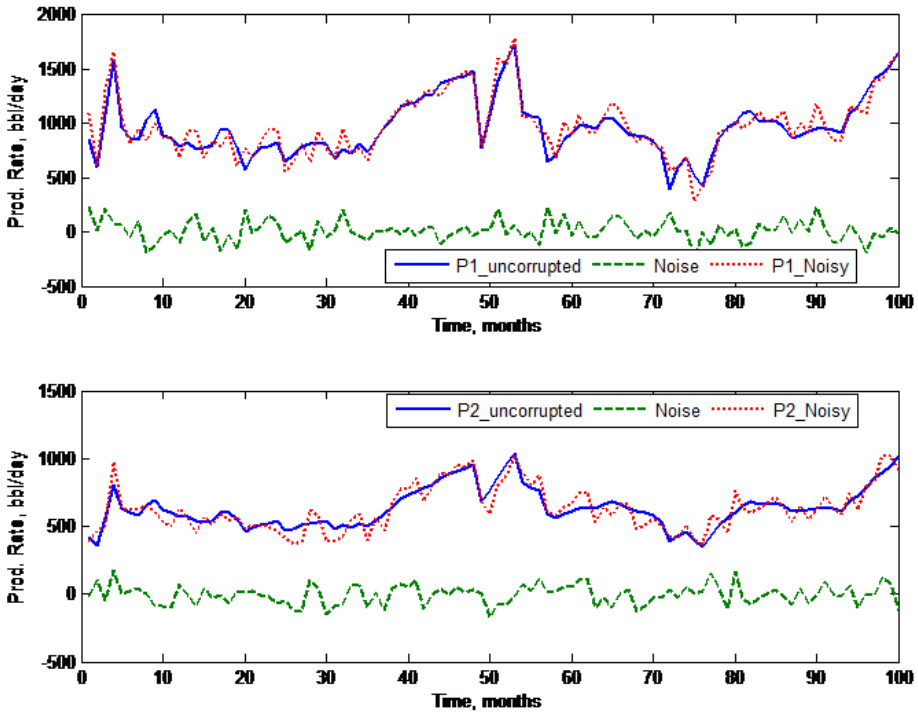

Figure A.4: Production rate profiles before and after noise addition for SNR $= 10^2$

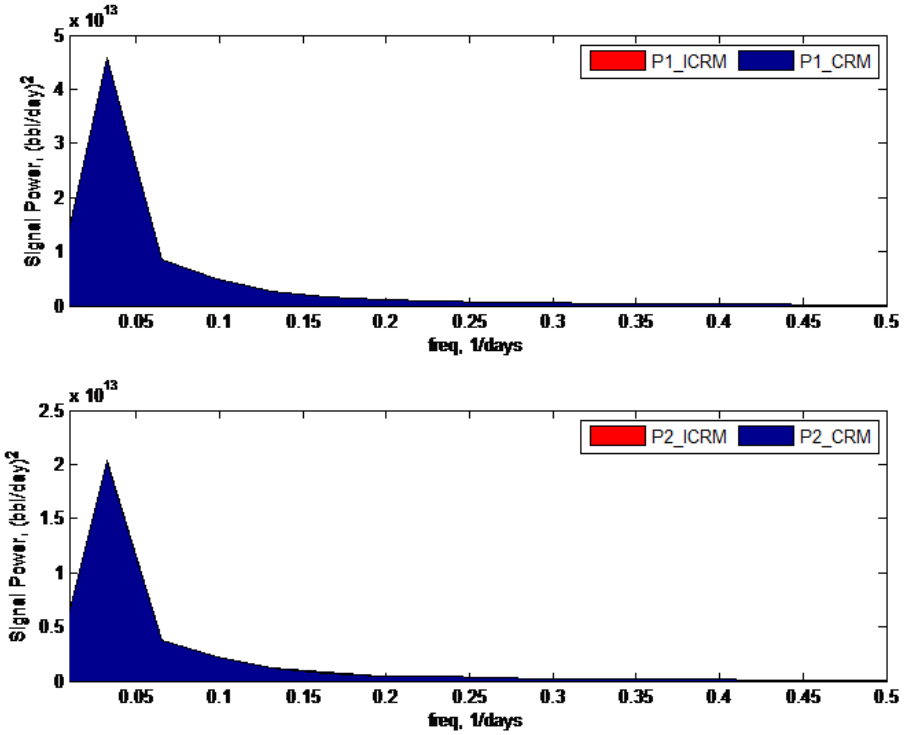

Figure A.5: Power Spectrum for Production Signals at SNR = 10^5

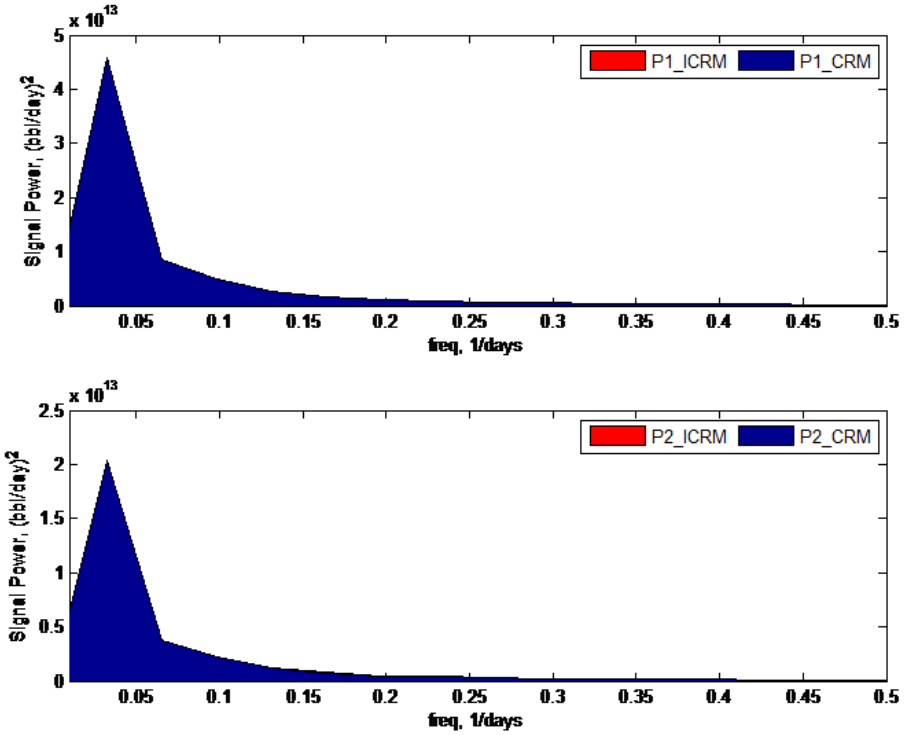

Figure A.6: Power Spectrum for Production Signals at SNR = 10^4

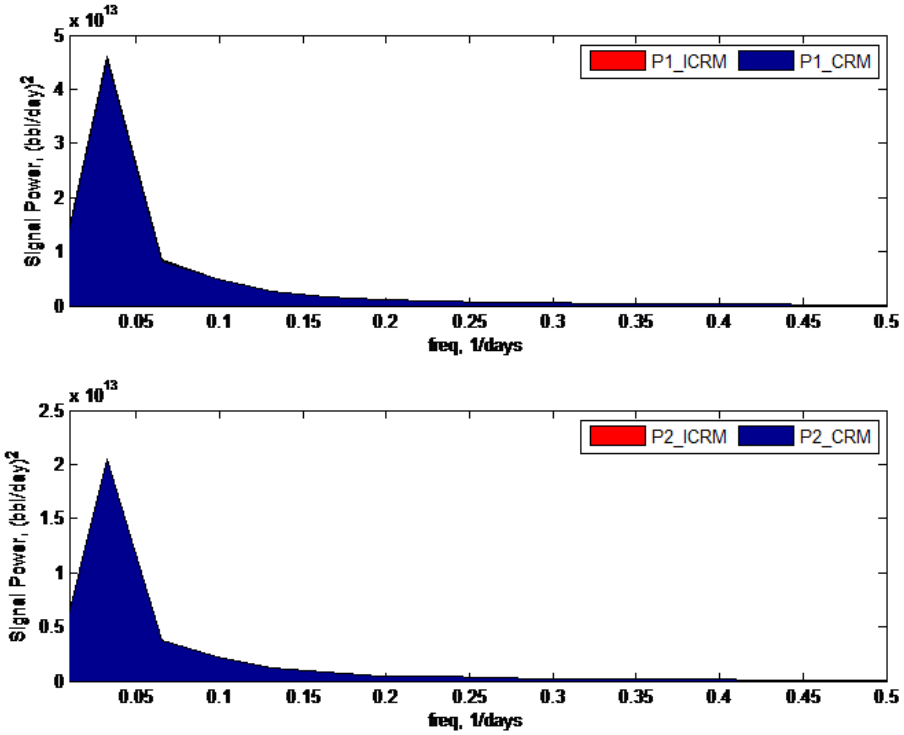

Figure A.7: Power Spectrum for Production Signals at SNR = 10^3

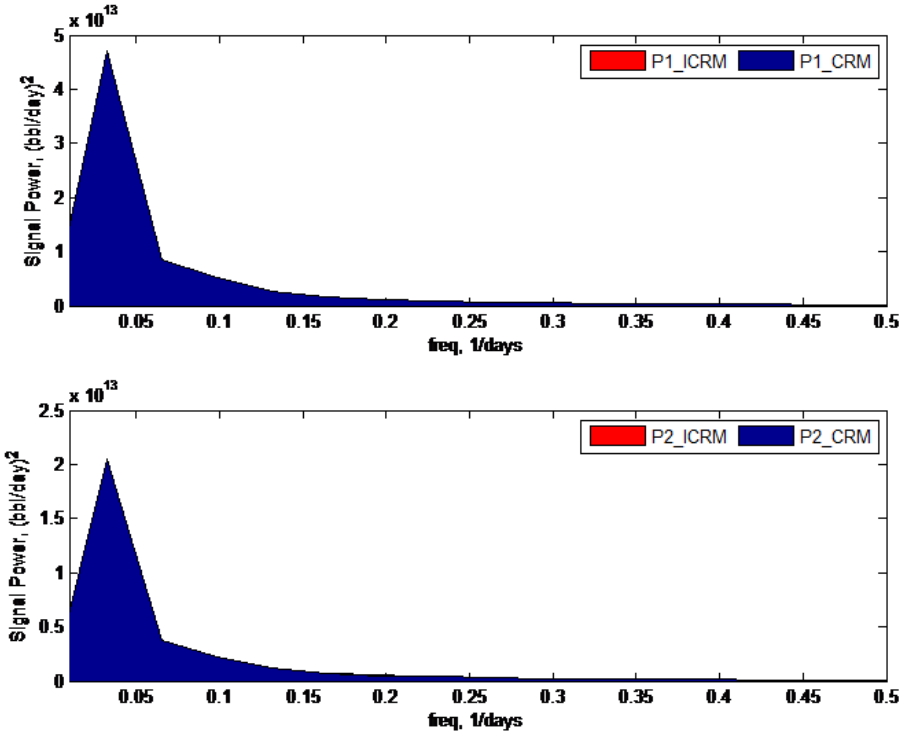

Figure A.8: Power Spectrum for Production Signals at SNR = 10^2

Appendix B

Additional plots for Chapter 4

In this Appendix, supplementary plots for Chapter 4 are included. Plots presented in the main body of the dissertation are omitted here to avoid duplication. Production rate plots before and after noise addition are included for SNR levels from 100 to 20. Additionally, denoising results from each of these SNR levels are presented. Production data denoised using the three different filters are compared to original, (i.e., not noisy) data. Finally, parameter estimates from denoised and noisy datasets are compared through a bar chart.

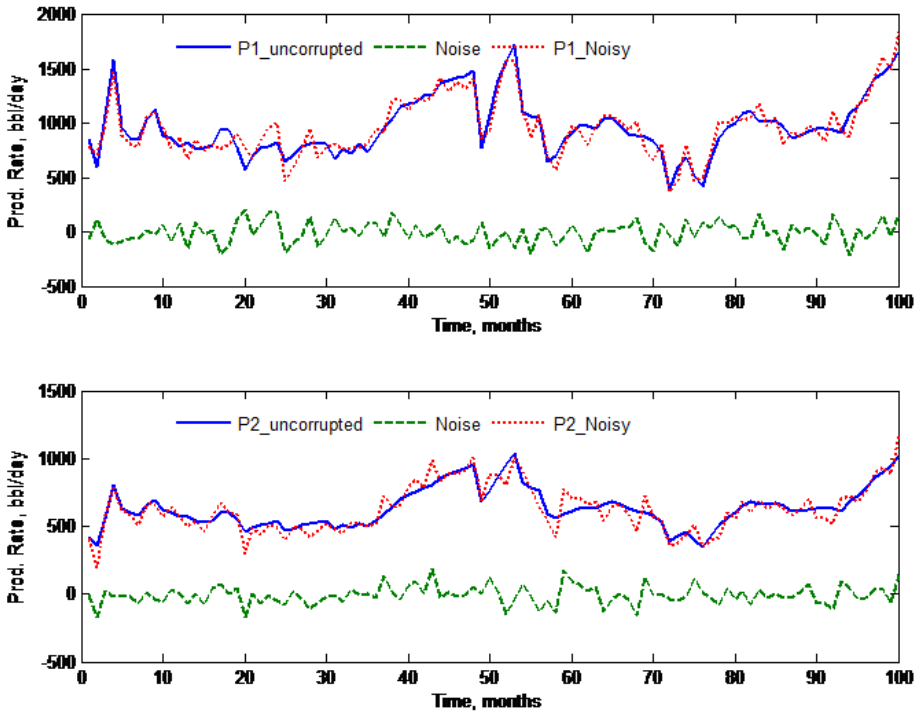

Figure B.1: Production rate profiles before and after noise addition for SNR = 100

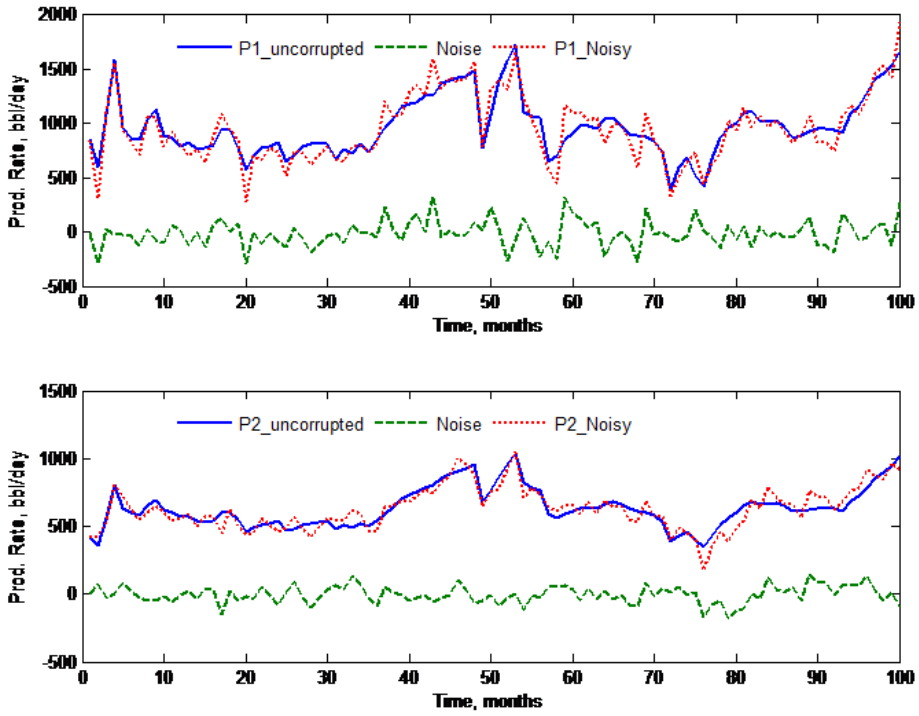

Figure B.2: Production rate profiles before and after noise addition for SNR = 75

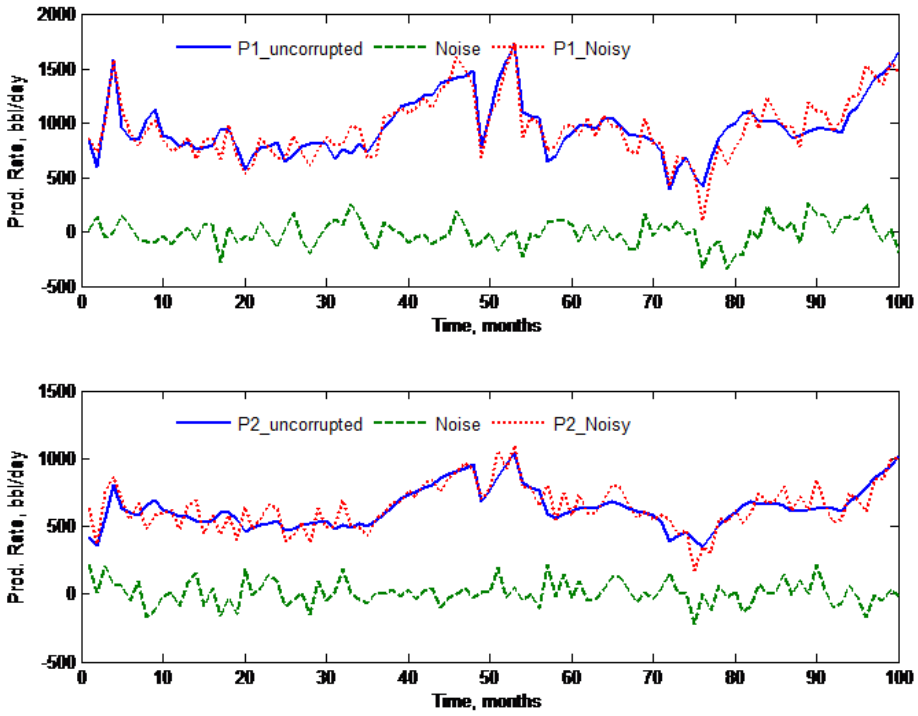

Figure B.3: Production rate profiles before and after noise addition for SNR = 50

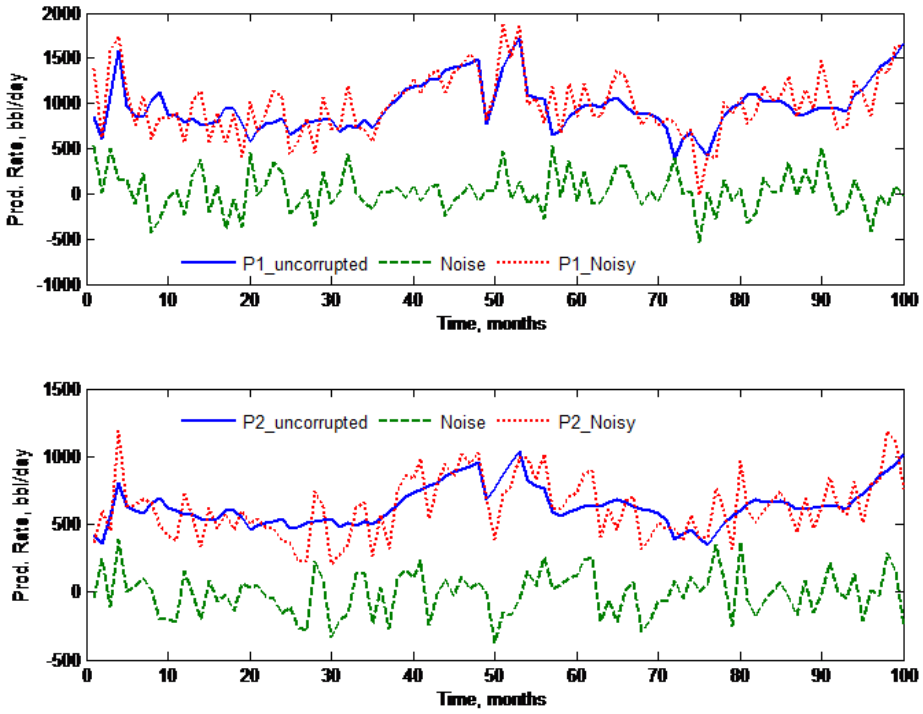

Figure B.4: Production rate profiles before and after noise addition for SNR = 20

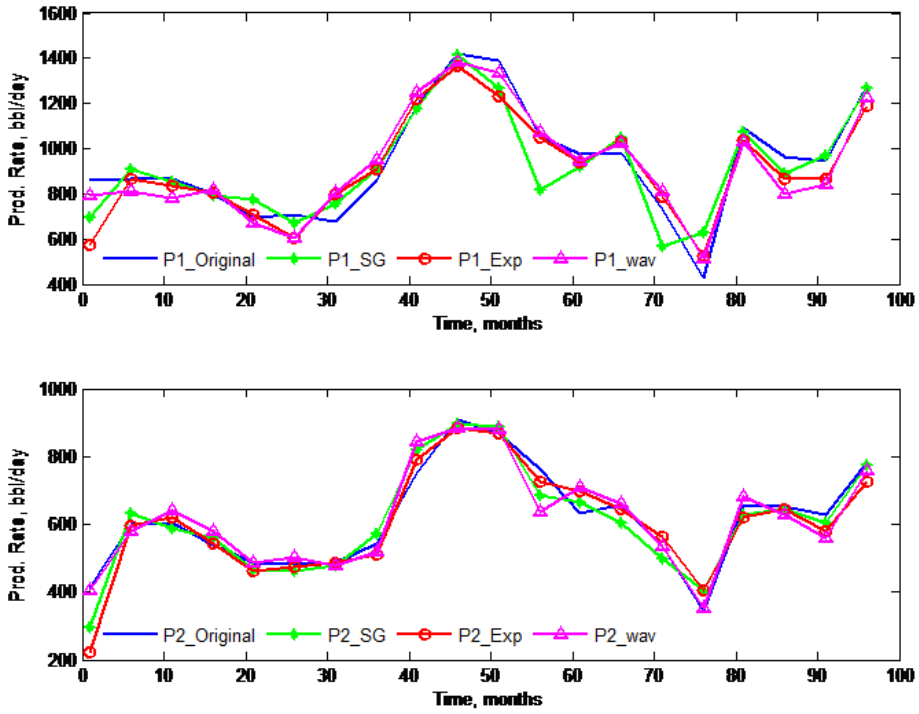

Figure B.5: Production rate profiles of both producers before and after denoising for SNR = 100

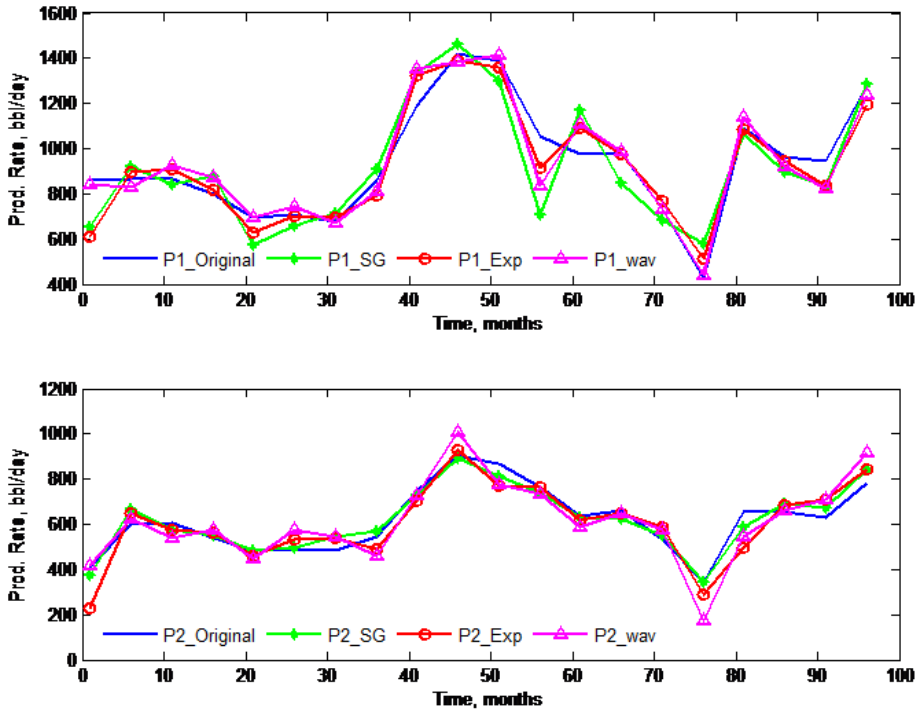

Figure B.6: Production rate profiles of both producers before and after denoising for SNR = 75

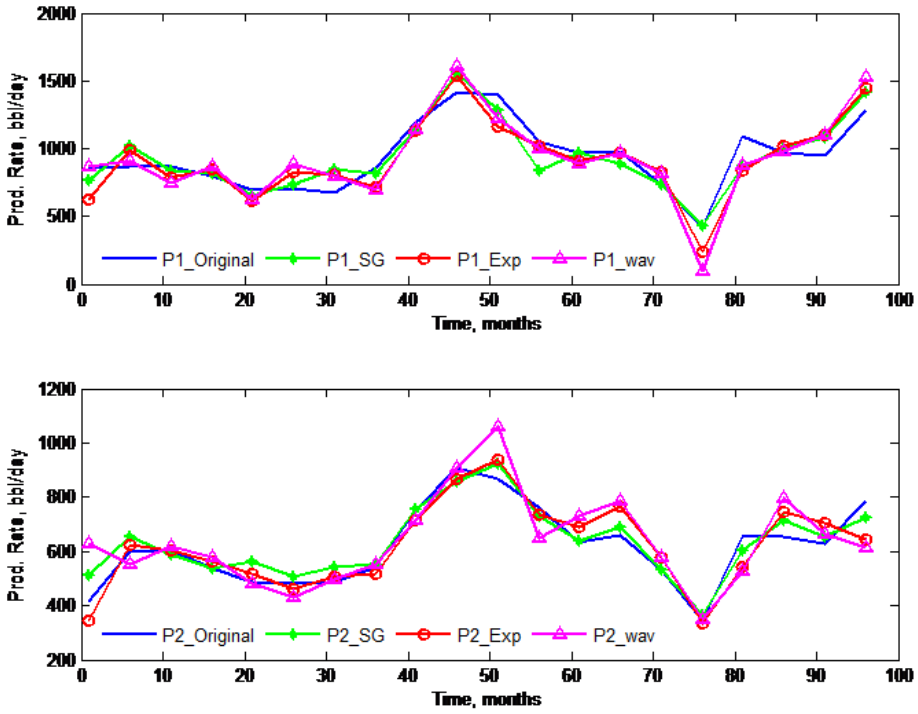

Figure B.7: Production rate profiles of both producers before and after denoising for SNR = 50

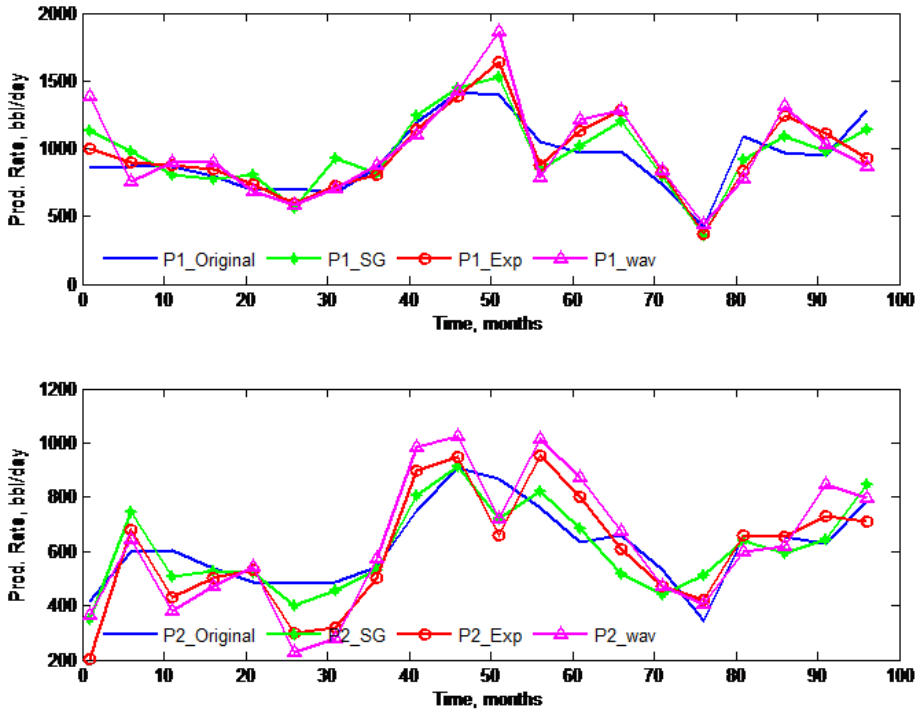

Figure B.8: Production rate profiles of both producers before and after denoising for SNR = 20

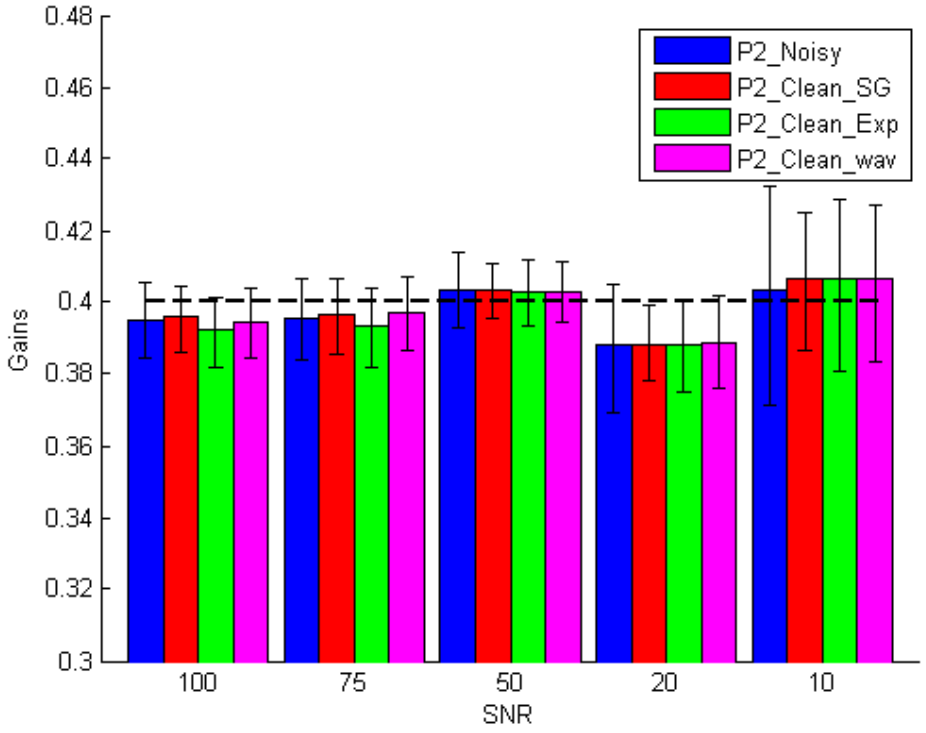

Figure B.9: CRM gain estimates before and after denoising for producer P2

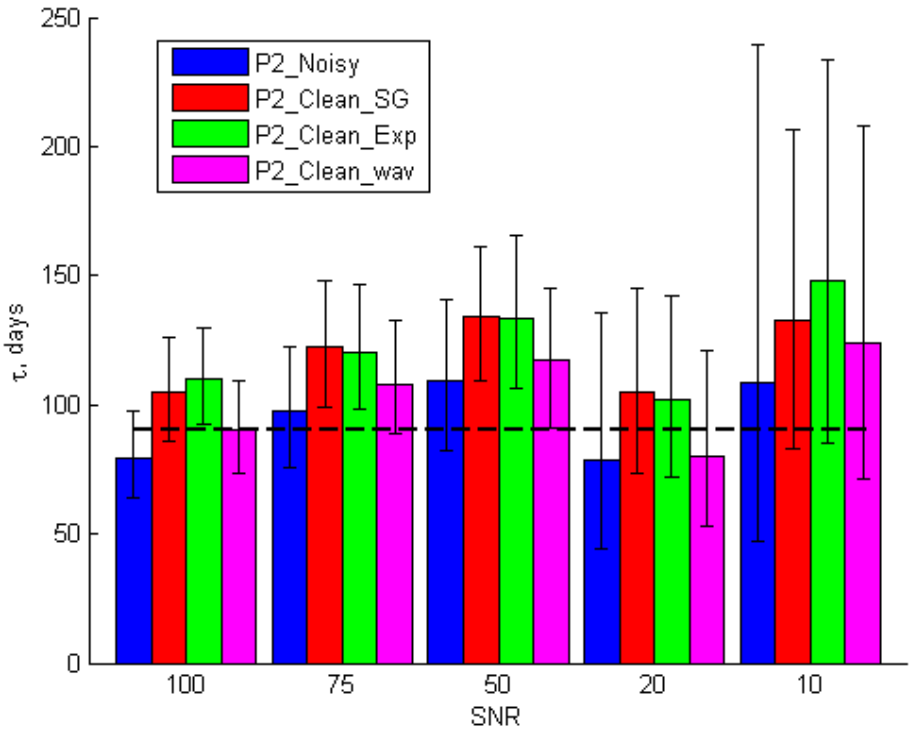

Figure B.10: CRM τ estimates before and after denoising for producer P2

Glossary A. List of Abbreviations

1D one dimensional

2D two dimensional

API American Petroleum Institute

BHP bottomhole pressure

CCRM coupled CRM

CMG computer modeling group

CRM capacitance resistance model

CRMIP injector-producer based CRM

CRMP producer based CRM

CRMT tank model CRM

CV control volume

DFT discrete Fourier transform

DOE design of experiments

EBTM energy balance tank model

EOR enhanced oil recovery

EWMA exponentially weighted moving average

FFT fast Fourier Ttansform

FIM Fisher information matrix

FIR finite impulse response

ICRM integrated capcitance resistance model

LCCRM linearized coupled CRM

ltCRMP linearly transformed producer based CRM

LVIR linear variation of injection rates

MVLR multivariate linear regression

ODE ordinary differential equation

OOIP original oil in place

PC principal component

PCA principal component analysis

PRBS pseudorandom binary sequence

PV pore volume of control volume around producer

RC resistance-capacitance

RO reduced order

SAGD steam assisted gravity drainage

SG Savitsky-Golay

SNR signal-to-noise ratio

SVD singular value decomposition

SVIR stepwise variation of injection rates

TCCRM thermally coupled CRM

USGS United States Geological Survey

Glossary B. Nomenclature

P_{wf} well bottom hole pressure (psi)

I injection rate ($bbl \cdot day^{-1}$)

N_P cumulative production (bbl)

CWI cumulative water injected (bbl)

A drainage area (ft^2)

c_f pore compressibility (psi^{-1})

c_o oil compressibility (psi^{-1})

c_t total compressibility (psi^{-1})

c_w water compressibility (psi^{-1})

$\boldsymbol{t}_D$ dimensionless time

$\bar{T}_D$ dimensional average temperature in the control volume

V_P drainage volume (ft^3)

V_b drainage volume (ft^3)

n_1 exponent of water relative permeability

n_2 exponent of oil relative permeability

f_o oil fractional flow

f_w water fractional flow

f_{ij} interwell connectivity (or gain) between injector i and producer j

h thickness of control volume (ft)

i injection rate ($bbl \cdot day^{-1}$)

J_t total productivity index ($bbl \cdot day^{-1} \cdot psi^{-1}$)

T_0 initial temperature in the control volume

N_{inj} number of injectors

T_{inj} temperature of injected fluid

S_{wr} irresidual water saturation

K_{val} Koval factor

N_{prd} number of producers

q_o oil production rate ($bbl \cdot day^{-1}$)

S_o oil saturation

$\bar{S}_o$ average oil saturation in the control volume

S_{o2} outlet oil saturation

$\boldsymbol{k}$ absolute permeability (darcy)

k_{ro} oil relative permeability

k_{ro}^0 endpoint oil relative permeability

k_{rw} water relative permeability

k_{rw}^0 endpoint water relative permeability

$\bar{P}$ average pressure in control volume (psi)

R^2 coefficient of fit (determination)

S_{or} residual oil saturation

C_A shape factor

$\bar{T}$ average temperature in the control volume

t time (day)

M_t total mobility ratio (cp^{-1})

q_t total production rate ($bbl \cdot day^{-1}$)

A_v pre-exponential constant for Andrade equation (cp)

B_v exponential constant for Andrade equation ($^\circ F$)

q_w water production rate ($bbl \cdot day^{-1}$)

S_w water saturation

$\bar{S}_w$ average water saturation in the control volume

r_w well radius (ft)

Greek letters

γ Euler constant

ϕ porosity

τ time constant (day)

θ TCCRM parameter for time constant estimation ($day \cdot cp^{-1}$)

μ_o oil viscosity (cp)

μ_w water viscosity (cp)

Subscripts and superscripts

cal subscript denoting calculated value

k superscript denoting discrete time index

i subscript denoting injector

obs subscript denoting observed value

o subscript denoting oil

j subscript denoting producer

$\boldsymbol{t}$ subscript denoting total

$\boldsymbol{w}$ subscript denoting water

Bibliography

[1] Tayeb A Tafti, Iraj Ershaghi, Amin Rezapour, Antonio Ortega, et al. Injection scheduling design for reduced order waterflood modeling. In *SPE Western Regional & AAPG Pacific Section Meeting 2013 Joint Technical Conference*. Society of Petroleum Engineers, 2013.

[2] Mohammad Ahmadi. Enhanced modeling of thermal oil recovery processes using moving mesh strategy. In *International Thermal Operations and Heavy Oil Symposium*. Society of Petroleum Engineers, 2008.

[3] Alejandro Albertoni, Larry W Lake, et al. Inferring interwell connectivity only from well-rate fluctuations in waterfloods. *SPE Reservoir Evaluation & Engineering*, 6(01):6–16, 2003.

[4] H Alboudwarej, J Felix, R Badry, et al. Highlighting heavy oil, oilfield review. *Schlumberger, Summer*, 2006.

[5] EN da C Andrade. The viscosity of liquids. *Nature*, 125:309–310, 1930.

[6] Elham Ashoori, Thom van der Heijden, William Rossen, et al. Fractional-flow theory of foam displacements with oil. *SPE Journal*, 15(02):260–273, 2010.

[7] Kjartan Berg, Janardhan Davalath, et al. Field applications of idun production measurement system. In *Offshore Technology Conference*. Offshore Technology Conference, 2002.

[8] WA Bruce et al. An electrical device for analyzing oil-reservoir behavior. *Transactions of the AIME*, 151(01):112–124, 1943.

[9] F Cao. Development of a coupled two phase flow capacitance resistance model. *PhD dissertation, The University of Texas at Austin, Austin, Texas, USA*, 2014.

[10] Fei Cao. A new method of data quality control in production data using the capacitance-resistance model. *Master's thesis, The University of Texas at Austin, Austin, Texas, USA*, 2011.

[11] Fei Cao, Haishan Luo, and Larry W Lake. Development of a fully coupled two-phase flow based capacitance resistance model (crm). In *SPE Improved Oil Recovery Symposium*. Society of Petroleum Engineers, 2014.

[12] James Carpenter and John Bithell. Bootstrap confidence intervals: when, which, what? a practical guide for medical statisticians. *Statistics in medicine*, 19(9):1141–1164, 2000.

[13] Chung-Shou Chen and HL Hutchinson. One-dimensional modeling of steam injection in tar sands. In *SPE Rocky Mountain Regional Meeting*. Society of Petroleum Engineers, 1983.

[14] Arthur T Corey. The interrelation between gas and oil relative permeabilities. *Producers monthly*, 19(1):38–41, 1954.

[15] M Delshad, A Bastami, P Pourafshary, et al. The use of capacitance-resistive model for estimation of fracture distribution in the hydrocarbon reservoir. In *SPE Saudi Arabia Section Technical Symposium*. Society of Petroleum Engineers, 2009.

[16] Dennis Denney et al. Downhole fiber-optic multiphase flowmeter. *Journal of petroleum technology*, 54(12):59–61, 2002.

[17] Thomas J DiCiccio and Joseph P Romano. A review of bootstrap confidence intervals. *Journal of the Royal Statistical Society. Series B (Methodological)*, pages 338–354, 1988.

[18] TA Edmondson. Effect of temperature on waterflooding. *Journal of Canadian Petroleum Technology*, 4(04):236–242, 1965.

[19] B Efron. Bootstrap methods: another look at the jackknife. *Annals of Statistics*, 7(1):1–26, 1979.

[20] Bradley Efron and Robert Tibshirani. Bootstrap methods for standard errors, confidence intervals, and other measures of statistical accuracy. *Statistical science*, pages 54–75, 1986.

[21] Bradley Efron and Robert J Tibshirani. *An introduction to the bootstrap*. CRC press, 1994.

[22] DL Flock, D Quon, MA Leal, and AR Thachuk. Modelling of a thermally stimulated oil reservoir-an evaluation of theoretical and numerical methods. *Journal of Canadian Petroleum Technology*, 6(04):136–145, 1967.

[23] Pablo Hugo Gentil. The use of multilinear regression models in patterned waterfloods: physical meaning of the regression coefficients. *Master's thesis, The university of Texas at Austin*, 2005.

[24] BS Gottfried. A mathematical model of thermal oil recovery in linear systems. *Society of Petroleum Engineers Journal*, 5(03):196–210, 1965.

[25] GJ Harmsen et al. Oil recovery by hot-water and steam injection. In *8th World Petroleum Congress*. World Petroleum Congress, 1971.

[26] David V Hinkley. Bootstrap methods. *Journal of the Royal Statistical Society. Series B (Methodological)*, pages 321–337, 1988.

[27] O Izgec and CS Kabir. Understanding reservoir connectivity in waterfloods before breakthrough. *Journal of Petroleum Science and Engineering*, 75(1):1–12, 2010.

[28] Danial Kaviani, Jerry L Jensen, and Larry W Lake. Estimation of interwell connectivity in the case of unmeasured fluctuating bottomhole pressures. *Journal of Petroleum Science and Engineering*, 90:79–95, 2012.

[29] Jong S Kim, Larry W Lake, and Thomas F Edgar. Integrated capacitance-resistance model for characterizing waterflooded reservoirs. *IFAC Proceedings Volumes*, 45(8):19–24, 2012.

[30] Jong Suk Kim. Development of linear capacitance-resistance models for characterizing waterflooded reservoirs. *Masters thesis, The University of Texas at Austin, Austin, Texas, USA*, 2011.

[31] EJ Koval et al. A method for predicting the performance of unstable miscible displacement in heterogeneous media. *Society of Petroleum Engineers Journal*, 3(02):145–154, 1963.

[32] Larry W Lake. *Enhanced oil recovery*. Old Tappan, NJ; Prentice Hall Inc., 1989.

[33] Larry W Lake, Ximing Liang, Thomas F Edgar, Ali Al-Yousef, Morteza Sayarpour, Daniel Weber, et al. Optimization of oil production based on a capacitance model of production and injection rates. In *Hydrocarbon economics and evaluation symposium*. Society of Petroleum Engineers, 2007.

[34] Larry W Lake and Walsh PM. *A generalized approach to primary hydrocarbon recovery. Handbook of petroleum exploration and production*, volume 4. Elsevier Science Limited, 2003.

[35] HA Lauwerier. The transport of heat in an oil layer caused by the injection of hot fluid. *Applied Scientific Research, Section A*, 5(2-3):145–150, 1955.

[36] A Mai and A Kantzas. Heavy oil waterflooding: Effects of flow rate and oil viscosity. *Journal of Canadian Petroleum Technology*, 48(03):42–51, 2009.

[37] Stephane Mallat. *A wavelet tour of signal processing: the sparse way*. Academic press, 2008.

[38] WL Martin et al. Results of a tertiary hot waterflood in a thin sand reservoir. *Journal of petroleum technology*, 20(07):739–750, 1968.

[39] JW Marx, RH Langenheim, et al. Reservoir heating by hot fluid injection. 1959.

[40] Raman Mehra. Optimal input signals for parameter estimation in dynamic systems–survey and new results. *IEEE Transactions on Automatic Control*, 19(6):753–768, 1974.

[41] Richard F Meyer, ED Attanasi, and Philip A Freeman. Heavy oil and natural bitumen resources in geological basins of the world. Technical report, 2007.

[42] Richard F Meyer and Emil D Attanasi. Heavy oil and natural bitumen-strategic petroleum resources. *World*, 434:650–7, 2003.

[43] L Mišković, Alireza Karimi, Dominique Bonvin, and Michel Gevers. Closed-loop identification of multivariable systems: With or without excitation of all references? *Automatica*, 44(8):2048–2056, 2008.

[44] Gustavo A Moreno and Larry W Lake. On the uncertainty of interwell connectivity estimations from the capacitance-resistance model. *Petroleum Science*, 11(2):265–271, 2014.

[45] Gustavo Ariel Moreno, Abel Garriz, et al. Injection leakage detection in mature fields using data-driven models. In *SPE Latin America and Caribbean Petroleum Engineering Conference*. Society of Petroleum Engineers, 2014.

[46] CH Neuman. A mathematical model of the steam drive process–applications. *California Reg. Meet. Soc. Pet. Eng., Ventura, Calif*, 1975.

[47] Anh Phuong Nguyen. Capacitance resistance modeling for primary recovery, waterflood and water-co flood. *PhD dissertation, The University of Texas at Austin, Austin, Texas, USA*, 2012.

[48] Anh Phuong Nguyen, Jong Suk Kim, Larry Wayne Lake, Thomas F Edgar, Byron Haynes, et al. Integrated capacitance resistive model for reservoir characterization in primary and secondary recovery. In *SPE Annual Technical Conference and Exhibition*. Society of Petroleum Engineers, 2011.

[49] SJ Orfanidis. Savitzky-golay filtering. *Introduction to Signal Processing, Englewood Cliffs, NJ*, 1996.

[50] Usman Pasarai, Norio Arihara, et al. Application of streamline method to hot water-flooding simulation for heavy oil recovery. In *SPE Asia Pacific Oil and Gas Conference and Exhibition*. Society of Petroleum Engineers, 2005.

[51] Donald W Peaceman et al. Interpretation of well-block pressures in numerical reservoir simulation with nonsquare grid blocks and anisotropic permeability. *Society of Petroleum Engineers Journal*, 23(03):531–543, 1983.

[52] Gary A Pope et al. The application of fractional flow theory to enhanced oil recovery. *Society of Petroleum Engineers Journal*, 20(03):191–205, 1980.

[53] HJ Ramey Jr et al. A current review of oil recovery by steam injection. In *7th World Petroleum Congress*. World Petroleum Congress, 1967.

[54] Abraham Savitzky and Marcel JE Golay. Smoothing and differentiation of data by simplified least squares procedures. *Analytical chemistry*, 36(8):1627–1639, 1964.

[55] Morteza Sayarpour. *Development and Application of Capacitance-resistive Models to Water/carbon Dioxide Floods*. ProQuest, 2008.

[56] Morteza Sayarpour, C Shah Kabir, Larry W Lake, et al. Field applications of capacitance-resistance models in waterfloods. *SPE reservoir evaluation & engineering*, 12(06):853–864, 2009.

[57] Morteza Sayarpour, E Zuluaga, C Shah Kabir, and Larry W Lake. The use of capacitance–resistance models for rapid estimation of waterflood performance and optimization. *Journal of Petroleum Science and Engineering*, 69(3):227–238, 2009.

[58] Ronald W Schafer. What is a savitzky-golay filter?[lecture notes]. *IEEE Signal Processing Magazine*, 28(4):111–117, 2011.

[59] Dale E Seborg, Duncan A Mellichamp, Thomas F Edgar, and Francis J Doyle III. *Process dynamics and control*. John Wiley & Sons, 2016.

[60] Amjad Shah, Robert Fishwick, Joseph Wood, Gary Leeke, Sean Rigby, and Malcolm Greaves. A review of novel techniques for heavy oil and bitumen extraction and upgrading. *Energy & Environmental Science*, 3(6):700–714, 2010.

[61] Steven W Smith et al. The scientist and engineer's guide to digital signal processing. 1997.

[62] James G Speight. *Heavy oil production processes*. Gulf Professional Publishing, 2013.

[63] AG Spillette and RL Nielsen. Two-dimensional method for predicting hot waterflood recovery behavior. *Journal of Petroleum Technology*, 20(06):627–638, 1968.

[64] Arthur G Spillette et al. Heat transfer during hot fluid injection into an oil reservoir. *Journal of Canadian Petroleum Technology*, 4(04):213–218, 1965.

[65] Qing Tao, Steven L Bryant, et al. Optimizing carbon sequestration with the capacitance/resistance model. *SPE Journal*, 2015.

[66] Mark P Walsh and Larry W Lake. Applying fractional flow theory to solvent flooding and chase fluids. *Journal of Petroleum Science and Engineering*, 2(4):281–303, 1989.

[67] Daniel Weber, Thomas F Edgar, Larry Wayne Lake, Leon S Lasdon, Sami Kawas, Morteza Sayarpour, et al. Improvements in capacitance-resistive modeling and optimization of large scale reservoirs. In *SPE Western Regional Meeting*. Society of Petroleum Engineers, 2009.

[68] Daniel Brent Weber. The use of capacitance-resistance models to optimize injection allocation and well location in water floods. *PhD dissertation, The University of Texas at Austin, Austin, Texas, USA*, 2009.

[69] Henry J Welge et al. A simplified method for computing oil recovery by gas or water drive. *Journal of Petroleum Technology*, 4(04):91–98, 1952.

[70] BT Willman, VV Valleroy, GW Runberg, AJ Cornelius, and LW Powers. Laboratory studies of oil recovery by steam injection. *Journal of Petroleum Technology*, 13(07):681–690, 1961.

[71] Gary K Youngren. Development and application of an in-situ combustion reservoir simulator. *Society of Petroleum Engineers Journal*, 20(01):39–51, 1980.

[72] Ali A Yousef, Pablo Hugo Gentil, Jerry L Jensen, Larry Wayne Lake, et al. A capacitance model to infer interwell connectivity from production

and injection rate fluctuations. In *SPE Annual Technical Conference and Exhibition*. Society of Petroleum Engineers, 2005.

[73] Martin B Zarrop. *Optimal experiment design for dynamic system identification*. PhD thesis, Imperial College London (University of London), 1977.

[74] Martin B Zarrop, RL Payne, and GC Goodwin. Experiment design for time series analysis: the multivariate case. *SIAM Journal on Applied Mathematics*, 37(2):370–381, 1979.

[75] Yang Zhang and Thomas F Edgar. Pca combined model-based design of experiments (doe) criteria for differential and algebraic system parameter estimation. *Industrial & Engineering Chemistry Research*, 47(20):7772–7783, 2008.

[76] Zuhui Zhou, WR Rossen, et al. Applying fractional-flow theory to foam processes at the" limiting capillary pressure". *SPE Advanced Technology Series*, 3(01):154–162, 1995.

[77] Zhouyuan Zhu, Margot Gerritsen, Marco Thiele, et al. Thermal streamline simulation for hot waterflooding. *SPE Reservoir Evaluation & Engineering*, 13(03):372–382, 2010.

[78] Abdelhak M Zoubir and B Boashash. The bootstrap and its application in signal processing. *IEEE signal processing magazine*, 15(1):56–76, 1998.

Vita

Victor C. Duribe was born in Owerri, Nigeria. He received his Bachelor of Science degree in Chemical Engineering from Mendeleev University of Chemical Technology of Russia in July, 2011. In the Fall of 2011, he began his doctoral studies under the joint supervision of Drs. *Thomas F. Edgar* and *Larry W. Lake* at The University of Texas at Austin.

Permanent e-mail address: vduribe@gmail.com

This dissertation was typeset with LaTeX[†] by the author.

[†]LaTeX is a document preparation system developed by Leslie Lamport as a special version of Donald Knuth's TeX Program.